Universität Potsdam

Institut für Physik und Astronomie

A Multiscale Analysis of Additively Manufactured Lattice Structures

Dissertation

zur Erlangung des akademischen Grades
"Doktor rerum naturalium" (Dr. rer. nat.)
in der Wissenschaftsdiziplin "Experimentalphysik"

eingereicht an der Mathematisch-Naturwissenschaftlichen Fakultät
der Universität Potsdam

von

Tobias Thiede

Erstgutachter:	Prof. Dr. Giovanni Bruno
Zweitgutachter:	Prof. Dr. Christoph Genzel
Drittgutachter:	Prof. Dr. Simone Carmignato

Potsdam, 30.10.2019

"Was einmal gedacht wurde, kann nicht mehr zurückgenommen werden."

Friedrich Dürrenmatt - Die Physiker. S.85,
Diogenes Verlag, Neufassung 1980

Abstract

Additive Manufacturing (AM) in terms of laser powder-bed fusion (L-PBF) offers new prospects regarding the design of parts and enables therefore the production of lattice structures. These lattice structures shall be implemented in various industrial applications (*e.g.* gas turbines) for reasons of material savings or cooling channels. However, internal defects, residual stress, and structural deviations from the nominal geometry are unavoidable.

In this work, the structural integrity of lattice structures manufactured by means of L-PBF was non-destructively investigated on a multiscale approach.

A workflow for quantitative 3D powder analysis in terms of particle size, particle shape, particle porosity, inter-particle distance and packing density was established. Synchrotron computed tomography (CT) was used to correlate the packing density with the particle size and particle shape. It was also observed that at least about 50 % of the powder porosity was released during production of the struts.

Struts are the component of lattice structures and were investigated by means of laboratory CT. The focus was on the influence of the build angle on part porosity and surface quality. The surface topography analysis was advanced by the quantitative characterisation of re-entrant surface features. This characterisation was compared with conventional surface parameters showing their complementary information, but also the need for AM specific surface parameters.

The mechanical behaviour of the lattice structure was investigated with *in-situ* CT under compression and successive digital volume correlation (DVC). The deformation was found to be knot-dominated, and therefore the lattice folds unit cell layer wise.

The residual stress was determined experimentally for the first time in such lattice structures. Neutron diffraction was used for the non-destructive 3D stress investigation. The principal stress directions and values were determined in dependence of the number of measured directions. While a significant uni-axial stress state was found in the strut, a more hydrostatic stress state was found in the knot. In both cases, strut and knot, seven directions were at least needed to find reliable principal stress directions.

Zusammenfassung

Das Laserstrahlschmelzen (L-PBF) als Prozess im Bereich der Additiven Fertigung (AM) ermöglicht ein neuartiges Bauteildesign und somit auch die Produktion von komplexen Gitterstrukturen, welche Materialeinsparungen und effizientere Kühlsysteme erlauben und daher für verschiedene industrielle Anwendungen (z.B. Gasturbinen) geeignet sind. Interne Defekte, Eigenspannungen und geometrische Abweichungen von der Soll-Geometrie sind jedoch unvermeidbar.
Im Rahmen dieser Arbeit wird die strukturelle Integrität von L-PBF gefertigten Gitterstrukturen zerstörungsfrei auf verschiedenen Größenskalen untersucht.
Eine Auswerteroutine für dreidimensionale quantitative Pulvercharakterisierung hinsichtlich der Partikelgröße, der -form, der -porosität, des Interpartikelabstands und der Packungsdichte wurde entwickelt. Synchrotron Computertomographie (CT) wurde für die Korrelation der Packungsdichte mit der Partikelgröße und -form genutzt. Darüber hinaus konnte festgestellt werden, dass mindestens 50 % der Porosität aus den Pulverpartikel während der Herstellung der Streben mittels L-PBF gelöst wurde.
Streben sind die Grundbausteine der Gitterstrukturen und wurden mit industrieller CT untersucht. Dabei lag der Fokus auf dem Einfluss des Bauwinkels auf die Strebenporosität und -oberflächenqualität. Die Analyse der Oberflächentopographie wurde hinsichtlich einer quantitativen Analyse von sogenannten *re-entrant features* erweitert. Der Vergleich dieser Auswertung mit konventionellen Oberflächenparametern offenbarte sowohl deren Komplementarität also auch den Bedarf an neuen AM-spezifischen Oberflächenparametern.
In-situ CT Versuche mit anschließender digitaler Volumenkorrelation (DVC) erlaubten die Gitterstruktur bezüglich des mechanischen Verhaltens unter Druckspannung zu bewerten. Aufgrund einer schichtweisen Faltung der Einheitszellen konnte dabei das Versagensverhalten als knoten-dominiert identifiziert werden.
Mittels Neutronenbeugung konnten Eigenspannungen in solchen Gitterstrukturen erstmalig experimentell bestimmt werden. Dabei wurden sowohl die Hauptspannungsrichtungen als auch die -beträge in Abhängigkeit von der Anzahl der gemessenen Spannungsrichtungen bestimmt. Während in der Strebe ein signifikanter uni-axialer Spannungszustand nachgewiesen wurde, zeigte der Knotenpunkt einen hydrostatischeren Spannungszustand. Sowohl im Falle der Strebe als auch des Knotenpunkts waren mindestens sieben gemessene Spannungsrichtungen nötig, um die Hauptspannungsrichtungen verlässlich zu ermitteln.

Contents

List of Abbreviations

AM	Additive Manufacturing
BCC	body centered cubic
BD	build direction
BHC	beam hardening correction
CAD	computer aided design
CMM	coordinate measuring machine
CT	computed tomography
DS	down-skin
DVC	digital volume correlation
EBSD	electron back-scattered detection
FBP	filtered back projection
FCC	face centered cubic
FEM	finite element method
FWHM	full width at half maximum
HIP	hot isostatic pressing
L-PBF	Laser-Powder Bed Fusion
LD	laser diffraction
ND	neutron diffraction
NAC	nominal-actual comparison
OM	optical microscopy
PD	packing density
PSD	particle size distribution
PCA	principal component analysis
ROI	region of interest
RS	residual stress
SDD	source-detector distance
SOD	source-object distance
UC	unit cell
US	up-skin
XRD	X-ray diffraction

1 Introduction

The American physicist Chuck Hull initiated the current hype about Additive Manufacturing (AM) by patenting stereolithography in 1986 [1]. Stereolithography was the first layer-by-layer manufacturing technique and enabled a new route of part design and production. Although the technical application regarding spare parts and rapid prototyping was obvious, while juxtapose metal to polymer, about a decade was needed to develop metal based AM techniques [2]. Nowadays, an enormous variety of techniques designated as AM are available [3].

Additive Manufacturing

A specific AM technique needs to be considered for a given part geometry and part size according to the specifications such as the production speed and the part tolerance [4]. The most common AM techniques for metals are Electron Beam Melting, Direct Energy Deposition, Wire Arc Additive Manufacturing, Metal Binder Jetting and Laser-Powder Bed Fusion (L-PBF). All of them have the freedom of design in common, enabled by a layer-by-layer production process [5, 6]. That means a computer aided design (CAD)-file is virtually sliced and processed successively according to the production technique based on powder or wire feedstock of metals. The heat source is commonly a laser- or an electron-beam. The industrial application of metal AM covers repair of turbine engines, spare parts, light-weighted parts for aerospace, automotive industry, medicine and gas turbines [7]. This work focuses on L-PBF. This technique offers high part accuracy but lacks in production speed compared to other metal based techniques such as Direct Energy Deposition. Therefore, L-PBF is used for production of fine and complex geometries such as lattice structures with strut diameters smaller than 1 mm. These structures are applicable for gas turbines justified by reduced weight, improved premixing of fuel, and opportunities for increased heat transfer and cooling rates. This enables less polluting exhausted gas emissions and enhanced total efficiency of the turbine.

First non-safety relevant parts produced by L-PBF are already in use for aircraft [8] and gas turbines [9]. The production of non-safety relevant part is mainly focused on materials savings and design optimisation [10]. The quality assurance by means of internal defects and residual stress (RS) characterisation becomes important only for safety-relevant parts. The knowledge about long

term performance is essential for certification of safety relevant AM parts. The strengthening mechanisms, fatigue behaviour, and crack initiation significantly differ from conventional parts. Therefore, their understanding in AM parts is essential for life time prediction and safety in application [11]. If safety relevant parts shall be used in the future, the understanding of AM specific defects, such as internal voids, geometrical inaccuracy, surface roughness, and residual stress is crucial to optimise the manufacturing process.

Powder Characterisation

This knowledge about part quality needs to be improved. The quality assurance begins where the process begins: the powder-feedstock.
Besides L-PBF, several of the above-mentioned AM techniques are based on powder-feedstock. Therefore, powder characterisation should be the first step for process optimisation. Powder properties, such as heat conduction [12], flowability [13], particle packing density [14], internal porosity [15], particle size, and particle shape [16], may influence the powder bed quality [17]. Some of these powder characteristics are certificated by the manufacturer such as particle size distribution (PSD) and flowability. Usually, the PSD is evaluated by a sieving procedure or by laser diffraction (LD) measurements. Both techniques could provide fast and inexpensive conformation of particle size. However, no information about particle shape is available [18].
The measurement technique affects the results of powder characterisation [19]. Therefore, a comparison among different techniques is difficult. It has been shown that LD results yield comparable lengths (*i.e.* maximum diameter) to particle sizes observed by means of X-ray computed tomography (CT) [20]. However, the shape of particles has an influence on particle size measurement [21], while in the case of LD, particles are assumed to be spherical [22]. The discussion about particle shape becomes even more critical when recycled powder is used during the manufacturing process, since the mean particle size and shape change after the first use [23–25] and certificates are not applicable any longer. Spierings *et al.* [13] have discussed the influence of the powder characteristics on the flowability, see Figure 1.1a.
Several publications have used 2D imaging techniques such as microscopic analysis to characterise powder feedstocks [25–27], see Figure 1.1b. However the particles have to be characterised in three dimensions for maximum information [28]. Com-

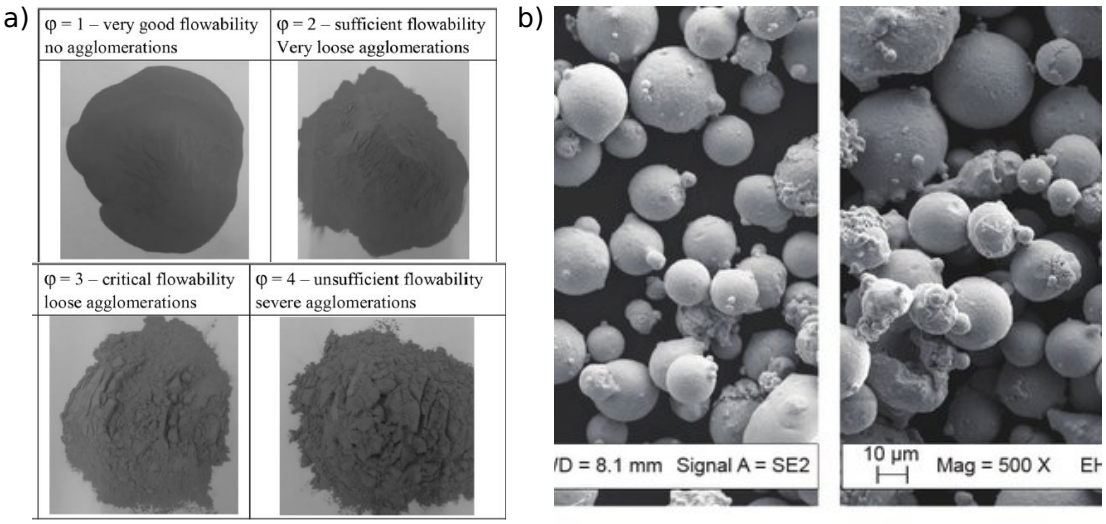

Figure 1.1: a) The optical investigation of the powder particle flowability taken from [13] and b) a typical optical microscopy image of powder particle for AM taken from [25].

puted tomography is a tool for volumetric powder characterisation [29]. It allows the acquisition of more statistically-relevant information (*i.e.* number of particles) compared to optical microscopy or scanning electron microscope.
As shown in [30], the use of realistic powder characteristics during modelling of AM processes is necessary for an accurate prediction of porosity and melt pool dimensions. One of the critical points for powder characterisation is porosity, since it can be transferred into the part and decrease its quality. Chen et al. [31] have shown that porosity in powder particles can depend on the method of powder production (*e.g.* water-, gas-, and plasma atomisation) as well as on the particle size. Also, the distribution of particles in the powder bed may lead to additional porosity in the part due to voids between particles [32]. Powder batches with different PSDs are known to induce a difference in powder bed quality affecting the built part quality [33].

Porosity

Porosity is a known problem for L-PBF parts [15, 34, 35]. The analysis of porosity inside of parts by means of CT started more than ten years ago [36, 37]. CT is the method of choice for non-destructive porosity analysis as it allows the evaluation of pores size, shape and spatial distribution [15] in 3D. This 3D analysis

by means of CT is also rich in pore statistics compared to the 2D analysis by means of optical microscopy on cross sections.

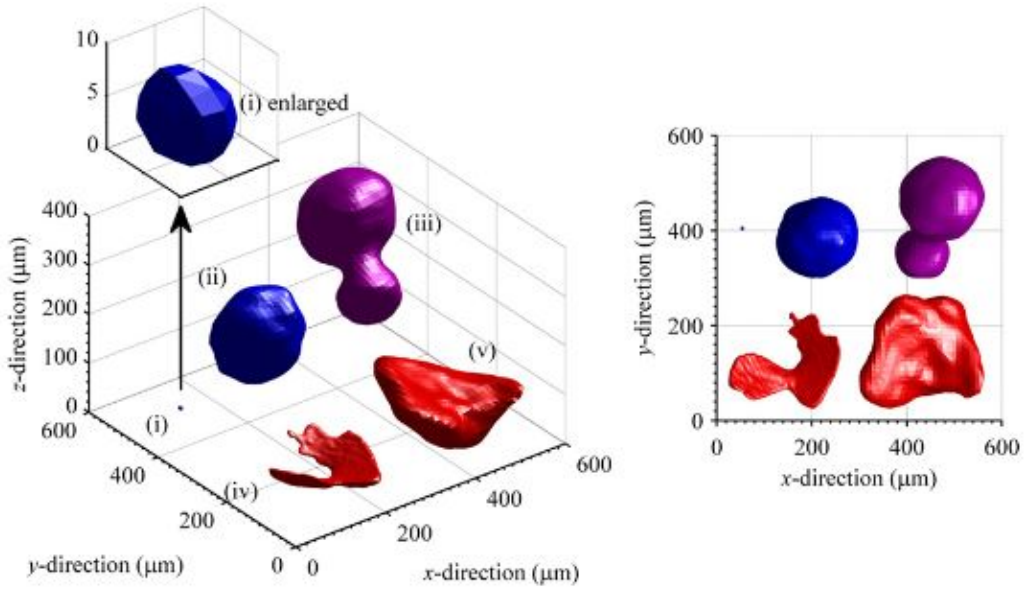

Figure 1.2: The different kind of pores, 3D rendered based on CT data taken from Tammas-Williams *et al.* [15]

Studies focused on X-ray CT and L-PBF are mostly conducted on low- to medium-absorbing materials such as aluminium-based alloys or Ti-6Al-4V [38–41]. The porosity characterisation has been used for optimisation of the process parameters [42]. CT and the Archimedes principle have been proven to be in good agreement for porosity measurements [43]. The quantification of defects by means of CT has been discussed by Maskery *et al.* [41]. The correlation between shape and origin of pores has been investigated by Tammas-Williams *et al.* [15]. The most likely appearance of micro porosity is known to be in the overlap region between contour and filling hatches. A hatch is one laser scan vector. The distinction of three kinds of pores is accepted in the current literature [15]: Keyhole pores, which were recently found to be induced at the turning points of the laser [44], the elongated lack of fusion pores, which are created if the energy input is not large enough to fuse layers or hatches together [42], and the round gas pores, which are induced by an excess of energy input [15, 42], see Figure 1.2. Another reason of pore formation was observed by means of Synchrotron *in-situ* radiography of the melt track. Spattered powder particles induced open porosity in the current layer. This open porosity was then only partly closed by the subsequent layer

melting [45].
Especially the lack of fusion pores are assumed to impact the mechanical properties of the part due to their elongated form and stress accumulation for large curvature radii [46]. Indeed, Vilaro *et al.* proved by means of fractography that lack of fusion porosity with a size larger than 100 μm is the origin for crack initiation [46]. Not only single lack of fusion pores but also an accumulation of round pores are detrimental for the part; Voisin *et al.* observed that a coalescence of pores under tensile load leads to early failure [47]. In this case, the part porosity was $\ll 1\,\%$. Tammas-Williams *et al.* were able to close all the porosity below the resolution of the CT measurement of about 5 μm by means of hot isostatic pressing (HIP) [48]. However, surface pores (*i.e.* open porosity) even increased their volume. This is critical as pores close to the surface were found as initiation for fatigue cracks [49]. Due to the high temperature, the microstructure was affected by HIP [50]. It has been shown, that the microstructure and hence the mechanical performance of various materials depend on the build angle (*i.e.* the angle between the nominal part surface and the build plate) [19, 51–53]. The same holds for the porosity distribution within a part [52].

Surface topography

Similar to the porosity, the surface topography is currently considered as a source of defects of AM parts [38–40, 54]. Methods to quantify the surface topography in terms of surface roughness such as coordinate measuring machine (CMM) and optical microscopy (OM) have limitations for small and round-shaped samples as well as complex structures [55]. The need for CT regarding the investigation of L-PBF parts is justified because no other non-destructive technique allows the evaluation of complex geometries with inner surfaces [38, 39] and re-entrant features [56].
State of the art roughness measurement techniques for conventional materials are tactile and optical surface probing. A comparison between tactile and CT measurements on flat surfaces has proven the applicability of CT for roughness analysis [57, 58]. The accuracy of CT was proven for metrology [59–61].
Du Plessis *et al.* showed the applicability of CT for AM surface analysis in the example of the external surface of a cube [62]. The next step was the characterisation of *inner* surfaces as carried out by Townsend *et al.* [63]. They found no significant difference between the extracted interior and exterior surface to-

pography by means of CT. They also emphasized the need for a local surface determination rather than a global ISO value[63]. Chen *et al.* investigated the roughness of cone-shaped test specimens by means of CMM [54]. The equivalence between CMM and CT was proven by Shah *et al.* [64].

Recently, Pagani *et al.* defined new surface characterisation parameters for AM surfaces [56]. These parameters were estimated on a free-form surface and consider the re-entrant features of the AM surface.

Another important aspect to define the surface topography of tilted structures, are overhanging surfaces (without solid material below) which is created by applying the scanning parameters for so called down-skin (DS), and surfaces with no solid material above, created by the scanning parameters for so called up-skin (US) [26, 65, 66], see Figure 1.3a. DS regions of L-PBF parts showed higher mean roughness values than US regions [54, 67] due to a higher number of attached powder particles and reduced heat conduction, so that overheating may occur in these DS areas.

Kleszczynski *et al.* observed an influence of the sample position on the baseplate on the surface topography of the sample [68]. The position on the baseplate changes the laser incidence angle. The far side of the strut (with respect to the laser) showed higher roughness values for any sample position, see Figure 1.3b.

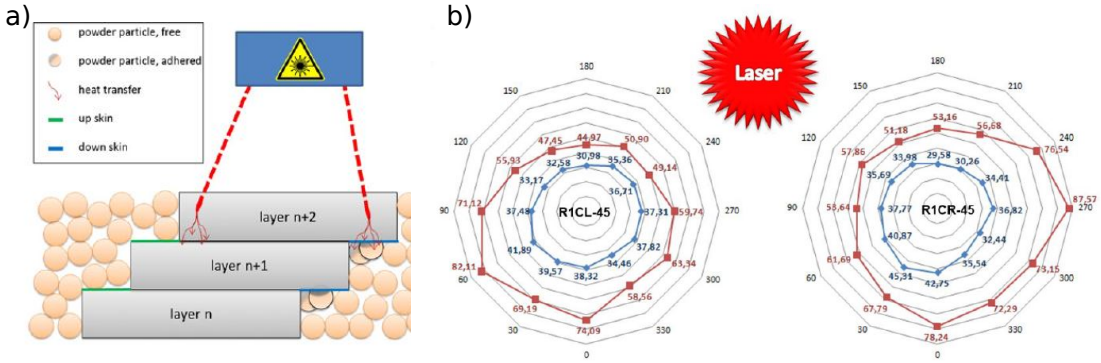

Figure 1.3: a) A sketch by Grimm *et al.* indicating the up-skin and down-skin regions for a tilted structure taken from [65] and b) the influence of the incidence angle of the laser beam in respect to the sample surface taken from [68].

Like the porosity and the microstructure, the surface topography is also influenced by the build angle [67]. The characterisation of the surface topography is assumed to be equivalent for L-PBF as well as for electron beam melted samples. Suard *et al.* discussed electron beam melted struts with dependence on the build

angle [40, 69]. They noticed that the stiffness of the strut, simulated on the base of the CT-surface, is in-between the stiffness of the inscribed and circumscribed cylinder [69], see Figure 1.4a. They introduced the equivalent cylinder having the same volume as the CT volume of the strut, see Figure 1.4b. This equivalent cylinder described the stiffness in the best way [40].

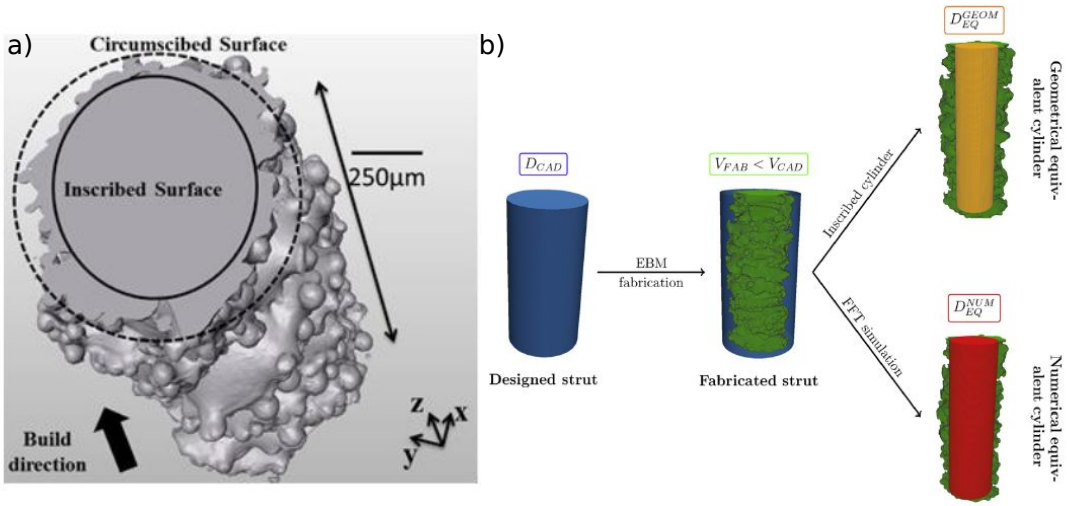

Figure 1.4: a) Indicates the choice of the inscribed and circumscribed cylinders as a strut equivalent taken from [69] and b) represents the volume deviation of the produced strut from the nominal strut taken from [40].

Electron beam melted struts showed an improvement of the fatigue bending strength for 45° compared to 90° [70]. Interestingly, in a study by Weissmann *et al.* [71] the 45°-strut showed the lowest compression strength. The failure mechanism was inspected in more detail and both symmetric and asymmetric buckling were observed for the struts under compression [71]. These studies prove the sensitivity of different mechanical properties to the build orientation in L-PBF.

Lattice Structures

Lattice structures, which are also called cellular structures in the literature [72, 73], can only be manufactured by L-PBF laser and electron powder bed fusion offer, if we specify the precision required for the construction of such complex structures. As their application is meant for replacement of bulk material (to save material and weight), their mechanical properties are often discussed in literature [74]. Different choices of the kind of unit cells, strut diameters, and

strut lengths allow a fine tuning of the lattice density. Different kind of unit cells have been found to induce different elastic moduli and yield strengths of the lattice structure [73]. The deformation of body centered cubic (BCC) lattice structures is dominated by either bending or stretching [72].
Due to the complexity of lattice structures, simulations are used to support their evaluation. A new simulation method to consider also the strut topography (up to a certain degree) was introduced in [75]. This method decreased the error of simulated part distortion compared to CAD-file. Rosa *et al.* proved by finite element method (FEM) simulation that lattice structures could also be used in damping structures [76].

Residual Stress

RS would influence both, the distortion and the mechanical properties, but is not yet reported for a lattice structure in literature. The distortion was shown to be significant for the fine lattice structures [77].
The creation of RS in L-PBF is described by Kruth *et al.* in [78]. The local heat input by the laser lead to melting and thermal expansion of the material. The thermal stress exceeds the yield strength and induces a zone of plastic deformation. This plastic deformation is the reason for resulting RS after cooling, as the plastic zone hinders shrinkage during cooling [78]. This scenario appears similar to RS formation in welds, which is understood in some detail [79–83]. Even though L-PBF can be described as a continuously repeated welding process, the extrapolation of the stress state induced by a superposition of welding processes to that induced by L-PBF is not possible. Instead, studies showed that RS in L-PBF parts are primarily caused by the temperature gradients due to continuous re-heating and cooling of previously solidified layers [84–86].
The production of thin walled structures is one of the main advantages of L-PBF. However, the presence of RS in such thin walled parts, may lead to distortion, delamination, and cracking of the part after or even during production [87–89].
Any process parameter of L-PBF changing the thermal history of the material will have a consequence for the RS state. The current challenge is the determination of all influencing process parameters and their ranking according to priority. The first important and well investigated parameter is the scanning strategy (*i.e.* the order each slice is deposited) [90–96]. The idea is to decrease RS already *during* the build job. This can be achieved using a homogenous distribution

of heat input. The influence of the scanning strategy on the distortion of the part needs to be considered for production of AM parts, since it was correlated with the stress relaxation and redistribution after removal from base plate [93, 95, 97]. A simulation by Parry *et al.* [98] recommended to avoid long hatches. This was supported by experimental results [99], and led to the conclusion that islands (*i.e.* squares) should be scanned instead of elongated regions. However, a contradiction was found for the island scanning strategy on 316L stainless steel. While several publications reported the lowest RS values [90, 95, 96], Bagg *et al.* found the largest RS values for the island scanning strategy compared to uni- and bi-directional scanning [91]. In addition, results of both simulations and experiments recommended a subsequent rotation of 15° of the hatching direction from layer to layer to reduce RS [100]. Other parameters influencing the RS state in the printed part were the number of layers and the thickness of every layer [85]. As described previously, the energy density has a large impact on the defect distribution. The energy density was also found to influence the RS state [101]. Since support structures promoted a more efficient heat transfer compared to powder [98], support structures will decrease the heat accumulation in the part and affects the RS state within the part [102]. The position of the part on the build plate during the manufacturing is receiving increasing attention. Small stress differences were found between samples being equal but for the position on the build plate [101, 103]. An influence of the geometry is expected but difficult to quantify because the geometry is not independent of other parameters, *e.g.* hatch length and interlayer time.

The non-destructive estimation of RS is an important field for the safety of the material [104] and therefore, for industrial applications [7]. The characterisation of RS in AM parts is performed mainly by destructive or semi-destructive techniques (e.g. the contour method [105–107], the hole drilling method [103], and the bridge curvature method [90, 91, 97]). The examples of non-destructive RS investigations are mainly focused on surface investigations by means of laboratory X-ray diffraction (XRD) [85, 108]. If one wants to determine bulk residual stress, laboratory XRD would need an incremental layer removal [109]. This requires extensive sample preparation and is time consuming. However, the use of large scale facilities (*i.e.* synchrotron and neutron reactor) is receiving increasing attention, since the non-destructive determination of RS distributions in AM material is of significant interest for structural integrity. The only non-destructive tech-

nique suitable for triaxial bulk RS characterisation with a mm spatial resolution is neutron diffraction (ND) [110]. Moat *et al.* showed that ND and the contour method are in agreement [107]. Synchrotron radiation allows efficient subsurface RS analysis [97, 102, 111].

Wang *et al.* reported a significant body of research using ND on IN 625 [112–114]. They showed that AM IN 625 exhibits a higher stress relaxation rate and lower peak and plateau stress than conventionally processed IN 625. They attributed this difference to different texture and grain sizes in the two materials [114]. Additionally, they presented a good agreement between ND experiments on IN 625 and thermo-mechanical stress simulations [113].

Simulations are a common method of stress estimation. The experimentally determined RS induced by thermal gradients for different scanning strategies was predicted through a thermo-mechanical FEM simulation [115, 116]. However, the complex nature of the AM-process impedes the success of simulations. In the work [117] the simulated distortion deviated by 26 % from the experiment. A benefit for understanding is achieved if simulation and experiments are combined to describe the part [116, 118–120].

A significant challenge for ND is the choice of an appropriate stress-free reference (d_0). In Refs. [113, 121], the variability of d_0 value along the sample height because of the microstructure evolution was discussed. Also, in Ref. [113], the use of position dependent d_0 was recommended, whereas in Ref. [122], the average value of three components has been used. A heat treated d_0 coupon (from IN 625) in Ref. [113] showed a change in chemical composition compared to the as-built d_0 coupon, leading to a lattice spacing shift. This calls for a spatial resolved d_0 measurement.

The high penetration of neutrons makes ND the only tool to non-destructively investigate complex AM structures [123]. Cakmak *et al.* started to use ND to investigate also more complex shapes than cuboids [124]. However, the principal stress directions were only determined for forged [125] and rolled [120] parts. Even in the case of simple cuboidal geometry a deviation of the principal stress directions from the geometrical directions was observed for L-PBF [126]. This finding correlates well with the observation from Vrancken *et al.* [127] who found that the principal stress directions at the surface coincide with the hatching direction of the last layer for all samples [127].

Measures to minimize both porosity and RS are established in the industrial production chain: Stress relief heat treatment to suppress RS and HIP [50] to close porosity. However, they are expensive, time consuming, and affect the microstructure of the part. Hence, there is a need for new strategies, and even for elimination of post-production treatments.

Motivation and Strategy

A thorough understanding of a complex structure requires the understanding of each single constituent of it. Here lies the novelty of this thesis: a multiscale materials characterisation that enables L-PBF process understanding and quality assessment. The scale extends from the powder particles ($10 - 40\,\mu$m) to the lattice structures (4 cm), as schematically shown in Figure 1.5.

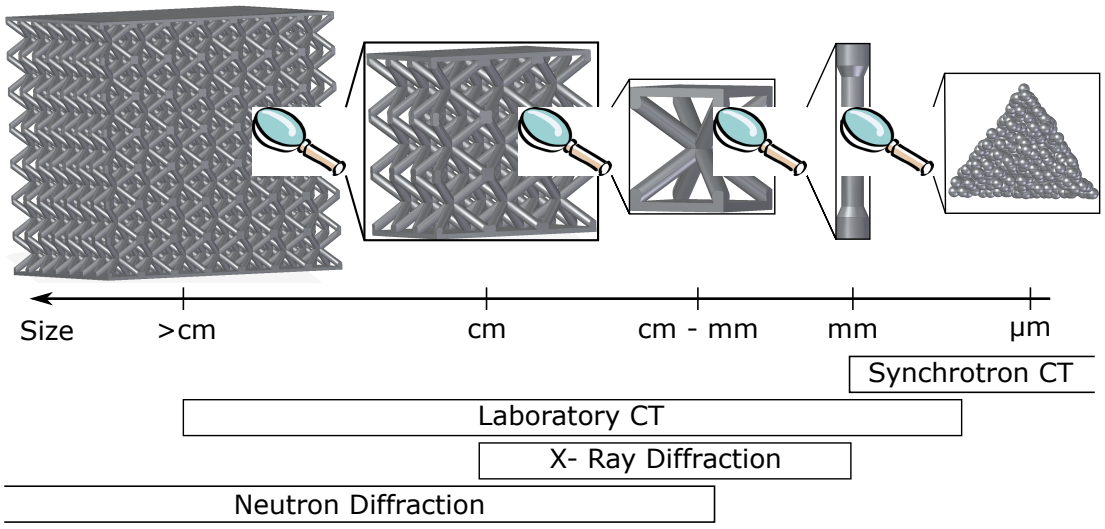

Figure 1.5: Sketch of the multiscale approach of the present investigation: from powder particles to lattice structures

The powder batch used for the manufacturing process will be evaluated regarding the size, shape, and arrangement within the powder bed. Synchrotron CT offers the best image quality and will therefore be optimised for a 3D analysis for such small powder particles partly below $10\,\mu$m.
As discussed above, a variety of small and simple samples such as cylinders have been investigated by means of CT. However, in the present context, an in-depth analysis on surface parameters such as roughness and re-entrant features is still missing. Within this thesis, existing evaluation routines will be advanced. In

this way, the information of the powder will be linked to the porosity and surface topography of the part. A special focus will be made on the influence of the build angle, as the struts are the basic constituent of lattice structures. Since post-processing (*e.g.* polishing) is expensive and ineffective for these complex and fine structures, the as-built surface topography is of highest interest for the fatigue behaviour of the structure and for the gas flow through the lattice structure. At the same time, the distribution and shape of inner defects (e.g. pores and delaminations) are of importance because they affect the mechanical performance of the structure as discussed above. Such aspects will be thoroughly treated herein.

In-situ CT is of significant current interest, since is allows resolving phenomena over time. In this thesis, the application of digital volume correlation (DVC) will reveal the deformation field of the lattice structure under external load.

A general problem of AM is the registration of the nominal volume (CAD) on the actual volume (*e.g.* measured by CT). The complexity of the lattice structure will allow improving the registration procedures.

While RS are mainly irrelevant for small samples such as struts, they become of interest for larger and more complex parts, such as the lattice structures. The RS-field within the lattice structures will be evaluated, and a discussion on the principal stress directions will be carried out.

Even though different materials are processed by means of L-PBF, such as Ti-6Al-4V (aerospace, medicine), austenitic stainless steel 316L (chemical engineering), AlSi10Mg, Hastelloy X or Inconel 718 (turbine engines), this work will focused on the nickel superalloy Inconel 625. All evaluation methods will be material-independent.

The aims of this thesis are summarised as following.

- Development of a workflow for powder characterisation by using high resolution synchrotron computed tomography
- A detailed strut characterisation, encompassing an advanced porosity analysis and the quantification of the surface topography in dependence of the build angle
- Determination of the mechanical response of lattice structures with focus on the geometrical accuracy, deformation under external load, and internal (residual) stress

2 Background Information

In this section, a comprehensive background is presented about the used material (IN 625), the manufacturing process (L-PBF) and the two main characterisation methods (CT and ND).

2.1 Inconel 625

The used material is the nickel-based superalloy Inconel 625 (IN 625). The nominal chemical composition of IN 625 powder is listed in table 2.1 [128]. The large amount of chromium (together with nickel) induces a high oxidation and corrosion resistance. These properties are most important for the application in gas turbines. The γ phase (matrix) of IN 625 has a face centered cubic (FCC) crystal structure and shows the precipitations γ' (Ni_3Al), γ" (Ni_3Nb) and delta phase (Ni_3Nb) [128]. IN 625 is a γ'-hardened material. Important for later, a FCC crystal structure allows only diffraction for lattice planes, which fulfil the condition: the Miller indices h,k,l are all even or all odd.

Table 2.1: Chemical composition of IN 625 powder in $wt\%$ according to [128]

Cr	Mo	Fe	Ta+Nb	Mn	Si	Ti	Al	Ni
$20-23$	$8-10$	5	$3.14-4.15$	0.5	0.5	0.4	0.4	balance

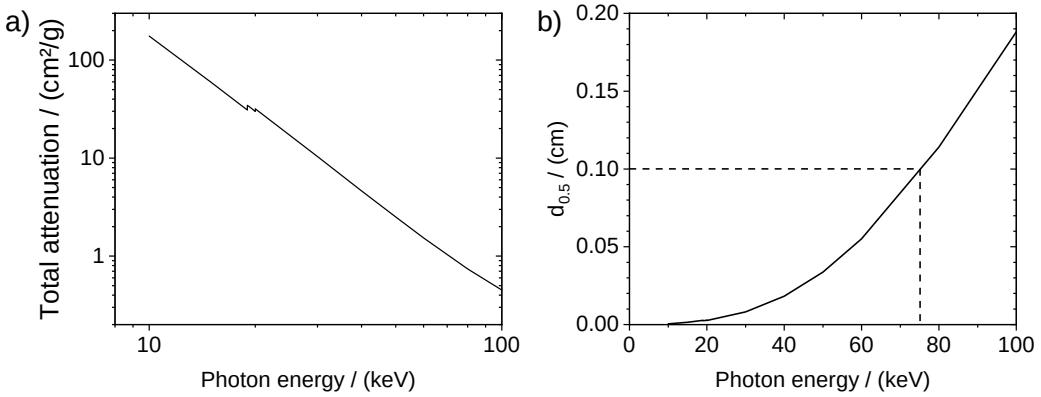

Figure 2.1: a) Total attenuation of X-rays by IN 625 and b) thickness of a plate IN 625 that absorbs 50 % of the X-ray intensity for a given energy [129]

The high amount of Cr, Fe, Ni, and Mo with electronic numbers of 24, 26, 28, and 42 leads to a materials density of $8.44\,\mathrm{g/cm^3}$. Therefore, the X-ray absorption

of IN 625 is rather high. The X-ray attenuation and the half-value thickness are plotted in Figure 2.1a and b. The plots are based on the online library by Henke *et al.* [129]. It lists X-rays energies up to 100 keV. The half-value thickness describes the thickness of a plate which would show 50 % transmission. For example, a 1 mm thick plate of IN 625 requires X-rays of 75 keV energy to achieve 50 % of transmission. Such information are necessary for CT experiments.

2.2 Laser-Powder Bed Fusion

Laser-Powder Bed Fusion is a specific process within a broad range of Additive Manufacturing techniques (briefly described in chapter 1). The production chain is split into three main steps:

1. Pre-processing:
The part is designed as CAD-file. Software assisted geometry optimisation is conducted as well as an optimisation of the build orientation regarding part distortion and residual stress. After subsequent virtual slicing of the part, the build job is sent to the L-PBF machine.

2. Printing:
L-PBF is conducted in a sealed build chamber consisting of a build plate adjustable in height, a re-coater with an attached powder reservoir, a gas flow facility and a mirror system for guidance of the laser beam, see Figure 2.2. The size of the build plate limits the part size in length and width while the part height is constrained by the maximum travel distance of the build plate. The layer-thickness d_{layer} is defined by the step width of the downwards motion of the build plate and corresponds to the slice thickness of the sliced CAD-file. After each step, the re-coater spreads a new layer of powder-feedstock; this is followed by the laser scanning and melting routine. The constant flow of protective gas (*e.g.* argon) protects the melt pool against oxidation. The re-coater and the protective gas flow are arranged perpendicular to each other. After repetition of stepwise sinking of the build plate, the re-coating and the melting process for all layers, the build job is finished.

3. Post-processing:
The solidified part and the loose powder have to be separated. Closed hollow chambers designed within the part need to be drilled, to permit the removal of the enclosed powder. Unmelted powder is removed using a vacuum cleaner and can be reused after sieving.
A subsequent solution heat treatment of the part shall release the RS. For IN 625, a quenching and an ageing cycle are necessary. The part is then removed from the build plate, and support structures have to be removed manually. Hot isostatic pressing to close porosity and surface polishing to give a consistent surface finish may be conducted as a final step.

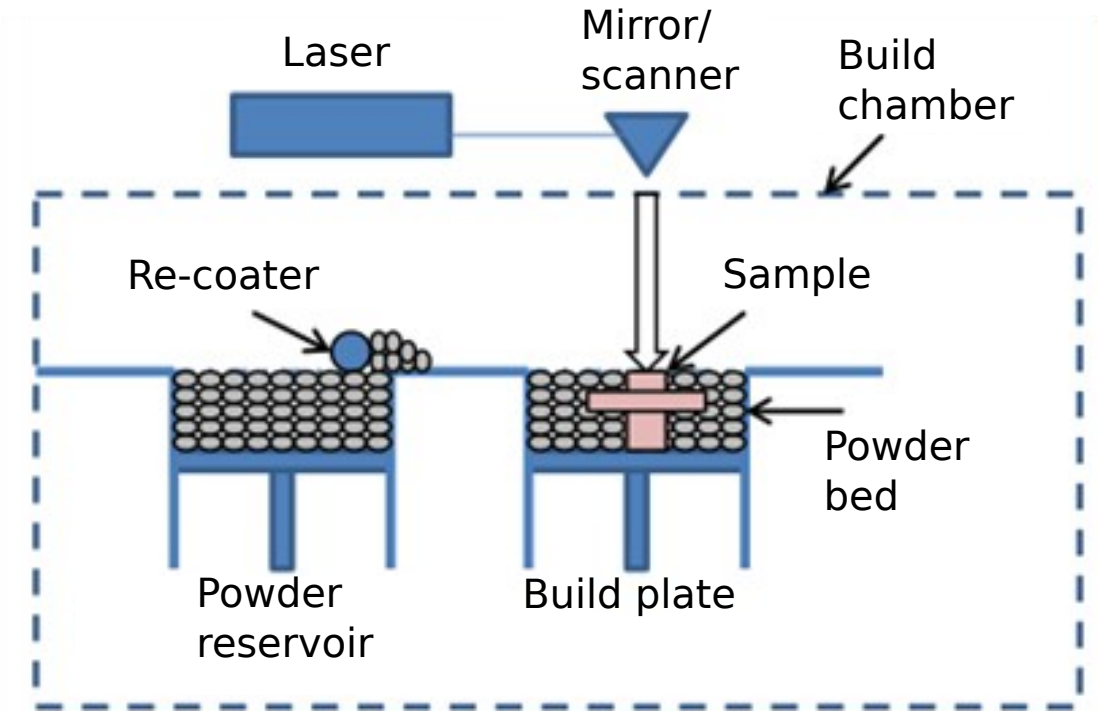

Figure 2.2: Schematic of the L-PBF process taken and adapted from [78].

The printing process can be tuned by a wide range of parameters. This chapter is focused on the energy density E_V as main parameter. This is the energy input per volume unit, which has become an important parameter for optimisation of porosity [42], see figure 2.3a.

$$E_V = \frac{P_{laser}}{v_{laser} \cdot h_d \cdot d_{layer}} \tag{2.1}$$

The laser power P_{laser} and the laser velocity v_{laser} are tunable in the range of

typically $150 - 450\,\mathrm{W}$ and $1000 - 1800\,\mathrm{m/s}$, respectively [130]. A hatch is equal to a scan vector. The hatch distance h_d depends on the diameter of the laser focus spot d_{laser} which typically has a full width at half maximum (FWHM) of around $100\,\mu\mathrm{m}$. An overlap between two hatches of at least $10\,\%$ is recommended ($h_d \leq 90\,\mu\mathrm{m}$) to properly fuse two hatches and minimise the porosity [130]. The layer thickness d_{layer} is recommended to be at least the size of the mean powder particle diameter d_{powder} [131]. A powder particles size of $10 - 60\,\mu\mathrm{m}$ leads to a layer thickness of $20 - 50\,\mu\mathrm{m}$.

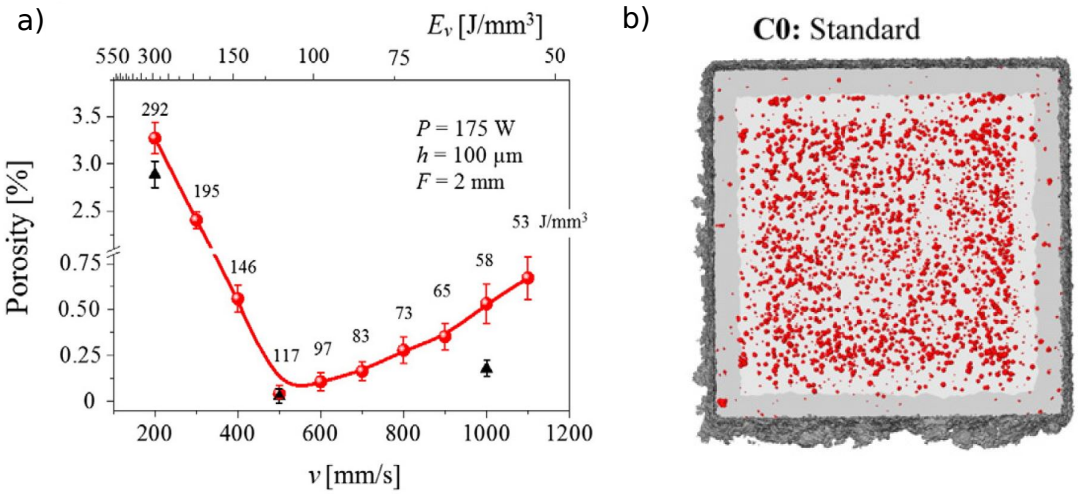

Figure 2.3: a) Kasperovich *et al.* [42] showed how the energy density E_v is used to optimise the porosity and b) and Tammas-Williams *et al.* [15] showed that CT can be used to observe and quantify the relationship between scanning strategy and resulting pore distribution.

The scanning strategy is defined as the pattern of laser movement *i.e.*, the arrangement of hatches. It can be varied within a layer and from layer to layer. An example for an interlayer variation is the so called contour scanning applied in regions close to the surface ($\leq 200\,\mu\mathrm{m}$). A contour hatch has a lower v_{laser} and P_{laser} compared to a filling hatch (applied for the bulk material) to reduce the melt pool dynamics and yield a smooth surface. A large variety of different scanning strategies has been investigated: uni- and bi-directional scanning, spiral contour scanning, $90\,^\circ$-rotation and $67\,^\circ$ scanning [15]. Currently, the most common scanning strategy, is the rotation strategy as it promotes a more isotropic microstructure and suppresses columnar grain growth along the building direction [84].

2.3 Computed Tomography

The term computed tomography (CT) is derived from Ancient Greek: *tomos = slice* and *graphō = to write*. Indeed, the first tomographs had an 1D detector array leading to a visualisation of one single slice of the object, *i.e.*, a tomogram. Nowadays, 2D detectors are state-of-the-art and therefore a full volume is recorded during a CT measurement. This section is based on [132, 133]:

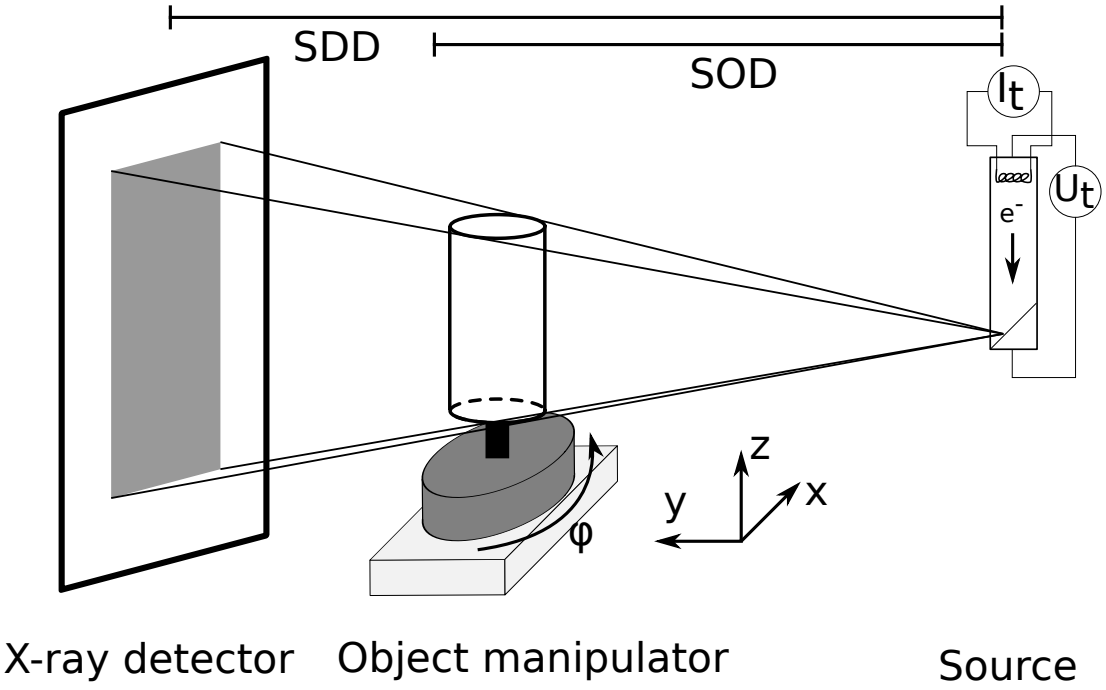

Figure 2.4: A schematic of the CT experiment

The principle of CT is the Radon transform described by Johann Radon in 1917 [134]. The Radon transformation states that a line integral along a projection of a function $f(x, y)$ is equal to the Fourier transform of that projection. Therefore, the inverse Radon transform allows the reconstruction of a function $f(x, y)$ from the projections. During CT scanning, projections of an unknown density function $f(x, y)$ (*i.e.* the object) are acquired in real space. According to the Fourier Slice Theorem, the 1D Fourier transform of that projection corresponds to the 2D Fourier transform of f(x,y) defined on a line in Fourier space parallel to the projection and cutting the origin. Therefore, the acquired projections build the 2D Fourier transform of the object in the Fourier space line by line. As low frequencies are sampled at a higher rate, since they are closer to the origin, a filter (or kernel) is applied in Fourier space to compensate for the

inhomogeneous point distribution. Now, the inverse Radon transform leads to the reconstruction of the object function $f(x, y)$. This reconstruction algorithm is known as filtered back projection (FBP) [135].
Complementary, iterative reconstruction techniques allow a higher degree of flexibility. While FBP requires a half or full circle scan, iterative reconstruction techniques do not require any specific projections. An initial object function $f(x, y)_0$ is iteratively adopted until the projections of the reconstructed object function match the acquired projections within a certain error. Higher computational demand is the trade-off for less and randomly required input data (projections).
The transmitted radiation intensity (*i.e.* a projection) follow the Lambert-Beer's law.

$$I = I_0 \exp\left(-\int \mu(x, E)dx\right) \tag{2.2}$$

The absorption coefficient $\mu(x, E)$ may depend on the energy E and the position x within the sample. The absorption of X-ray photons within the materials is governed by three main interaction mechanisms.

1. Photoelectric effect
If the energy of the incoming X-ray photon is higher than the binding energy of the atomic shell electron, the X-ray photon is absorbed, while its energy is used to ionise the atom. The transition of outer shell electrons onto a lower energy level causes emission of a scatter photon.

2. Compton scattering
Compton scattering describes a case of inelastic photon-electron scattering. The incoming X-ray photon transfer a part of its energy to a atomic shell electron and is deflected.

3. Pair effect
The pair effect needs to be consider for high energies only ($\geq 1.022\,\mathrm{MeV}$). The kinetic energy of the incoming X-ray photon is used to create a new electron-positron pair.

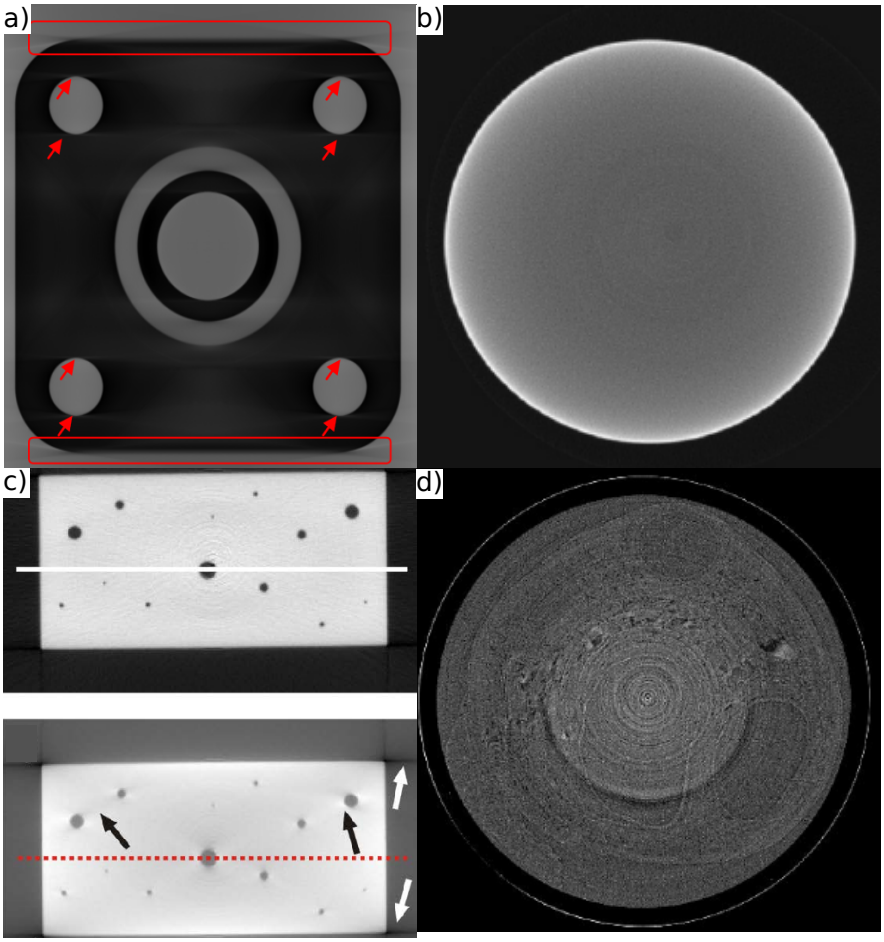

Figure 2.5: Examples extracted from literature to give an impression of a) the cone beam [136], b) the beam hardening [137], c) the scatter [138] and d) the ring artefacts [139].

CT is based on transmission of X-rays. The three above described interaction mechanisms lead to photon scattering in the sample. Such scattering decreases the resolution as the key parameter of CT scans. Resolution is defined as the minimum distance at which two features could still be recognised separately. The theoretically best resolution is equal to the voxel size (see chapter 2.3.1). Independent of the reconstruction techniques, image artefacts may decrease the image resolution. Various artefacts are known and should be compensated:

1. Cone beam artefact, Figure 2.5a

If a cone beam is used, which is typical for a laboratory tomograph, then only the central plane is mathematically correctly reconstructed, since the back projection does not consider cubic voxel. A correction is implemented in the FBP-algorithm.

However, it fails near the top and the bottom of the detector and on the top and the bottom of high absorbing material (see Figure 2.5a), since pathway of the X-ray beam through the material is different.

2. Beam hardening artefact, Figure 2.5b
Beam hardening is unavoidable when using a polychromatic X-ray beam. The low energy photons (*i.e.* soft X-rays) are more likely to be absorbed by the material than high energy photons. The first layers of material harden the X-ray beam and less photons are absorbed by the inner material. The former will appear less dense in the tomogram. With the assumption of a constant X-ray absorption, the effect can be corrected by application of a polynomial fit of grade n with $n + 1$ fitting parameters.

3. Scattering artefact, Figure 2.5c
Scattering occurs twice during the acquisition process. First, X-ray photons scatter within the material. It depends strongly on the material's density and the sample's geometry. However, this effect is most prominent for photon energies larger than 300 keV and a short sample to detector distance which is rarely used in CT with μm-resolution. The second scatter process occurs inside the scintillator material in the detector. A thinner scintillator layer would suppress the scattering in trade off with a drop of quantum conversion increasing the image noise.

4. Ring artefact, Figure 2.5d
A sinogram is the representation of the movement of a single voxel in the sample in dependence of the rotation angle for each slice. An object without movement during sample rotation, such as dust or splatter particles on the tube window or the detector appear as straight lines in the sinogram. Such lines lead to ring artefacts in the tomogram. Ring artefact can be corrected by a wavelet filter [140] on the sinogram.

2.3.1 Laboratory Computed Tomography

Nowadays, a typical laboratory tomograph consists of a X-ray tube, an area detector, and a manipulator system mounted on a granite base. The latter allows movements with micrometer precision. In the X-ray tube a tungsten filament

is heated by electric current. The number of emitted electrons is controlled by the tube current I_t. The filament emits thermal electrons that are accelerated in the static electric field between cathode (tungsten filament) and anode (target). Dipole magnets focus the electron beam. The maximum energy of the electrons depends linearly on the applied tube voltage U_t.

$$E_{max} = e \cdot U_t \tag{2.3}$$

By hitting the target, the kinetic energy of the electrons is converted into thermal energy and kinetic energy emitted in form of X-ray photons. The electrons are decelerated in two ways: a continuous deceleration, due to Coulomb interactions with the atomic shell electrons, and ionisation of the atom. The first case leads to a continuous X-rays spectrum, while the ionisation process leads to a characteristic X-ray spectra due to the defined atomic energy levels for electrons. The vacant electronic state is occupied by an electron from an outer shell. Photons with the energy difference between the two electronic states is emitted in form of characteristic peaks.
Important to note is the difference between transmission and reflection targets. A transmission target allows smaller focus spot sizes. However, the tube power $P_t = U_t \cdot I_t$ has to be lower, since the electron beam would burn the thin target.
The manipulation system allows sample positioning by means off three perpendicular translation axes and sample rotation. The rotation stage is either a mechanical bearing system for higher load capacity (but lower angular precision) or an air bearing system for higher angular precision (but lower load capacity).
A 2D flat panel detector is commonly used for image acquisition. The detector position along the source-object-detector axis tunes both the image magnification M and the photon count rate. The latter follows the distance-squared law. M is defined by the ratio of the source-object distance (SOD) and the source-detector distance (SDD) (for cone beam geometry only).

$$M = \frac{SDD}{SOD} \tag{2.4}$$

The pixel size of a projection and hence the reconstructed voxel (***vo****lumetric* *pi****xel***) size a_{voxel} is the ratio between the detector's pixel pitch $pixel_{pitch}$ and the

magnification.

$$a_{voxel} = \frac{pixel_{pitch}}{M} = pixel_{pitch} \cdot \frac{SOD}{SDD} \tag{2.5}$$

The voxel size is equal to the theoretically best spatial image resolution. However, the real spatial resolution of a tomogram is decreased by several factors, such as image artefacts, discussed in section 2.3, noise in the detector signal, and image blurring due to a non-point-like source. The blurring increases with the magnification and the diameter of the focus spot, while the signal-to-noise ratio decreases with increasing diameter of the focus spot due to a higher photon flux. In general, the diameter of the focus spot has to be smaller than a_{voxel}.
For the reduction of noise, both the offset and the gain images are used to correct every projection. The offset is a detector image without radiation, *i.e.* the so-called dark image. The gain is a detector image with X-ray radiation but without sample in the beam, *i.e.* the so-called bright image or flat-field.

2.3.2 Synchrotron Radiation Computed Tomography

A synchrotron is a storage ring for highly accelerated electrons. The electrons are primary accelerated by a linear accelerator up to 99 % of the speed of light ($c \simeq 3 \cdot 10^8$ m/s). The accelerated electrons are injected into the electron storage ring, a tube under ultra high vacuum consisting of alternating straight segments (*i.e.* insertion devices such as wiggler or undulator) and bending magnets forcing the electrons on a circular trajectory. Being accelerated within a wiggler, an undulator, or an bending magnet, the electrons emit a part of their energy in the form of X-ray photons. The beam of synchrotron X-ray radiation exhibits a high intensity. The beam can be monochromised for imaging purposes. The beam can also be considered parallel (the distance between source and detector is in the range of several tens of meters, and the angular spread is inherently small) and coherent (all X-ray photons are emitted simultaneously). These beam properties lead to a higher image quality compared to laboratory CT. The above described beam hardening artefact is avoided by a monochromatic beam. The cone-beam artefact is also suppressed, since a parallel beam is used. Based on the mentioned advantages, synchrotron radiation has application in high spatial and high time resolution investigation for small samples in the millimetre range.
The radiation is detected by a scintillation screen converting the X-ray photons

into visible light. An objective behind the scintillation screen enables image magnification. The image is acquired by means of a CCD-camera.

2.4 Diffraction-based Residual Stress Determination

Stress occurs in general in all materials. In the frame of this thesis, residual stress (RS) is caused by an inhomogeneous distortion in the metal lattice, induced by mechanical or thermal load. Such stress is the one that remains in the material even without external load. This section is based on [141–144].
Stress is described as a second rank tensor and is therefore often visualised as an ellipsoid. The three values on the diagonal entries σ_{11}, σ_{22}, σ_{33} describe the stress components normal to the surfaces of a unit cube, as shown in Figure 2.6. The values off-diagonal represent the shear stress components.

$$\overline{\overline{\sigma}} = \begin{pmatrix} \sigma_{11} & \sigma_{12} & \sigma_{13} \\ \sigma_{21} & \sigma_{22} & \sigma_{23} \\ \sigma_{31} & \sigma_{32} & \sigma_{33} \end{pmatrix} \tag{2.6}$$

Since each component describes the force acting on the cube surface area ($|F_{i,j}| = A \cdot \sigma_{i,j}$), the stress tensor describes the force acting on a unit cube of material. A visual description is the following: if a unit cube would be cut out of a sample, the cube would distort according to the stress tensor at this very position. The distortion can be separated into a volumetric and a deviatoric term. The volumetric stress leads to a change in the cube's volume, while the deviatoric stress induces a change of the cube's shape without a change in volume.
RS is commonly sub-divided in Type I, Type II and Type III stress, see Figure 2.6b. Type I stress is also called macroscopic stress, as it describes the stress at the sample scale. Type II stress describes the inter-granular stress and is observed therefore at the grain-size scale. Type III stress describes intra-granular stress and is found only within grains. Based on the different length scale, every type has a different boundary condition:

$$\int_{sample} \sigma_{TypeI}(V)dV = 0 \tag{2.7}$$

$$\int_{severalgrains} \sigma_{TypeII}(V)dV = 0 \tag{2.8}$$

$$\int_{singlegrain} \sigma_{TypeIII}(V)dV = 0 \tag{2.9}$$

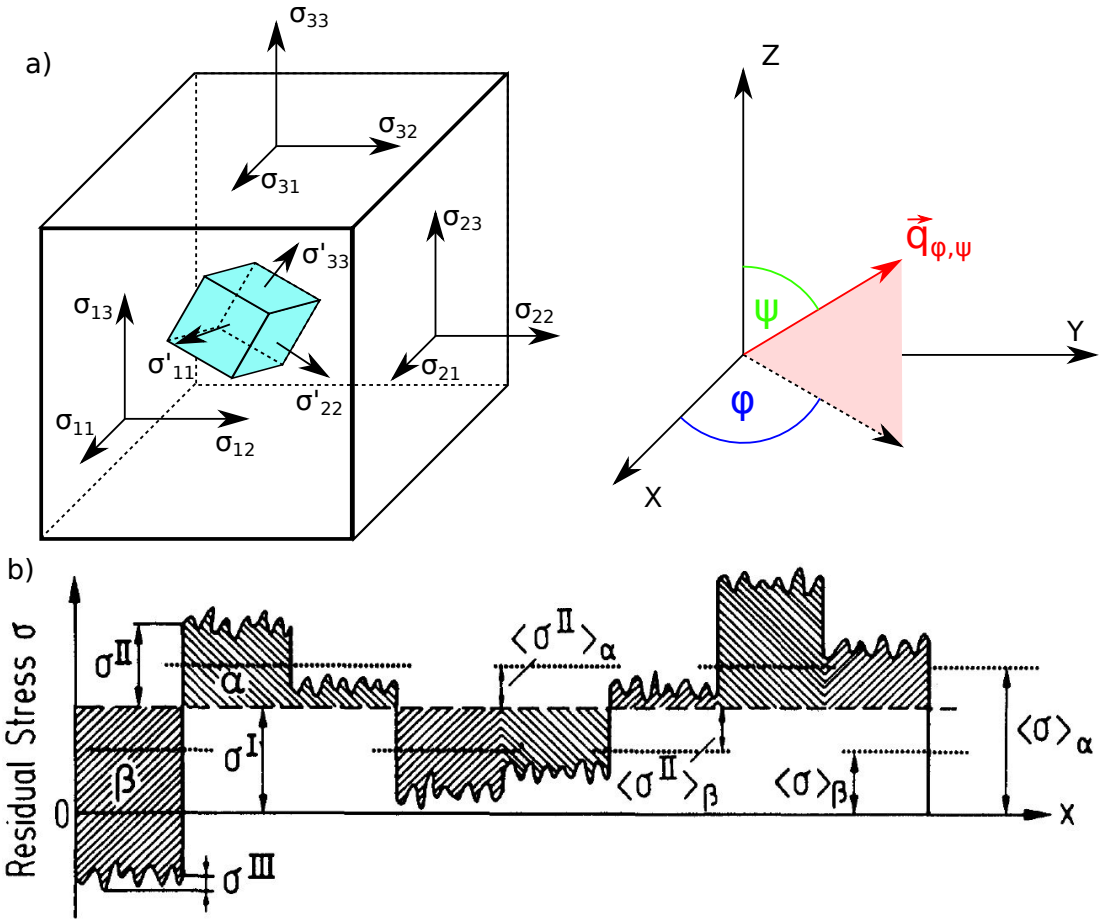

Figure 2.6: a) The nine stress component are sketched for a cube sample (left). The small and turquoise cube indicates the orientation at which the shear stresses would vanish, *i.e.* the principal stress orientation. The scattering vector is presented in the sample coordinate system (right) and is defined by the azimuth angle ϕ and the polar angle ψ. b) An illustration of the three types of RS taken from [145] indicates the different length scale of each RS type.

The determination of the residual stress state is equivalent to the determination of the nine stress components in equation 2.6. Since the symmetry of the unit cube induces a symmetric tensor ($\sigma_{12} = \sigma_{21}$, $\sigma_{13} = \sigma_{31}$, $\sigma_{23} = \sigma_{32}$), only six stress components are independent. The measurement of six independent directions is therefore needed to estimate the full tensor.
The estimation of residual stress by diffraction is based on the Bragg's Law:

$$n\lambda = 2 \cdot d^{hkl} \cdot \sin\left(\theta^{hkl}\right) \tag{2.10}$$

with n being the order of constructive interference maxima ($n = 1$ in most of the cases), λ being the wavelength and θ^{hkl} being the Bragg's angle under which the constructive interference maxima is observed. With the aim to calculate the lattice spacing d^{hkl} for the corresponding lattice planes described by the Miller indices h, k, l, the measurement can be performed in either angle- or energy-dispersive modes (using $E = {}^{hc}/_{\lambda}$ in the latter case). Once d^{hkl} is known, the strain is calculated by use of an unstrained reference value d_0^{hkl}.

$$\epsilon^{hkl} = \frac{d^{hkl} - d_0^{hkl}}{d_0^{hkl}} = \frac{d^{hkl}}{d_0^{hkl}} - 1 = \frac{\sin\left(\theta_0^{hkl}\right)}{\sin\left(\theta^{hkl}\right)} - 1 \tag{2.11}$$

The strain tensor is converted to stress by Hooke's Law:

$$\overline{\overline{\sigma}} \;=\; \mathbf{C} \cdot \overline{\overline{\epsilon}} \tag{2.12}$$

which in its isotropic variant reads: .

$$\begin{pmatrix} \sigma_{11} \\ \sigma_{22} \\ \sigma_{33} \\ \sigma_{12} \\ \sigma_{13} \\ \sigma_{23} \end{pmatrix} = \frac{E}{(1+\nu)(1-2\nu)} \begin{pmatrix} 1-\nu & \nu & \nu & 0 & 0 & 0 \\ \nu & 1-\nu & \nu & 0 & 0 & 0 \\ \nu & \nu & 1-\nu & 0 & 0 & 0 \\ 0 & 0 & 0 & \frac{1-2\nu}{2} & 0 & 0 \\ 0 & 0 & 0 & 0 & \frac{1-2\nu}{2} & 0 \\ 0 & 0 & 0 & 0 & 0 & \frac{1-2\nu}{2} \end{pmatrix} \begin{pmatrix} \epsilon_{11} \\ \epsilon_{22} \\ \epsilon_{33} \\ 2\epsilon_{12} \\ 2\epsilon_{13} \\ 2\epsilon_{23} \end{pmatrix} \tag{2.13}$$

The "elastic Modulus" E^{hkl} and the "Poisson ratio" ν^{hkl} are often used to describe the elastic behaviour of the lattice family h, k, l measured by means of diffraction (see equations 2.10 and 2.11). For the sake of brevity, no variable is superscripted by h, k, l in equation 2.13. The use of Hooke's law leads to a determination of

only the elastic stress.
It is important to note, that due to the format of the stiffness tensor $\mathbf{C}$, three stress components (σ_{11}, σ_{22} and σ_{33}) can always be calculated as long as three respective perpendicular strain components (ϵ_{11}, ϵ_{22} and ϵ_{33}) were determined, even though they do not correspond to the principal stress directions.
The estimation of principal stress components requires the knowledge of all six independent stress components (σ_{11}, σ_{22}, σ_{33}, σ_{12}, σ_{13}, σ_{23}) and hence the measurement along $N \geq 6$ independent strain directions $\epsilon_{\phi,\psi}$, where ϕ is the azimuth angle and ψ the polar angle of the scattering vector with respect to the sample coordinate system, see Figure 2.6. Each measured strain component can be described as following.

$$\begin{aligned} \epsilon_{\phi_n,\psi_n} &= \epsilon_{11}\cos^2\phi_n \sin^2\psi_n + \epsilon_{22}\sin^2\phi_n \sin^2\psi_n + \epsilon_{33}\cos^2\psi_n \\ &\quad +\epsilon_{12}\sin(2\phi_n)\sin^2\psi_n + \epsilon_{13}\cos\phi_n \sin(2\psi_n) + \epsilon_{23}\sin\phi_n \sin(2\psi_n) \\ &\quad \text{with} \qquad n = (1, ..., N) \end{aligned} \tag{2.14}$$

With the assumption of an isotropic material and the use of the Kronecker delta δ_{ij}, the relation

$$\epsilon_{ij} = \frac{1+\nu}{E}\sigma_{ij} - \delta_{ij}\frac{\nu}{E}\sigma_{kk} \tag{2.15}$$

can be inserted into equation 2.14 which yields

$$\begin{aligned} \epsilon_{\phi_n,\psi_n} &= \frac{1+\nu}{E}\left(\sigma_{11}\cos^2\phi_n + \sigma_{12}\sin^2(2\phi_n) + \sigma_{22}\sin^2\phi_n - \sigma_{33}\right)\sin^2\psi_n \\ &\quad +\frac{1+\nu}{E}\sigma_{33} - \frac{\nu}{E}\left(\sigma_{11}+\sigma_{22}+\sigma_{33}\right) \\ &\quad +\frac{1+\nu}{E}\left(\sigma_{13}\cos\phi_n + \sigma_{23}\sin\phi_n\right)\sin(2\psi_n) \qquad (2.16) \\ &\quad \text{with} \qquad n = (1, ..., N) \qquad (2.17) \end{aligned}$$

For $N \geq 6$ the linear system can be solved for σ_{11}, σ_{22}, σ_{33}, σ_{12}, σ_{13} and σ_{23} to fill the stress tensor $\overline{\overline{\sigma}}$ (equation 2.6). The eigenvalues λ_i and the eigenvectors v_i, representing the principal stress values and the principal stress directions, respectively, are estimated by solving the equation

$$\left(\overline{\overline{\sigma}} - \lambda_i \mathbf{I}\right) \cdot v_i = 0 \qquad \text{for } i = 1, 2, 3 \tag{2.18}$$

I is the second-rank unit tensor. The diagonalization corresponds to a physical rotation of the sample coordinate system (which is equal to a change of basis for the stress-tensor $\overline{\overline{\sigma}}$). All shear stress components can be neglected in principal stress condition.

$$\begin{pmatrix} \sigma_{11} & \sigma_{12} & \sigma_{13} \\ \sigma_{21} & \sigma_{22} & \sigma_{23} \\ \sigma_{31} & \sigma_{32} & \sigma_{33} \end{pmatrix} = (v_1, v_2, v_3) \begin{pmatrix} \lambda_1 & 0 & 0 \\ 0 & \lambda_2 & 0 \\ 0 & 0 & \lambda_3 \end{pmatrix} (v_1, v_2, v_3)^{-1} \tag{2.19}$$

The diagonalized tensor describes the same stress state than $\overline{\overline{\sigma}}$ since the stress-invariants I_1, I_2 and I_3 are the same:

$$\begin{aligned} I_1 &= \mathrm{Tr}\left(\overline{\overline{\sigma}}\right) = \sigma_{11} + \sigma_{22} + \sigma_{33} = \lambda_1 + \lambda_2 + \lambda_3 && (2.20) \\ I_2 &= \frac{1}{2}\left(\mathrm{Tr}\left(\overline{\overline{\sigma}}\right)^2 - \mathrm{Tr}\left(\overline{\overline{\sigma}}^2\right)\right) = \sigma_{11}\sigma_{22} + \sigma_{11}\sigma_{33} + \sigma_{22}\sigma_{33} - \sigma_{12}^2 - \sigma_{13}^2 - \sigma_{23}^2 \\ &= \lambda_1\lambda_2 + \lambda_1\lambda_3 + \lambda_2\lambda_3 && (2.21) \\ I_3 &= \det\left(\overline{\overline{\sigma}}\right) = \sigma_{11}\sigma_{22}\sigma_{33} + 2\sigma_{12}\sigma_{13}\sigma_{23} - \sigma_{11}\sigma_{23}^2 - \sigma_{22}\sigma_{13}^2 - \sigma_{33}\sigma_{12}^2 \\ &= \lambda_1\lambda_2\lambda_3 && (2.22) \end{aligned}$$

$\mathrm{Tr}\left(\overline{\overline{\sigma}}\right)$ and $\det\left(\overline{\overline{\sigma}}\right)$ means the trace and the determinant of the stress-tensor, respectively.
The diffraction based techniques used to determine the lattice spacing according to equation 2.10 are divided according to the kind of primary radiation. Neutron diffraction and X-ray diffraction are therefore described in the two following subsections.

2.4.1 Neutron Diffraction

Neutrons for research purpose can be produced in two different ways: firstly, steady state sources (*i.e.* research reactors), and secondly, pulsed sources. In this work, only steady state sources were used.
Interestingly, the total world-wide power of all 250 research reactors is slightly higher than the power provided by one single power reactor (3000 MW) [146].
In most cases thermal neutrons are used for ND. Thermal neutron have a kinetic energy around 25 meV. That corresponds to room temperature. The hot neutrons (high kinetic energy) created by fission are slowed down by a moderator. The moderator is typically heavy water (hydrogen is replaced by deuterium in

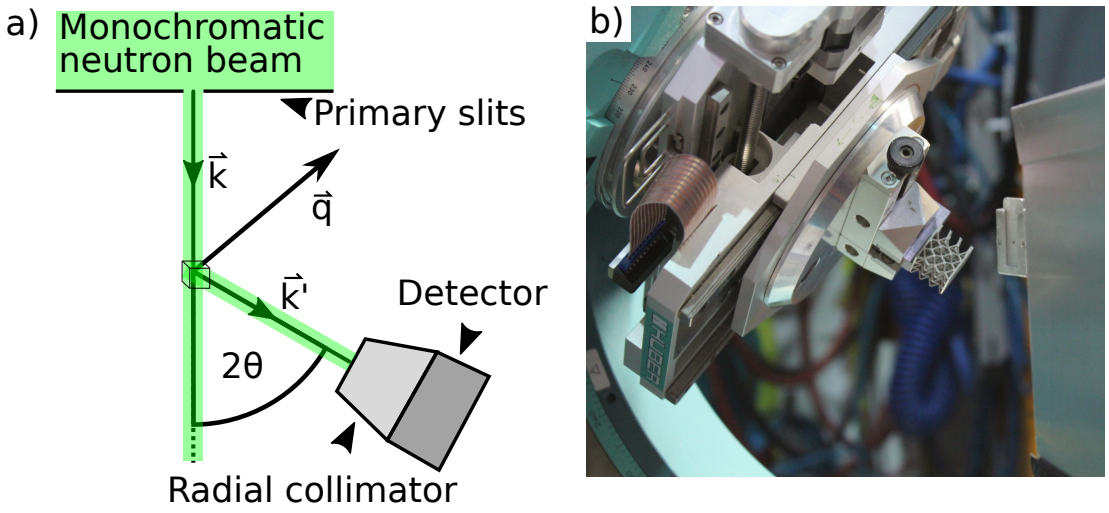

Figure 2.7: a) A schematic of the ND experiment with the incoming beam $\vec{k}$, the diffracted beam $\vec{k'}$, and the scattering vector $\vec{q}$ and b) the ND setup at Stress-Spec beamline at FRMII neutron reactor, Garching, Munich

water molecules).

The gauge volume is defined by the intersection between primary beam and secondary beam. Both are defined by either a radial collimator or a horizontal and vertical slit system. An oscillating radial collimator allows one to reduce the beam divergence.

An array (1D or 2D) detector is used to capture the diffracted neutrons. Neutron detectors are based on nuclear interactions as neutrons are not a directly ionising radiation. The sample is translated and rotated through the pre-defined gauge volume and a section of the Debye diffraction-rings is detected in the case of a poly-crystalline material. A polar integration is used to transform the 2D ring segment into a 1D diffraction peak.

2.4.2 X-ray Diffraction

Laboratory X-ray diffraction uses the same principles as described above but X-rays as a primary radiation. X-ray photons interact with the atomic shell rather than with the nucleus. Therefore, the penetration depth into metals is significantly lower for X-rays compared to neutrons. While neutrons penetrate into the bulk material, X-rays are used to measure the surface stresses in a non-destructive manner. A penetration depth up to 10 μm [99] justifies the assumption of a negligible stress component normal to the surface ($\sigma_{33} = 0$). However, the

low penetration depth induces a need for a highly precise surface alignment. A tactile surface alignment is carried out for every measurement point to avoid the influence of surface waviness.
Under the assumption of negligible shear stresses along the two direction $\phi = 0°$ and $\phi = 90°$ equation 2.17 simplifies to .

$$\frac{d^{hkl}_{0°,\psi} - d^{hkl}_0}{d^{hkl}_0} = \frac{1+\nu}{E}\left[(\sigma_{11}-\sigma_{33})\sin^2\psi+\sigma_{33}\right] - \frac{\nu}{E}(\sigma_{11}+\sigma_{22}+\sigma_{33}) \quad (2.23)$$

$$\frac{d^{hkl}_{90°,\psi} - d^{hkl}_0}{d^{hkl}_0} = \frac{1+\nu}{E}\left[(\sigma_{22}-\sigma_{33})\sin^2\psi+\sigma_{33}\right] - \frac{\nu}{E}(\sigma_{11}+\sigma_{22}+\sigma_{33}) \quad (2.24)$$

The measured lattice spacings $d^{hkl}_{\phi,\psi}$ depends linearly on $\sin^2(\psi)$ according to equation 2.23 and 2.24. It becomes clear that the $\sin^2\psi$-method allows the estimation of stress differences, only. In combination with the assumption $\sigma_{33} = 0$ in the case of planar, stress the differences $\sigma_{11} - \sigma_{33}$ and $\sigma_{22} - \sigma_{33}$ become σ_{11} and σ_{22}, respectively. The knowledge of d^{hkl}_0 up to a few hundredth of an Ångstrom is sufficient for XRD.

$$\sigma_{11} = \frac{1}{d_0}\cdot\frac{1+\nu}{E}\frac{\partial d^{hkl}_{0°,\psi}}{\partial\sin^2\psi} \quad (2.25)$$

$$\sigma_{22} = \frac{1}{d_0}\cdot\frac{1+\nu}{E}\frac{\partial d^{hkl}_{90°,\psi}}{\partial\sin^2\psi} \quad (2.26)$$

3 Powder Characterisation

Powder is the feedstock for the L-PBF process. In order to understand the process and to improve the quality control of L-PBF, the first step is powder characterisation. A deep understanding of the powder characteristics is indispensable since they have a significant impact on wide variety of properties of the final part [17]. Powder particles are characterised and certified by the producer in terms of the particle size. Sieving and laser diffraction are commonly used for such a certification [128]. However, this particle size becomes meaningless after the first use of the powder batch since particle agglomeration influences the mean size and shape of the used powder. Both techniques, sieving and LD, provide information about the particle size only. Since the quantification of particle shape is complex, it should be characterised in three dimensions for more representative information [28]. CT is a common tool for volumetric powder characterisation [29]. Greater statistical information (*i.e.* larger number of particles) is gained by CT, compared with 2D imaging techniques including optical microscopic analysis [25]. The application of image processing routines on CT data enables the evaluation of different size parameters (*e.g.* the equivalent diameter, the circumsphere diameter, the dimension of the bounding box) and shape factors of powder particles [29, 147].

This chapter is split into two parts. The first describes the workflow developed to evaluate the size, the shape, the packing density, and the inter-particle distance of the powder in the example of a IN 625 powder batch. As described in chapter 1, IN 625 lattice structures will be investigated below. Besides providing a workflow for particle segmentation and powder analysis by means of synchrotron CT, the second part of this chapter tackles correlations of particle size and shape with the packing density of the powder bed. The workflow is tested on two different kind of powder batches. The stainless steel AISI 316L and the Ti-6Al-4V powder batches were produced by means of gas and plasma atomisation, respectively. The differences and similarities will be discussed.

The experiment, the workflow, and a part of the results presented in the following chapters are published in [148].

3.1 Experiment

Synchrotron CT was used for the characterisation of AM powder particles thanks to its high resolution and reduced image artefacts compared to lab-CT [149] (see subsections 2.3.1 and 2.3.2).
Two different sample preparation were used. In the first, the powder particles were filled into a glass capillary with a diameter of 1 mm. In the second the powder particles were filled into two-component liquid adhesive (epoxy plus binder). After solidification of the epoxy matrix, solid samples with dimensions of 3 mm × 3 mm × 10 mm were obtained.
The synchrotron CT experiments were carried out at the BAMline at the synchrotron radiation facility BESSY II (Helmholtz Zentrum, Berlin, Germany) [150]. The energy of the monochromatic and parallel beam was varied between 40 keV and 50 keV (depending on the material) to achieve at least 10 % transmission on each sample. An effective pixel size of 0.876 μm was achieved by using a 5x microscope objective (Olympus, Hamburg, Germany) and a CCD-based camera (4000 × 2760 pixels, PCO, Kelheim, Germany). The spatial resolution for one radiography was measured with a JIMA RC-02 resolution chart [151] to be 1 μm. The distance between the scintillator screen and the object was 10 mm. Three thousand projections over a range of 180° were acquired for each measurement. Each projection had an integration time of 3 s. 10 flat-field images were acquired after every 100 projections and were averaged. This average flat field was used to correct the subsequent 100 projections. The volume data were reconstructed from the projections by first applying Paganin's phase retrieval algorithm (with $\beta/\delta = 0.027$) [152] and, subsequently, the filtered back-projection algorithm for parallel beam geometry [135]. In-house developed software was used.

3.2 Workflow for Powder Characterisation by CT

The following workflow is developed to extract the particle packing density, the inter-particle distance, the particle shape, the particle size, and the porosity within the powder particles with a sufficient particle statistic from one acquisition.
The reconstructed raw data are represented in Figure 3.1a. Ring artefacts (as described in chapter 2.3) are visible in Figure 3.1a and are corrected by a filter [140] implemented in *ImageJ* [153]: After a transformation into cylindrical

coordinates, the ring artefacts appear as stripes and are filtered by a wavelet filter. The result is shown in Figure 3.1b. A bilateral filter is used for noise reduction [154]. The bilateral filter is defined as a weighted average of pixels. It takes into account not only the spatial distance of pixels but also the variation in their grey values. Therefore, the bilateral filter allows the suppression of noise while preserving the edges of objects (*e.g.* the particles). The following filter parameters provide the optimal combination of de-noising and edge preservation: a spatial distance kernel of 7 pixels and a grey value range kernel of 50 (in a total scale of 256 grey values), see Figure 3.1c. Afterwards a binary mask of the powder particles is created by application of the automatic grey value threshold implemented in ImageJ. The final threshold value is defined by the iterative procedure based on the ISO data algorithm, which has first been introduced in [155]. Figure 3.1d shows the resulting binary image after global thresholding. The voids (*i.e.* porosity) *within* the powder particles are artificially suppressed at this step of the workflow, as they would disturb the successive watershed segmentation as well as the analysis of the inter-particle distance (described below in this chapter). The porosity analysis is performed on the filtered grey value distribution shown in Figure 3.1c and is therefore not influenced by suppression of the inner voids after the binarisation.

The majority of the powder particles are physically connected and need to be separated during image analysis for quantification. A widely used approach for particle recognition and separation is the watershed segmentation algorithm [156]. This algorithm searches first for seed points by determination of local maxima of the 3D distance map of the binarised pixel mask, see Figure 3.1e. A virtual watershed rises (in grey value) from these seed points. As soon as the waterfronts from two different seed points are touching each other, this voxel where they met is defined as background. The search for seed points is highly sensible to concavities of particles. An advanced watershed approach for 3D particle recognition (implemented plug-in in ImageJ) that tolerates particle concavities was applied [156], see Figure 3.1f.

The novel idea implemented here, which differs from the conventional watershed, is the use of an additional controlling parameter k for limitation of the separation $0 \leq k \leq 1$. $k = 1$ corresponds to the conventional watershed separation and $k = 0$ would lead to no separation [156]. k is the ratio between the particle's diameter and the length of the contact line along which two particles are touching.

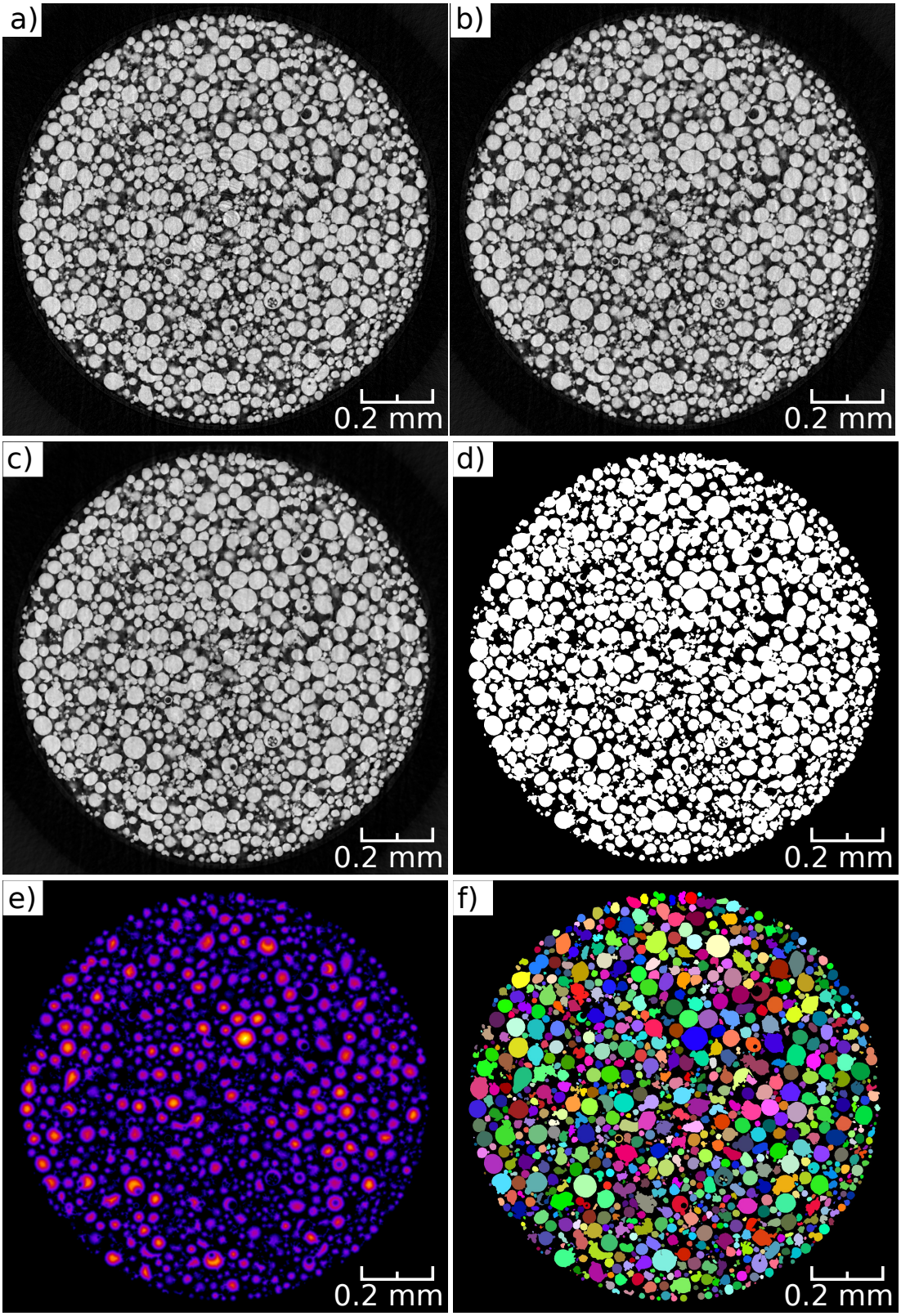

Figure 3.1: Representation of the particle segmentation work-flow. The same tomogram is shown in successive steps of image analysis: a) raw data, b) ring artefact correction, c) bilateral filter, d) binarised pixel mask, e) 3D distance map of the pixel mask (each local maxima represents a seed point), f) particle separation based on the seed point from e) (advanced watershed algorithm with $k = 0.7$).

This helps avoiding the over-separation, which occasionally takes place in conventional watershed algorithms, for which any concavity of the particle surface leads to separation. For the analysed datasets, the best segmentation result with the minimum amount of improper fragmentations was achieved with $k = 0.7$, see Figure 3.1f. Examples of under- ($k = 0$) and over-separation ($k = 1$) are shown in Figure 3.2a and b, respectively. While in Figure 3.2a too many particles are attached together, in Figure 3.2b even whole and solid particles are separated.

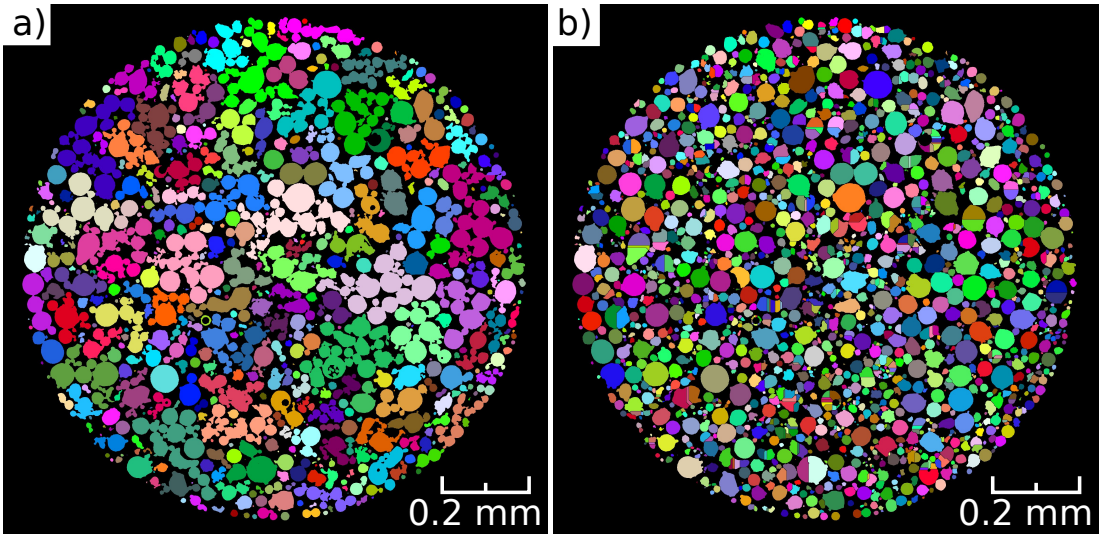

Figure 3.2: An example for a) under-separation of particles $k = 0$ b) and over-separation of particles $k = 1$ is presented.

First tests of different watershed algorithms revealed certain artefacts in the size distribution. While an over-segmentation leads to a significant peak for small particles, an under-segmentation induces a peak for large particles. This problem is solved by application of the advanced watershed and adapting the fragmentation parameter k until the size distribution shows neither of the two artefacts. Figure 3.3a illustrates the described peaks and show also the assumed log-normal distribution of the particles.
Separated powder particles are the basis of the following analysis regarding particle packing density, inter-particle distance, porosity within the powder particles, particle size and particle shape.

1. Particle packing density
The particle packing density (PD) is defined by the ratio of the volume assigned to the particles and the total evaluated volume of the glass capillary. The PD is

assumed to vary within the glass capillary [157, 158]. Therefore variously sized and positioned region of interest (ROI) are chosen for the minimisation of the statistical error. PD depends strongly on the surface determination, as each material voxel is counted. Based on experience, the advanced surface determination tool implemented in VG studio MAX 3.2 (Volume Graphics, Heidelberg, Germany) is chosen for the estimation of PD. In addition to various global grey value surface thresholds, the advanced surface determination considers the local grey value gradient at each point. The initial surface is estimated by a global grey value threshold. This surface is iteratively improved. It each point of this initial surface, the grey value distribution is searched for the point of inflection. This is used as the final surface. In this way, surface determination depends less on the absolute grey values, and the reproducibility is assured. Since the voids within the particles would bias the evaluation of PD, all internal porosity is artificial suppressed for the evaluation of the PD. Five ROIs are extracted and evaluated from the data set, Figure 3.3b. This leads to a PD of 0.60 ± 0.005 for IN 625.

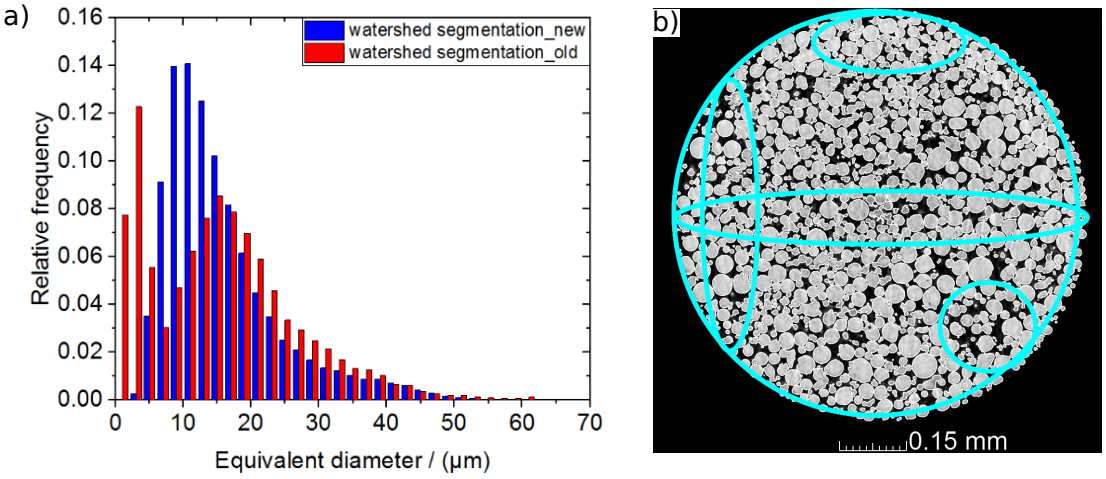

Figure 3.3: a) The particle size distribution for powder particles segmented with conventional (red) and with advanced (blue) watershed segmentation and b) a tomogram of the IN 625 powder sample in glass with the investigated ROIs for the powder packing density.

2. Inter-particle distance

The inter-particle distance describes the size of the smallest voids between the particles within the powder bed. It provides more detailed information about the arrangement of the particles than PD does. The inter-particle distance is es-

timated by the application of a cylindrical mask (grey value = 0 inside and grey value = 255 outside of the glass capillary) on the binary volume of Figure 3.1d). One obtains an inverted image, as shown in Figure 3.4a. A 3D distance transform is applied to Figure 3.4a resulting in Figure 3.4b. The 3D distance transform assigns each voxel to the value of the smallest Euclidean distance (in 3D) to a voxel in the material. Therefore, all voxels assigned to the material acquire the value = 0. The statistical analysis of the 3D distance map, see Figure 3.4c, illustrates the distribution of voxels within the inter-particle voids. A maximum inter-particle distance of 13 μm was found for the IN 625 powder batch. As this value represents the shortest distance to a material voxel, the same void space is available in every direction. A sphere with a diameter of at most 26 μm would fit in such a void.

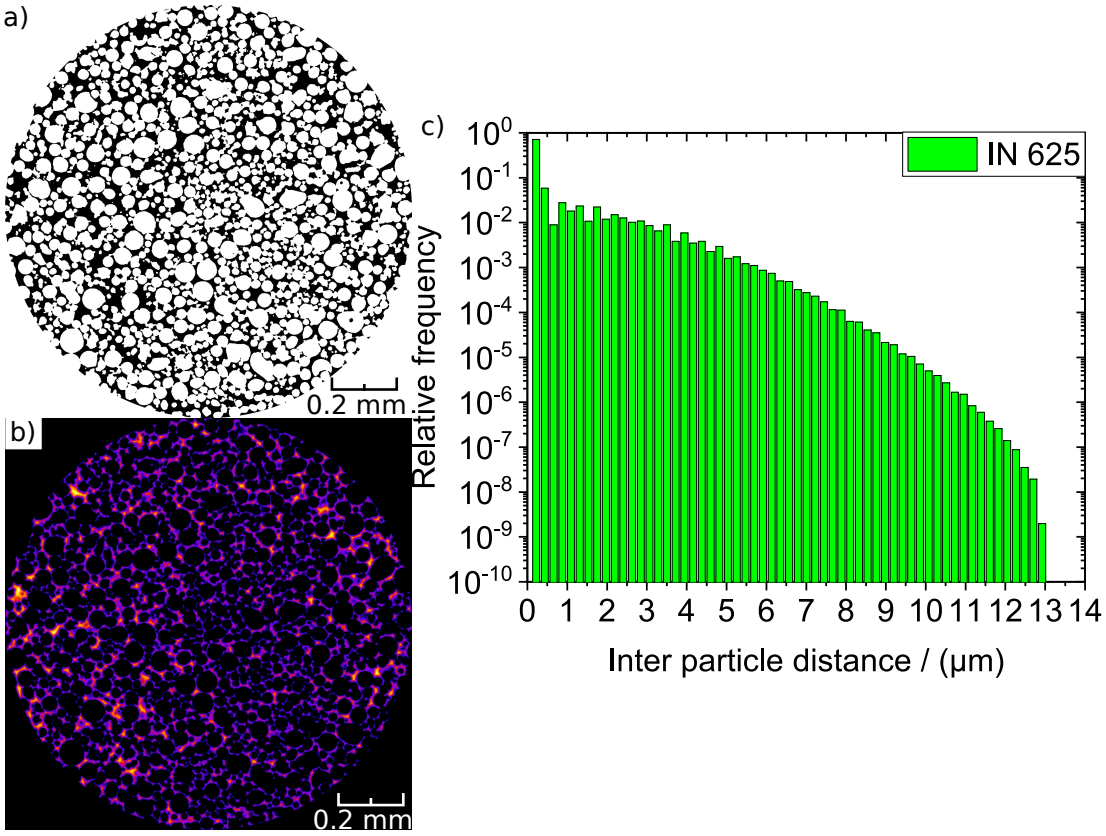

Figure 3.4: a) The binary volume is based on the presented Figure 3.1d). The background outside of the glass cylinder was inverted by a cylindrical mask. b) presents the 3D distance transformation of 3.4a. The result of a statistical analysis of the distance is shown c).

3. Particle porosity

The porosity within the particles is evaluated using the the VGdefX algorithm implemented in VG studio MAX 3.2. The volume fraction of porosity is very small (0.05 % for the IN 625 powder). The size distribution of the detected porosity is presented in Figure 3.5a in form of the circumsphere diameter. This presentation of size is the most conservative (see the following paragraph). The mean pore size within the powder particles is found to be 5 μm with a standard deviation of 3 μm (and only a few instances above 20 μm). However, open porosity filled with smaller powder particles, as shown in Figure 3.5b, are found twice (see also [159]). The effect of such irregularities, or 'pregnant particles', on the mechanical behaviour of the processed part is not clear yet.

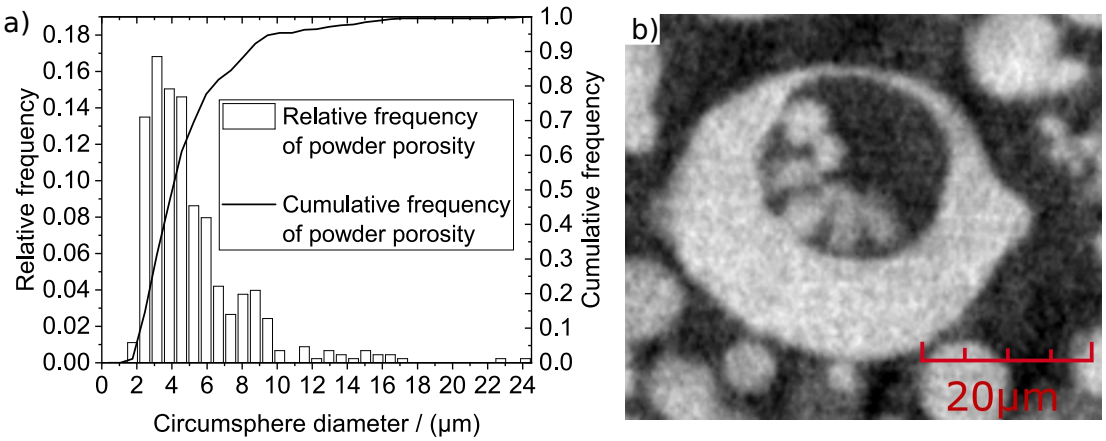

Figure 3.5: a) The porosity size distribution by means of the circumsphere diameter in the form of relative frequency (left axis, hollow bars) and the cumulative frequency (right axis, solid line) and b) a open pore in a large particle is filled with smaller particles

4. Particle size

The size of a particle can be described is different ways. The volume is the most precise one but is rarely used since it reveals no information about the dimensions of the particle. Therefore, the equivalent diameter is defined as the diameter of a sphere with the same volume as the particle would have, see equation 3.1.

$$d_{eq} = \sqrt[3]{\frac{3 \cdot V_{particle}}{4\pi}} \tag{3.1}$$

Another tool to estimate the size of a particle is the diameter of the circumsphere

d_{cs}. Both diameters are influenced by the shape of the particle. The more sphere-like the particle is, the more precisely the dimensions of the particle are described by d_{eq} and d_{cs}. It is important to note, that $d_{eq} \leq d_{cs}$ always. d_{cs} is therefore the more conservative measurement of size.
If the particle is approximated by an ellipsoid, a principal component analysis (PCA) [160] is the method of choice to find the dimensions and orientation of the ellipsoid. The PCA provides the eigenvalues λ_1, λ_2, and λ_3 of the covariance matrix for each particle. The eigenvalues λ_1, λ_2, and λ_3 correlate with the diameters along the directions of the three eigenvectors of the covariance matrix of the grey value distribution of a particle [161]. The eigenvectors of the covariance matrix physically correspond to the axes of inertia of the particle. The PCA is implemented in VG studio MAX 3.2. However, it is neither intuitive nor well documented. For instance, it is not described how the estimated eigenvalues correspond to the diameter of the particle. The correlation between eigenvalue and diameter was carried out by analysis of simulated ellipsoids. Variously sized voxel-based ellipsoids were simulated, each in a binarised volume of $256 \times 256 \times 256$ voxel. These known ellipsoids are analysed by means of the PCA implemented in VG studio MAX 3.2. A proportionality factor of 0.225 was found between eigenvalues and diameter along the respective direction, see 3.6a.
This proportionality factor is then subsequently used to calculate the three diameters for the powder particles according to equation 3.2.

$$d_{length} = \frac{\sqrt{\lambda_1}}{0.225}, \qquad d_{width} = \frac{\sqrt{\lambda_2}}{0.225}, \qquad d_{height} = \frac{\sqrt{\lambda_3}}{0.225} \tag{3.2}$$

Since these three respectively orthogonal diameters can be understood as the bounding box around the particle [20, 21], see Figure 3.6b, they are labelled as:

d_{length} = largest diameter (corresponds to λ_1)
d_{width} = medium diameter (corresponds to λ_2)
d_{height} = smallest diameter (corresponds to λ_3)

d_{eq}, d_{cs}, d_{length}, d_{width} and d_{height} are calculated for the same volume of powder particles and compared in Figure 3.7a. The variables D_{10}, D_{50}, and D_{90} represent the value of the cumulative frequency at 0.1, 0.5, and 0.9, respectively. The cumulative frequencies are the integrals of the PSD given as an example in Fig-

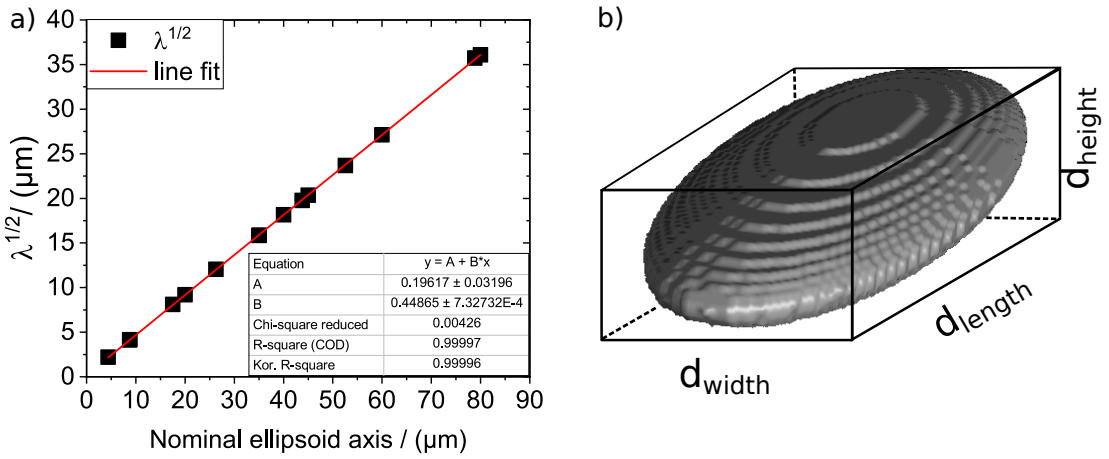

Figure 3.6: The dependence of the eigenvalues on the real dimension for simulated ellipsoids in a), the slope of the linear regression is used as proportionality factor. Sketched dimensions for a simulated ellipsoid are shown in b)

ure 3.7b for d_{eq}. The five different quantities are in reasonable agreement. The length and the circumsphere diameter define the upper edge while the height is the smallest dimension. The width and the equivalent diameter are very close to each other, as they both describe an average value for the powder sample. Figure 3.7a proves that d_{cs} is indeed the most conservative diameter to describe the size, as d_{cs} yields the largest value for the size.

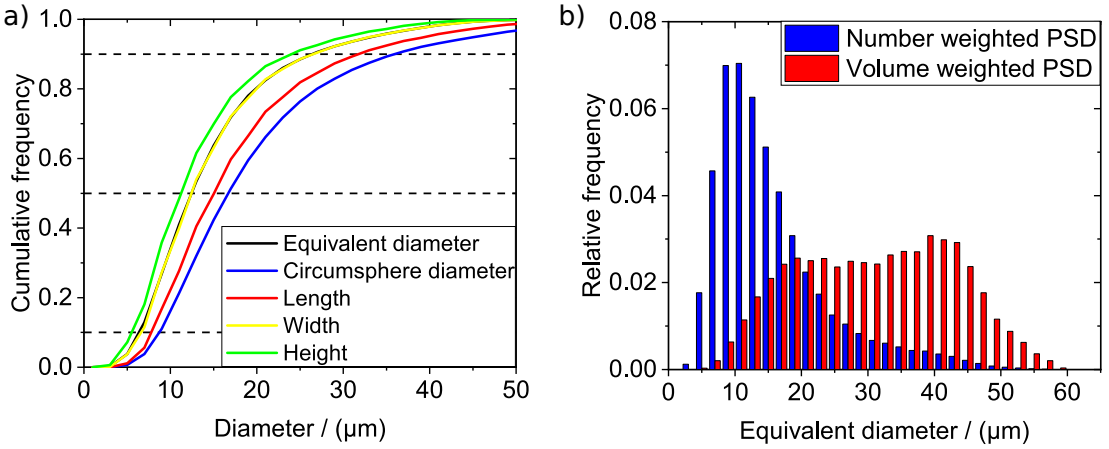

Figure 3.7: a) The cumulative size distribution is presented for d_{eq}, d_{cs}, d_{length}, d_{width} and d_{height} and b) the number weighted PSD is presented together with the volume weighted PSD as an example for d_{eq}

An important detail is the difference between the number weighted and the volume weighted PSD, see Figure 3.7b. The 3D analysis by means of CT allows the estimation of both PSDs, while other techniques such as sieving and laser diffraction provide results exclusively as a volume weighted PSD. The volume weighted PSD results in larger values for D_{10}, D_{50}, and D_{90}. For the sake of comparison this difference needs to be considered.

5. Particle shape

The shape of an object can be described by the best fitting regular geometries, *e.g.* a sphere, a cube, a cylinder, a pyramid, etc.). In case of AM powder particles, the ellipsoid, having the sphere as a special case, is a suitable regular object [20, 148].

Several parameter exist for shape analysis, similar to the particle size. Within this work the sphericity S and the anisotropy A are studied. While the assumption of an ellipsoidal particle is made for the estimation of the anisotropy, the sphericity takes into account only the particle's volume and surface. A is expressed by the ratio of the smallest (λ_3) and largest (λ_1) eigenvalue determined by PCA and is also named Feret diameter. A is calculated according to equation 3.3.

$$A = 1 - \frac{\lambda_3}{\lambda_1} \tag{3.3}$$

S is specified by the ratio between the surface area of a sphere with the same volume as the particle ($V_{particle}$), and the surface area of the particle ($A_{particle}$) itself, see equation 3.4.

$$S = \frac{\sqrt[3]{36\pi \cdot V_{particle}^2}}{A_{particle}} \tag{3.4}$$

The method is only meaningful, if the surface of the particle is not voxel-based but smoothed. These are described as 'discrete' and 'continuous', respectively, in the software Amira (2019.03, ZIB, Berlin, Germany). If VG studio MAX 3.2 is used for surface determination, the surface is also smoothed. In the case of an ideal spherical particle it would hold $A_{sphere} = 0$ and $S_{sphere} = 1$.

Even though both the anisotropy and the sphericity are generally used to describe the shape, the differences are significant between them, as shown in Figure 3.8a. The anisotropy is spread between 0 and 0.9 with a global maximum at 0.2, while

the sphericity shows values from 0.7 to 1 with a global maximum at 0.95. The two maxima agree well taking into account that $A_{sphere} = 0$ and $S_{sphere} = 1$. The spread of the distributions is also different. It indicates that the two parameters (anisotropy and sphericity) are sensitive to different characteristics of the shape. While the anisotropy is a measurement of the axes ratio (see equation 3.3), the sphericity is a measurement of the convexity (see equation 3.4). The sphericity is not very sensitive to a change of axis ratio of the particle, see 3.8b. The calculated sphericity describes very well the observed sphericity for the size range of the powder particles.

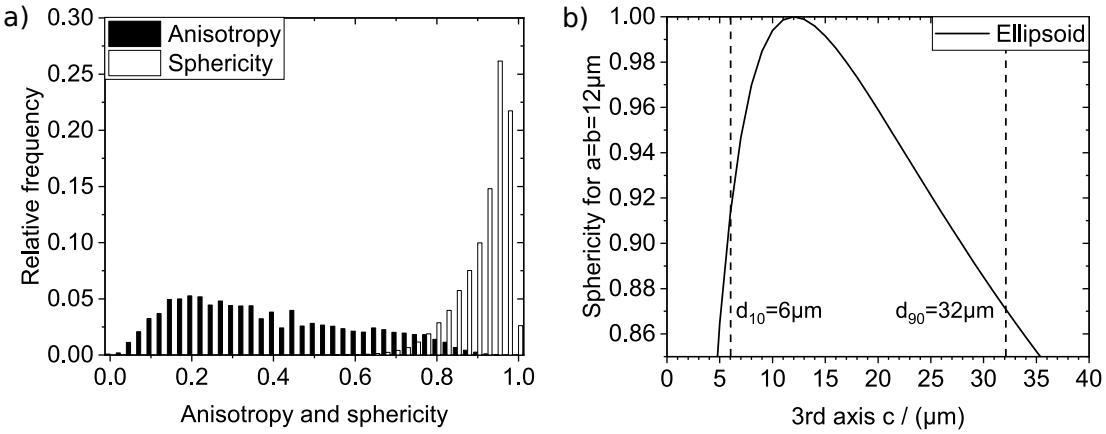

Figure 3.8: a) The sphericity (white) and the anisotropy (black) distribution of IN 625 powder particles and b) the theoretical trend of the sphericity in dependence of one axis for a perfect ellipsoid based on equation 3.4.

The parameters anisotropy and sphericity are not redundant but complementary. They lead to the conclusion that the characterised IN 625 powder particles are mostly convex but possess different axis ratios. This conclusion agrees with the visual impression of the particles (see Figure A.1), and justifies the description of the particles as ellipsoids and consequently the use of the PCA).

3.3 Discussion

The results show that the powder characterisation by means of Synchrotron CT is rich in information and statistics. The investigated volume considers 64000 powder particles. This corresponds to a material weight of 3 mg assuming the nominal density $\rho_{IN625} = 8.44\,\mathrm{g/cm^3}$ [128]. The presented workflow is also consistent for a variety of AM powder batches. In this way the comparison of *e.g.* gas

atomised powder and plasma atomised powder is possible [148]. Here the similarities and differences of three powder batches (IN 625, AISI 316L, and Ti64) shall be discussed to present the generalised nature of the workflow presented in chapter 3.2.

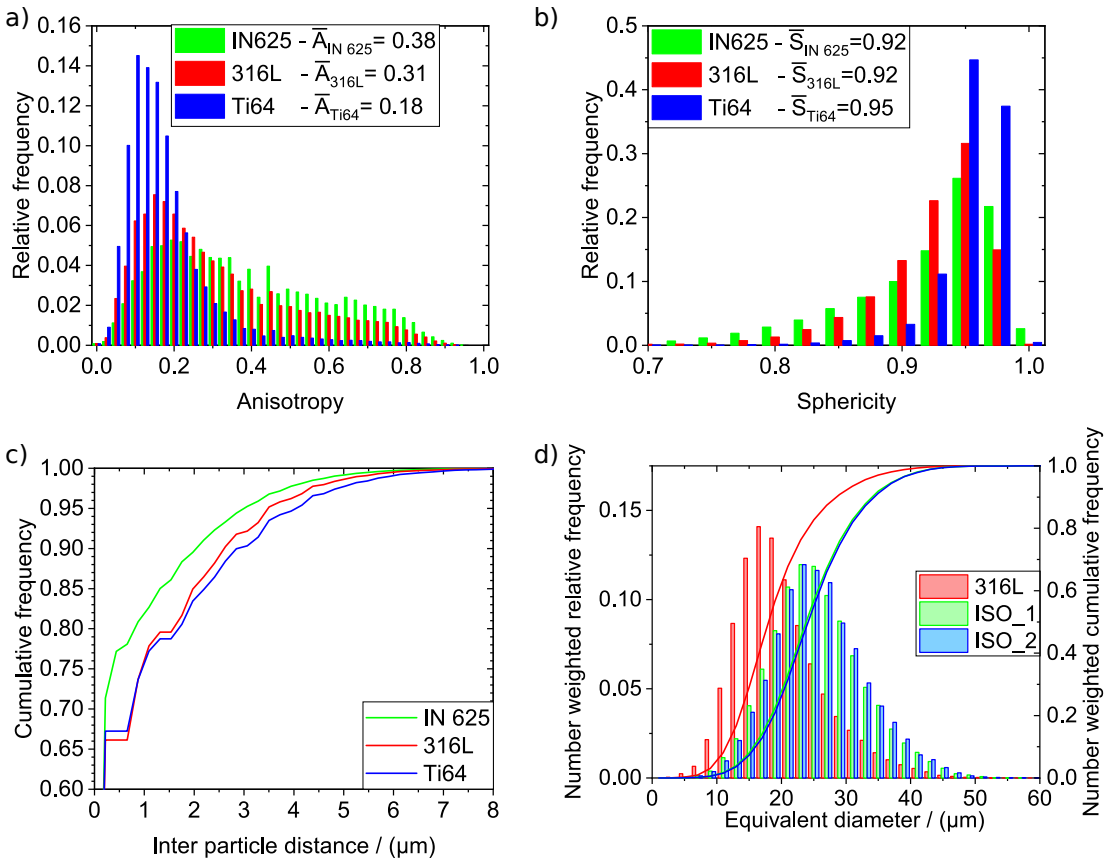

Figure 3.9: a) The anisotropy, b) the sphericity, and c) the inter-particle distance are presented for three powder batches IN 625 (green), AISI 316L (red) and Ti64 (blue). d) The PSD for the steel powder batch. The sampled powder was extracted from the batch according to ISO standard 3954 [162]. ISO_1 and ISO_2 represent the same epoxy sample at two different heights.

The powder bed quality can be accessed with knowledge about the packing density (PD), the inter-particle distance, and the particle shape. With $PD_{Ti64} = 0.561 \pm 0.003$ and $PD_{316L} = 0.576 \pm 0.004$ [148], it can be concluded that $PD_{IN625} > PD_{316L} > PD_{Ti64}$. The inter-particle distance shows the same trend. The difference $PD_{316L} - PD_{Ti64}$ is smaller than $PD_{IN625} - PD_{316L}$ and so is also the difference in inter-particle distance. The IN 625 powder particles shows the smallest inter-particle distance with the largest average anisotropy value.

The results of the shape analysis indicate that the influence of the particle shape on the PD is minor. The PD of 316L and Ti64 is nearly the same while the shape in terms of anisotropy is significantly different, see Figure 3.9a. IN 625 and AISI 316L display a comparable anisotropy and sphericity but they differ in PD. The maximum PD for ordered monodisperse spheres is known to be 0.74. For disordered monodisperse spheres, a PD of 0.635 has been reported [163]. In this work, polydisperse particle size distributions were discussed. Pednekar *et al.* have presented statistically equivalent bidisperse size distributions for log–normal size distributions [164].
The statistically equivalent bidisperse distribution was calculated for our polydisperse distributions according to Pednekar *et al.* [164], see table 3.1. The calculation is also presented in the appendix A.2. The radii ratio $\frac{D_S}{D_L}$ correlates with the PD, with D_S and D_L being the diameter of the smaller and the larger particles of the bidisperse distribution, respectively. The smaller radii ratio leads to a larger particle PD because the smaller particles fit into the voids between the larger particles. However, this shows that all three radii ratios are not small enough to allow an increase of PD compared to the nominal value of mono-disperse powder (0.635).

Table 3.1: Conversion from poly- to bidisperse particle size distribution

Powder	IN 625	316L	Ti64
Polydispersity α_{poly}	0.48	0.33	0.33
Skewness S_{poly}	1.54	1.03	1.02
Rel. amount of large particles	0.19	0.27	0.27
Rel. amount of small particles	0.81	0.73	0.73
Diameter of large particles D_L	$36.68\,\mu$m	$37.68\,\mu$m	$37.95\,\mu$m
Diameter of small particles D_S	$14.18\,\mu$m	$19.53\,\mu$m	$19.68\,\mu$m
Radii ratio $\frac{D_S}{D_L}$	0.39	0.52	0.52
Particle packing density	0.60 ± 0.005	0.576 ± 0.004	0.561 ± 0.003

It is obvious that the two shape parameters (anisotropy and sphericity) describe a different shape (see also below, Figure 3.9a and b). The sphericity is comparable for all three powder batches, while the anisotropy is different for Ti64. The shape of particles has to be understood as a 3D parameter. One shape parameter is not sufficient enough to describe the shape of the powder batch.

The two different sample preparations need to be discussed. In the case of powder in a capillary, the influence of the container size on the PD of the particles needs to be considered, as described in [157, 158]. These work dealt with mono- and bidisperse powders, respectively. Since the powder characterised above is neither mono- nor bidisperse, the mean size (20 μm, Figure 3.7) was taken to verify if on average, the right container size (1 mm) was used for the powder measurement. The ratio ($\frac{1000\,\mu m}{20\,\mu m}$) corresponds to McGeary's plateau of maximum theoretical PD, where the sample size was statistically representative [157]. Hettiarachchi *et al.* confirmed that the container wall effect can be neglected when the ratio between particle size and container size is less than 0.1 [158]. A container of 1 mm would allow a maximum particle diameter of 100 μm. All of the analysed particles are significantly smaller than 100 μm. Therefore, the chosen sample can be regarded as a representative volume.

Another correlated problem is the extraction of the powder sample from the powder batch and the transport to the experiment. The ISO standard 3954 recommends the extraction of powder particles from the batch (by means of a special device) at different heights [162]. The recommended procedure extracts an amount of powder particles that is to large to be fully scanned by CT. Therefore, any transport and vibrations would lead again to a separation of small and large powder particles. The extracted amount of powder particles can be split into representative potions by means of centrifugation. The capture of all particles in such a small representative powder batch cannot be ensured by utilising a glass capillary. The preparation of powder particles in epoxy is more appropriate since all particles can be mixed into the epoxy without any additional segregation. Such a measurement of powder extracted according to ISO 3954 standard was performed for the AISI 316L powder batch. The difference is presented in Figure 3.9d.

Two dataset are compared: in the first case, the powder was prepared in the capillary, and in the second case, the powder was prepared in the epoxy. The datasets represent the same volume (*i.e.* region of interest): 2250 × 2250 × 200 (930 MB) with a voxel size of 0.438 μm for the capillary sample and 1125 × 1125 × 100 (115 MB) with a voxel size of 0.876 μm for the epoxy sample. The voxel size is different due to the different sample size and therefore different magnification to avoid ROI-CT during the measurement. The computing time of the particle separation algorithm is 100 min and 2.25 min, respectively. The number of analysed

particles within the capillary and epoxy is 3000 and 270, respectively. While the powder arrangement in the glass capillary yields for higher particle statistics, the pre-separated particles in the epoxy resin are separated faster by algorithms.
A disadvantage of the powder sample in a capillary is that any vibration will affect the particle arrangement within the sample. It is therefore not reproducible. Once the powder particles are embedded in epoxy resin, they could also be sent to various laboratories for round robin tests.
According to the needs of the measurements and the information above, an optimised powder sample preparation could be achieved.

4 Influence of the Build Angle on the Strut Porosity and Surface Topography

The nominal geometry of a strut is a cylinder [40]. Struts are the fundament of the lattice structures. A detailed knowledge about struts is crucial for lattice structure design as well as for the understanding of their performance.
As described in chapter 2.3, the resolution of a CT-scan becomes better with decreased part size. A high resolution scan of a single strut will reveal information that would have been invisible at the scale of the whole lattice structure. Therefore, the combination of such multiscale sample measurements are advisable.
In this chapter the link between the porosity of the powder particles and the manufactured struts will be made, as well as the link between powder particle size and strut surface topography. The build angle (*i.e.* the angle between build plate and major axis of the produced structure) is of significant interest for the design of lattice structures. The aim is to be able to manufacture structures by means of L-PBF without any restriction on the build angle. Currently, the production of structures with a build angle below 30° is not feasible without support structures [66] because the part would fall apart. This chapter will therefore aim to an improved and detailed understanding of how the strut quality (in terms of porosity and surface topography) is influenced by the build angle.
An analysis strategy will be presented, allowing a detailed insight into angular resolved surface topography together with detailed porosity evaluation, since the pore shape is correlated with the position within the strut, and this correlation dependce on the build angle.

4.1 Experiment

Seven struts made of IN 625 with a build angle α ranging from 30° to 90° as shown in Figure 4.1a were produced by means of L-PBF by Siemens, Gas and Power, Berlin, Germany. α is defined as the angle between the cylinder axis and the build plate, so that $\alpha = 90°$ implies a strut perpendicular to the build plate. Each strut had a nominal diameter of 1 mm and a nominal length of 6 mm. A region of interest of 5 mm was analysed along the height of the samples. A marker, as shown in Figure 4.1b, was attached to the head of the strut. The gap in the ring indicated the up-skin (US) surface during production.

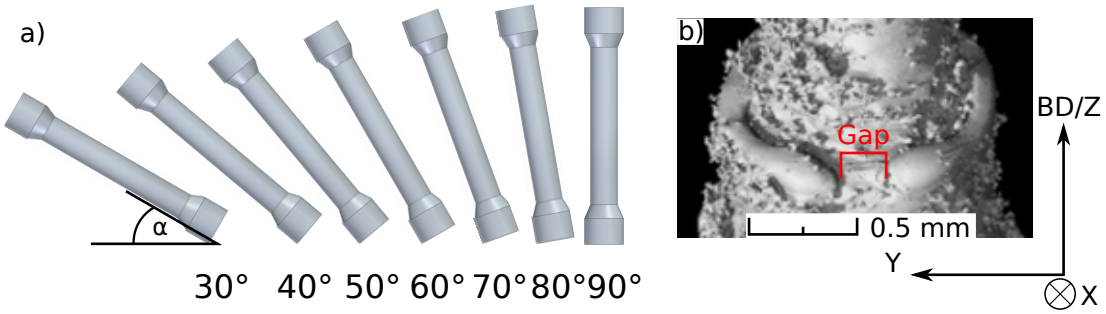

Figure 4.1: Sketch of the investigated struts with build angle α ranging from 30° to 90° (BD=build direction) and b) a 3D rendered image of the gap in the reference marker at the head of a strut to indicate the up-skin (US)

The IN 625 powder characterised in chapter 3 was used to manufacture the struts. All samples were manufactured on an EOS M290 machine with a Siemens-proprietary process parameter set, optimised for IN 625. A layer thickness of 20 μm was applied. The samples were inclined towards the re-coater [66]. The scan strategy was a bi-directional hatch pattern, rotated by 67° from layer n to layer $n+1$. Since no contour scanning was applied, only filling hatches were used.

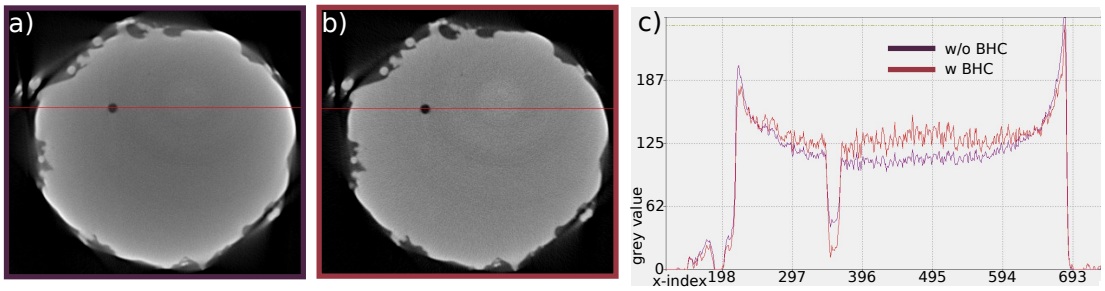

Figure 4.2: A tomogram is presented without a) and with b) applied beam hardening correction and together with the respective line profiles c)

The CT measurements were carried out on a laboratory CT scanner (GE v|tome|x 180/300L) with a transmission target operated at $U_t = 125\,\text{kV}$ and $I_t = 60\,\mu\text{A}$. An acquisition time of 2 s per projection for 2100 projections resulted in a measurement time of 70 min per scan. A physical beam filter was not applicable, due to the low beam intensity of the transmission target. However, a beam hardening correction (BHC) was applied by means of an in-house software based on look-up

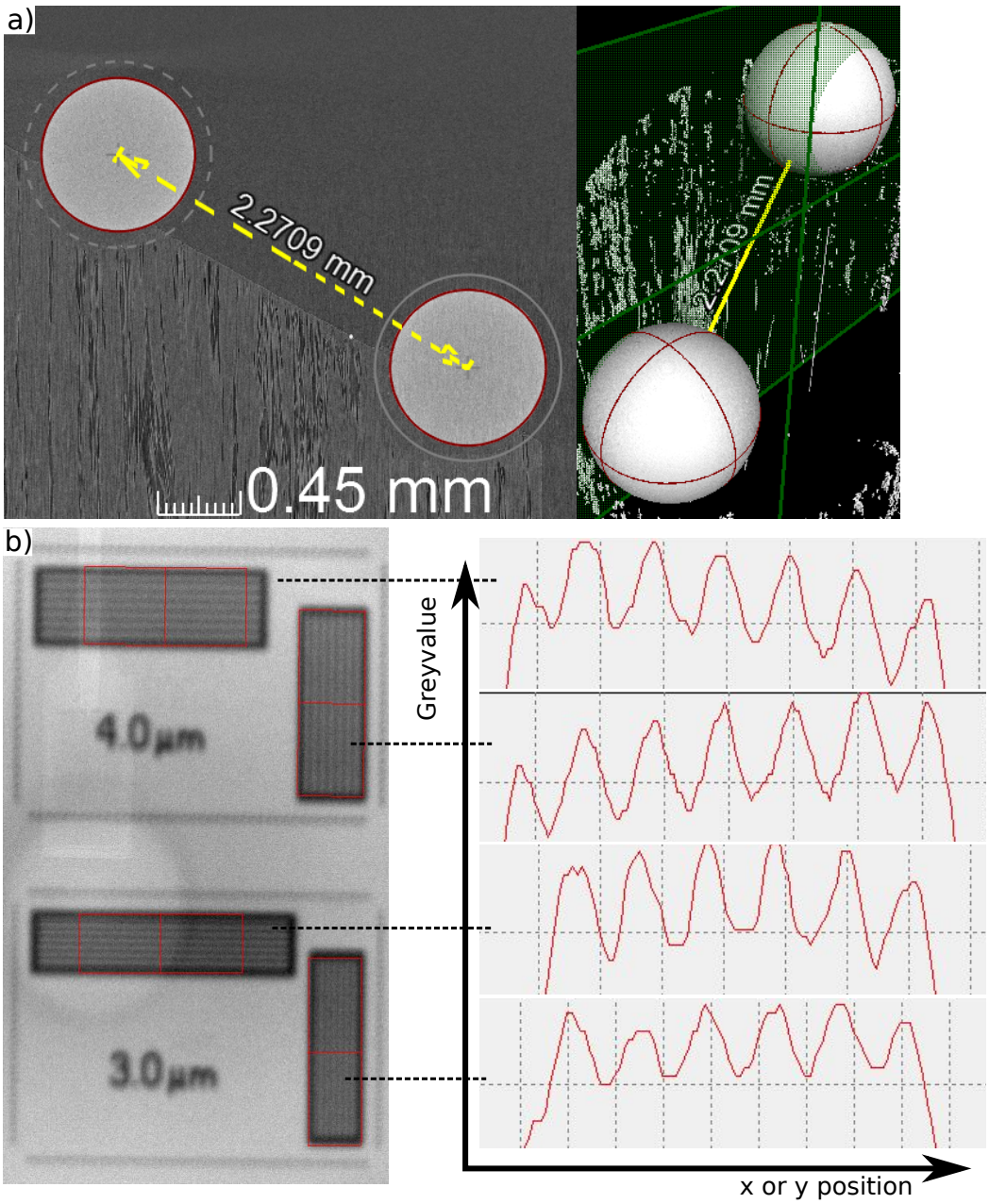

Figure 4.3: a) The result of the calibration measurement with two ruby spheres indicating the measured distance of 2.2709 mm. A tomogram is presented on the left, which is marked green in the 3D image on the right. b) The radiography on the left shows the JIMA RC-02 resolution chart for the tube parameter $U_t = 125\,\mathrm{kV}$ and $I_t = 60\,\mu\mathrm{A}$. The profile plot indicate that all seven lines are resolved for $4\,\mu$m in both horizontal and vertical direction. In the case of $3\,\mu$m line thickness, only six lines are visible.

tables, see Figure 4.2. A Feldkamp algorithm [135] was used for reconstruction. The voxel size was 2.1 μm, estimated by a calibration measurement. A pair of ruby spheres separated by a calibrated distance was measured, see Figure 4.3a. The nominal and actual sphere distances were 2.2728 mm and 2.2709 mm, respectively. This procedure is needed as the GE v|tome|x 300L is not designed as a metrology system. Therefore, the mechanical motor position is not precise enough for measurements at high magnifications ($M = 96\,\mathrm{x}$). After calibration of the voxel size, the rotation stage was kept at the same SOD for all experiments. A resolution of 4 μm for the projections was determined by means of a JIMA RC-02 resolution chart [151], see Figure 4.3b. The line profiles shown in Figure 4.3b indicate a clear separation of all seven lines for both horizontal and vertical directions for the 4 μm chart, while for the 3 μm chart only six lines were resolved.

Each strut was scanned at three different heights and each volume was reconstructed separately. Afterwards, the reconstructed volumes were merged into one volume. For the sake of a proper merge, the absorption coefficient has to be the same for all reconstructions.

The reference ring was used to align all samples to the same coordinate system: The US-DS axis was aligned with the x-axis, while DS corresponded to $+x\,(\theta = 0°)$ and US to $-x\,(\theta = 180°)$; the argon flow was aligned with the y-axis (spanning from $\theta = 90°$ to $\theta = -90°$); the height of the strut was aligned with the z-axis in the way that the strut was built in positive z-values, see Figure 4.1. The registration of the sample coordinate system onto this coordinate system was done first by the module 'simple registration' implemented in VG studio MAX 3.2 and afterwards with a least-square fit of a cylinder, see source code 1 in chapter A.4. The reconstructed struts were characterised regarding porosity and surface topography.

4.2 Porosity

The detection and characterisation of pores within the material was performed by the VGdefX-algorithm implemented in VG studio MAX 3.2 [165]. The detected pores were filtered according to their volume. In general, a pore size filter of 27 voxels is recommended [166]. That represents a lateral side of 3 voxels. However, a conservative pore size filter of 64 voxel was applied to avoid false positive pore

detection.

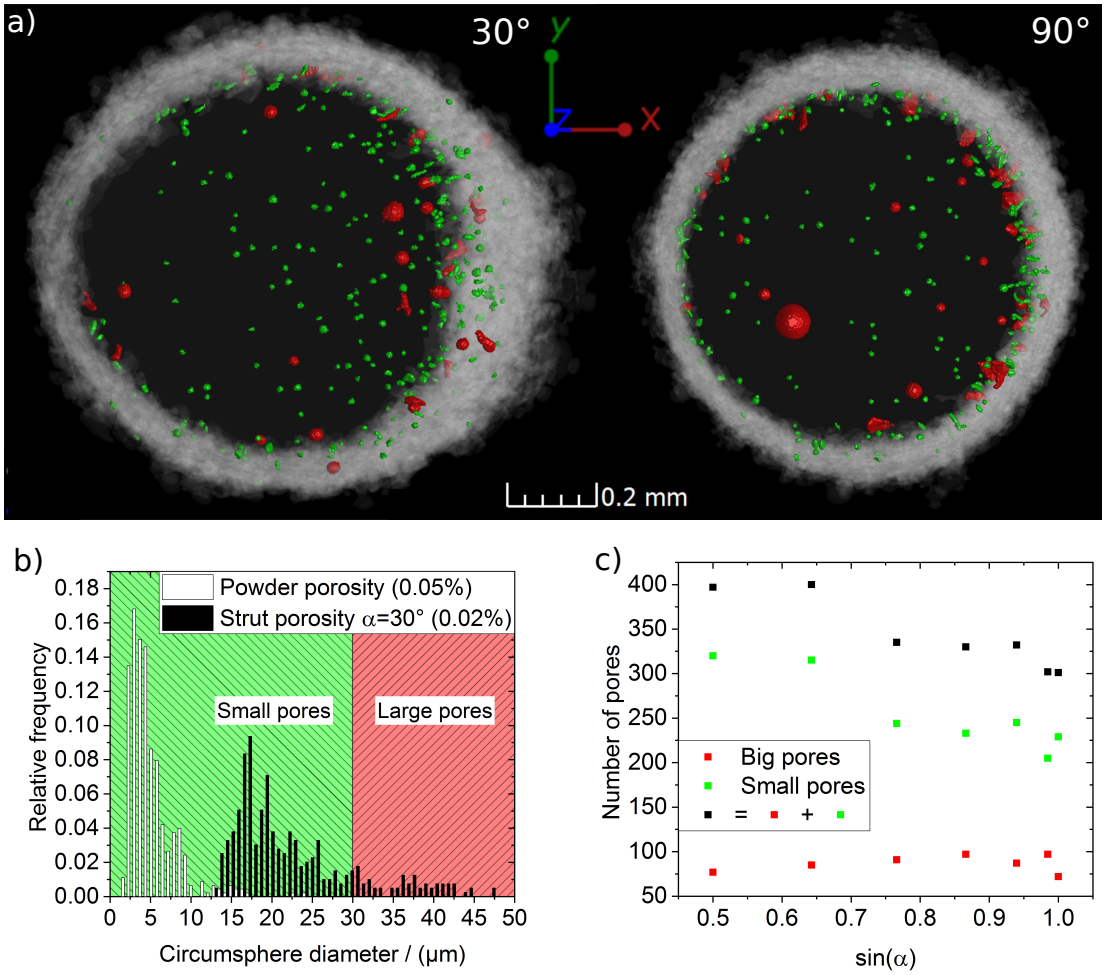

Figure 4.4: a) Projection of porosity and surface along the height of the strut with (left) $\alpha = 30°$ and (right) $\alpha = 90°$. The material is presented as transparent to 90 %. The pores are color-coded according to the two categories: small (green) and large (red), as defined in Figure 4.4b. b) The pore size distribution for the powder sample (white) and for one strut ($\alpha = 30°$, black), categorised into small pores ($d_{CS} \leq 30\,\mu$m, green) and large pores ($d_{CS} > 30\,\mu$m, red). c) Absolute number of small and large pores in dependence of $\sin(\alpha)$ and partitioned according to Figure 4.4b.

The 3D porosity is projected onto a plane in Figure 4.4a for the 30°-strut and the 90°-strut. The material is shown as transparent to 90 % to help visualising pores as well as the outer surface of the struts, which appear as a grey cloud. In Figure 4.4a, the DS is on the right side of the 30°-strut. The porosity distribution shows

a gradient with an increased number of pores near the down-skin. This gradient does not appear for the 90°-strut, since this strut was built perpendicular to the build plate. The porosity is 0.02 % and 0.03 % for the 30°-strut and the 90°-strut, respectively.

The pore size distribution in terms of the circumsphere diameter d_{SC} is shown in Figure 4.4b for $\alpha = 30°$. d_{SC} is chosen to be conservative in particle size as explained in chapter 3.2. The maximum diameter was found to be around 50 μm. According to this distribution, the pores are divided into small ($\leq 30\,\mu$m) and large pores ($> 30\,\mu$m), color-coded in green and red, respectively. The results for all struts are summarised in Figure 4.4c. Both the total number of pores and the number of small and large pores are presented as a function of $\sin\alpha$. The decrease of the total number of pores can be understood as a reduction of only the number of small pores. The number of large pores remains constant with $\sin\alpha$. Therefore, an upright sample orientation ($\alpha = 90°$) promotes the suppression of pores with a size $\leq 30\,\mu$m.

The spatial distribution of the porosity is evaluated as the next step. The pores are homogeneously distributed along both the strut height and the build height (= strut height $\times \sin\alpha$). In addition, the size and shape of the pores does not depend on the height, see Figure A.2. However, it is clear that pores accumulate near the surface (Figure 4.4a). For quantification, the anisotropy of each pore (defined by equation 3.3) is plotted as a function of distance to the sample surface, *i.e.* the shortest distance in 3D between pore surface and sample surface (Figure 4.5). Each point in Figure 4.5 corresponds to one pore. The point cloud shows three different regions. Region I proves a strong likelihood for pore appearance within 90 μm from the surface. This effect is known [44] and explained by excessive energy input due to deceleration and acceleration of the laser at the turning points, as well as to heat accumulation due to the surrounding powder bed [44]. An absence of elongated pores is observed in region II (large distance to sample surface and large A). This indicates a preferential appearance of elongated pores ($A \geq 0.8$) within $\leq 90\,\mu$m to the surface. Nearly every pore with a distance to the strut surface larger than 90 μm showed an anisotropy value lower than 0.8 (region III).

This can be qualitatively explained by a more isotropic heat distribution within the bulk compared to the surface. Assuming a soft material at manufacturing temperature, the pore would align with the temperature gradient. Furthermore,

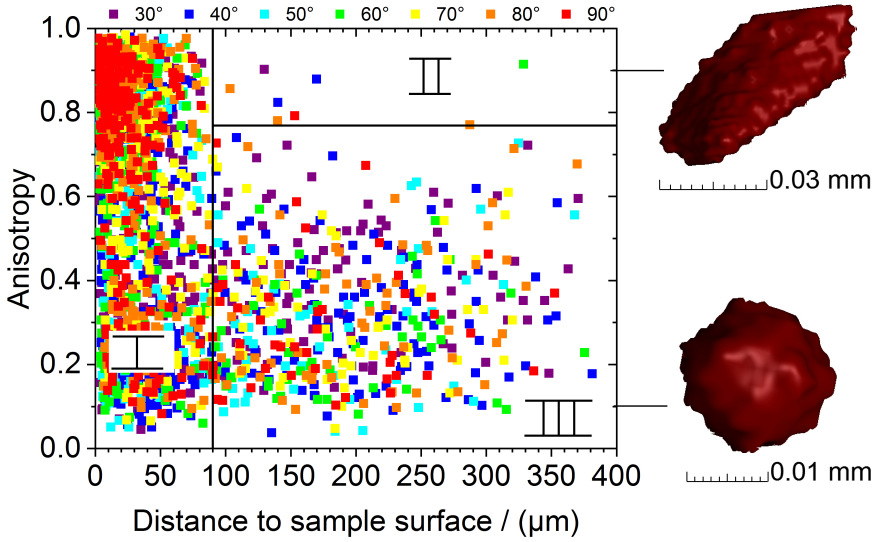

Figure 4.5: The anisotropy of each pore plotted as a function of the pore distance to the sample surface, color-coded according to α, see legend above the graph. The diagram was split into three regions of interest (I, II and III), each characterised by a different pore shape. The 3D-rendered pores on the right side visualise the difference in anisotropy.

it is reasonable that near the surface the material can freely deform in the radial direction, creating thereby elongated pores, while in the bulk the hydrostatic stress induces round-shaped defect. A total porosity of $0.02 - 0.03\,\%$ gives evidence that the process parameters are optimised and therefore that lack of fusion porosity is unlikely, *i.e.* the energy density is sufficient not to get lack of fusion pores [42].

4.3 Surface Topography

The projection along the strut height (Figure 4.4) indicates also a difference in the surface topography of the two struts. For $\alpha = 30°$ the projection shows a broader grey cloud. This can be understood as a higher amount of attached powder particles, especially at the DS (positive x-axis). Even though the 90°-strut was build perpendicular to the build plate, the porosity and surface topography is not isotropic (see Figure 4.4a, right). This observations denotes an effect of the part position on the build plate (this is discussed in chapter 4.4).
To gain more information about the surface topography, a workflow was created (Figure 4.6) as a combination between the advanced surface determined by VG

studio MAX 3.2 and a self-written Python script (see appendix A.4, for the source code 1). This script used the advanced surface determination from VG studio MAX 3.2, see Figure 4.7a. The rendered strut surface was presented in 3D in Figure 4.7b for $\alpha = 30°$. The resolution was sufficient to correlate the laser hatches with the build angle. In this case ($\alpha = 30°$) the laser tracks appear with an angle of 60°. The determined surface was meshed and exported in both formats: point cloud (ASCII) and surface-mesh (stl). The point cloud data was smaller, easier to handle, and led to shorter calculation times. The trade-off was the loss of the surface orientation as defined by the surface normal vector. The latter was instead provided within a stl-file.

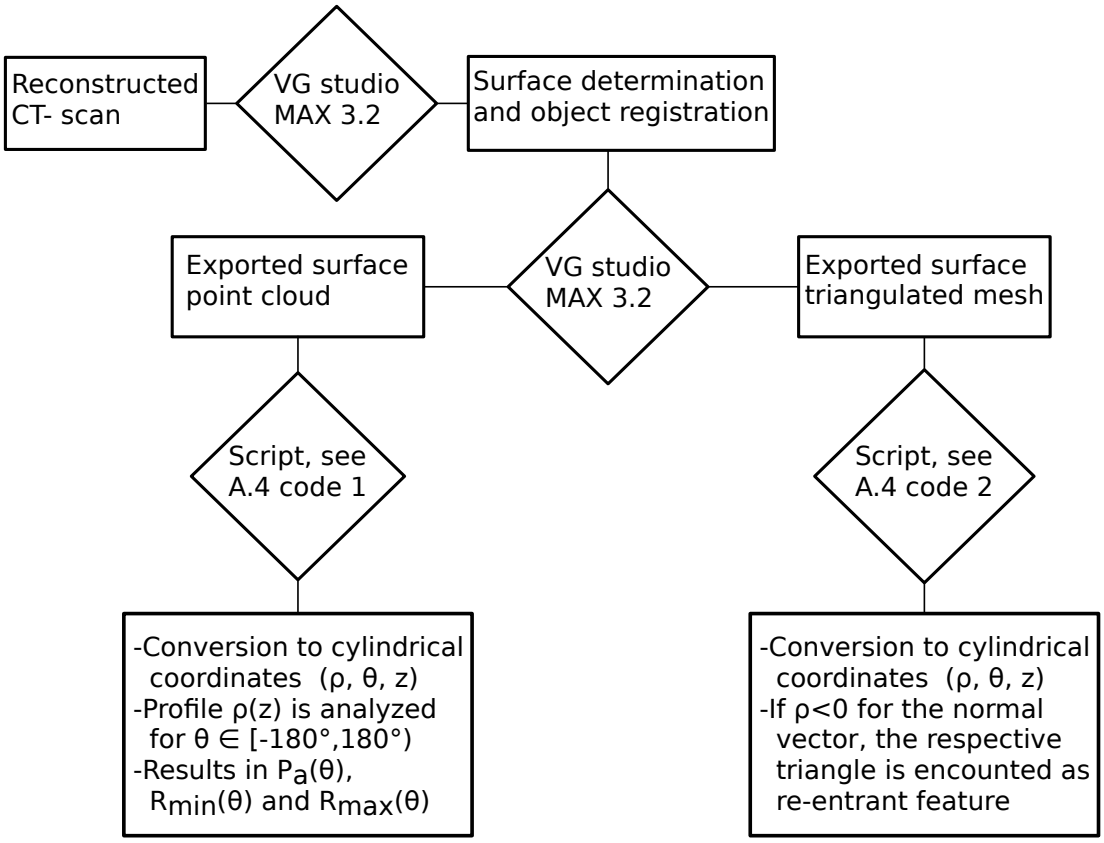

Figure 4.6: The schematic workflow for the surface topography characterisation.

The next step for surface topography analysis was the conversion of the Cartesian strut surface (x, y, z) to cylindrical coordinates (ρ, θ, z), see Figure 4.7c. As indicated in Figure 4.7c, primary line profiles $\rho^{\theta}(z)$ were extracted from the surface along the strut height for every azimuth angle θ. 'Primary' means that no high- or low-pass filter was applied to the line profiles, as recommended to distinguish the

surface waviness and surface roughness according to ISO-standard [167]. These line profiles $\rho^{\theta}(z)$ were analysed calculating the arithmetic mean $P_a(\theta)$, the maximum value ρ^{θ}_{max}, and the minimum value ρ^{θ}_{min} according to equation 4.1 and 4.2.

$$P_a = \frac{1}{N}\sum_{i=1}^{N}\left|\rho_i^{\theta}(z) - \rho^{\theta}_{mean}\right| \tag{4.1}$$

with

$$\rho^{\theta}_{mean} = \frac{1}{N}\sum_{i=1}^{N}\rho_i^{\theta}(z)$$

$$\rho^{\theta}_{max} = \max_i \rho_i^{\theta}(z) \qquad \rho^{\theta}_{min} = \min_i \rho_i^{\theta}(z) \tag{4.2}$$

The analysis was tested for two data sets that had a different point cloud resolution, *i.e.* the surface is sampled with a higher ('precise') and with a lower ('fast') number of points. The line profiles were plotted for $\alpha = 30°$, $\theta = 0°$ and $\alpha = 30°$, $\theta = 180°$ in Figure 4.7d. The difference between 'fast' and 'precise' line profiles becomes prominent for surface sections of low curvature. Even the 'fast' point cloud shows a sufficient sampling rate for surface regions of high curvature. Therefore, both point clouds result in similar P_a values, see Figure 4.7e. It is remarkable that P_a is slightly smaller in the case of the 'precise' point cloud compared to the 'fast' one for most θ. In fact, the 'fast' profile was expected to smoothen the surface, which would have led to lower P_a values.
The evaluation of ρ^{θ}_{max} and ρ^{θ}_{min} is shown in Figure 4.7f. ρ^{θ}_{min} encloses an area corresponding to the amount of solid material in the centre of the strut. The dark-grey area in Figure 4.7f can be understood as the base of a prism representing the solid core of the strut throughout the full height. If the projection through the height of the strut contains at least one voxel of air, it is assigned to the light-grey area restricted by ρ^{θ}_{max}. The internal porosity is neglected for this analysis.
Evaluating the shape of the inner area (dark-grey) in Figure 4.7f, a flat side is noticed at the DS and a round shape at the US. This indicates more material at $\theta = 180°$. This observation indicates an improved material solidification at the US compared to the DS. However, in Figure 4.8b, the size of the dark-grey area is found to be independent of the build angle. The size of the light-grey area shows a decrease by 17 % relative to the nominal area. The increasing volume of the low-density annular region is an indication of an increased number of attached

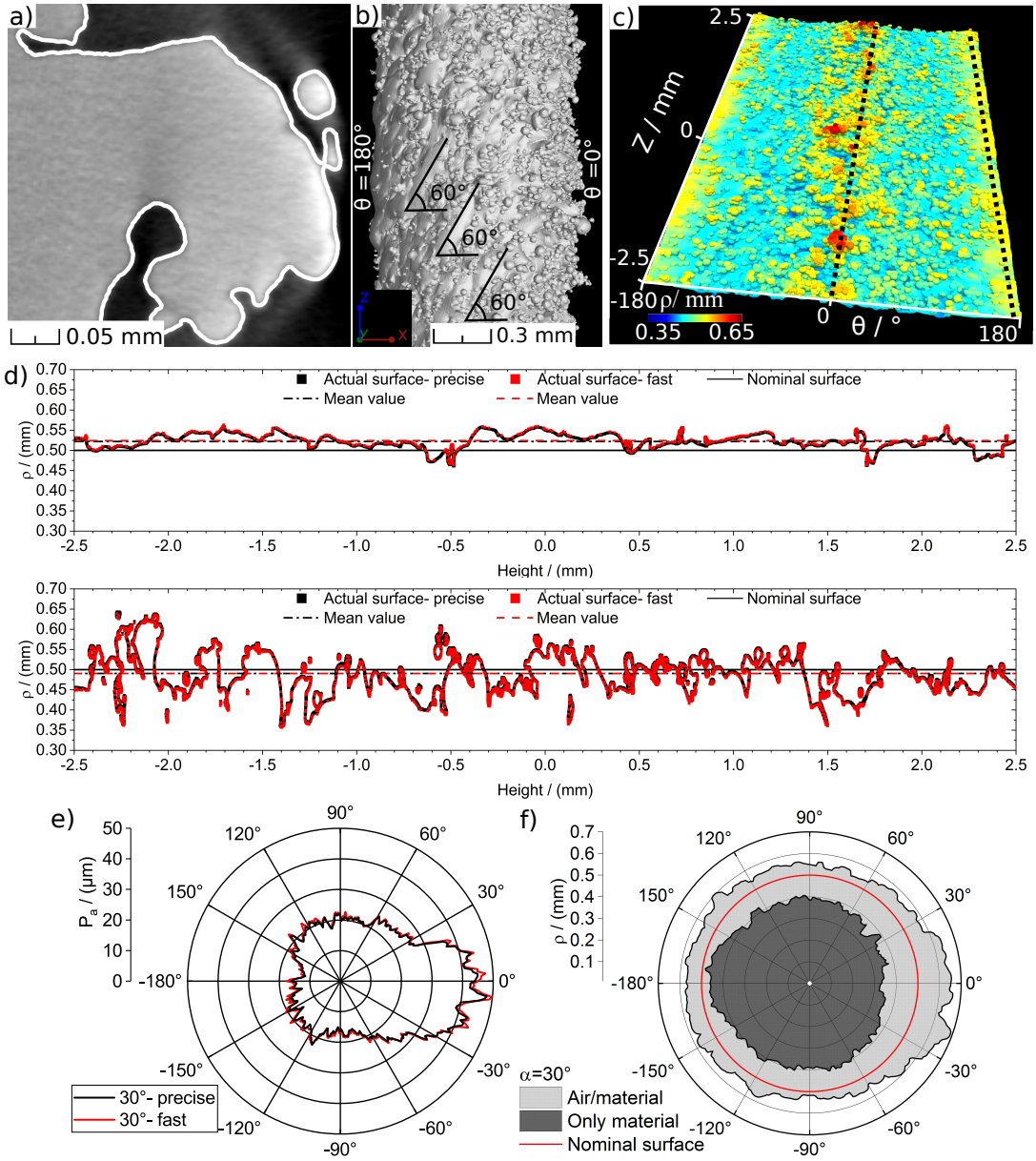

Figure 4.7: a) Example of the determined surface applying the advanced surface determination by VG studio MAX 3.2. b) Side view of the rendered surface of the strut with $\alpha = 30°$, aligned upright. The down skin (DS) (right, $\theta = 0°$), the US (left, $\theta = 180°$), and the laser tracks of the individual layers are clearly visible. c) The unrolled rendered surface presented in polar coordinates. The two dotted black lines indicate the position of the two exemplary line profiles shown in d). d) The up-skin (top) and the down-skin (bottom) line profiles are extracted for a different point cloud resolution. e) The results of the surface analysis according to equation 4.1 for $\alpha = 30°$. f) The polar plot of ρ_{min} and ρ_{max} according to equation 4.2 indicates to different areas. The dark grey area represents the area of solid material through-out the full strut height, where the light grey area indicates the region of attached powder particles and notches.

powder particles, potentially along with the increased surface roughness at the DS.

The analysis workflow is explained for one strut ($\alpha = 30°$) in Figure 4.7. The results of the workflow for all seven struts are presented in Figure 4.8.

While the P_a value remains similar for the US, P_a values in the DS region increases with decreasing α (increased tilt to the vertical direction). The high P_a values (up to 50 μm for the DS of the strut with $\alpha = 30°$) extend over an azimuthal range of $\theta \approx 90°$. This means that a quarter of the surface holds an increased number of powder particles.

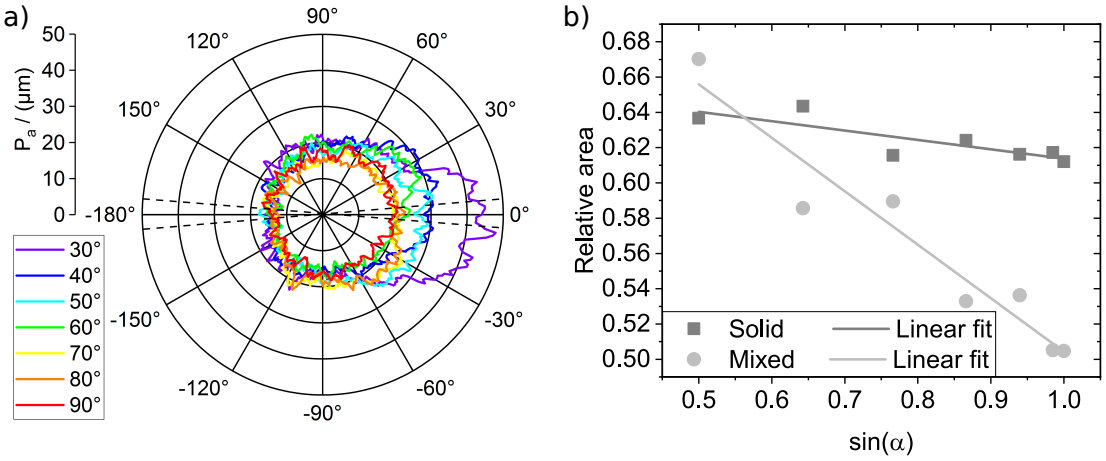

Figure 4.8: a) The results of the surface analysis according to equation 4.1 for the seven struts. b) The evaluation of the dark-grey and light-grey area in Figure 4.7f for the seven struts.

For each strut, $P_a(\theta)$ is averaged over two intervals $-5° \leq \theta \leq 5°$ (DS) and $175° \leq \theta \leq 185°$ (US), see dotted lines in Figure 4.8a. These mean values are plotted in dependence of $\sin(\alpha)$ in Figure 4.9a. The standard deviation is taken as the error for P_a. The stair-case effect induces a known amount of roughness for the DS and the US. Such effect was therefore subtracted from our data, see hollow triangles in Figure 4.9a. While the roughness at the DS decreased by 50 % from the strut with $\alpha = 30°$ to the strut with $\alpha = 90°$, the roughness at the US slightly increased, indicating a smaller number of attached powder particles for $\alpha = 30°$. The lowest P_a values correspond to the most horizontal surface: the US of the strut with $\alpha = 30°$. The total change of roughness at the DS corresponds to the mean powder particle size ($d_{50} = 17\,\mu$m). It could be argued that tailoring the particle size would enable to tune the surface topography.

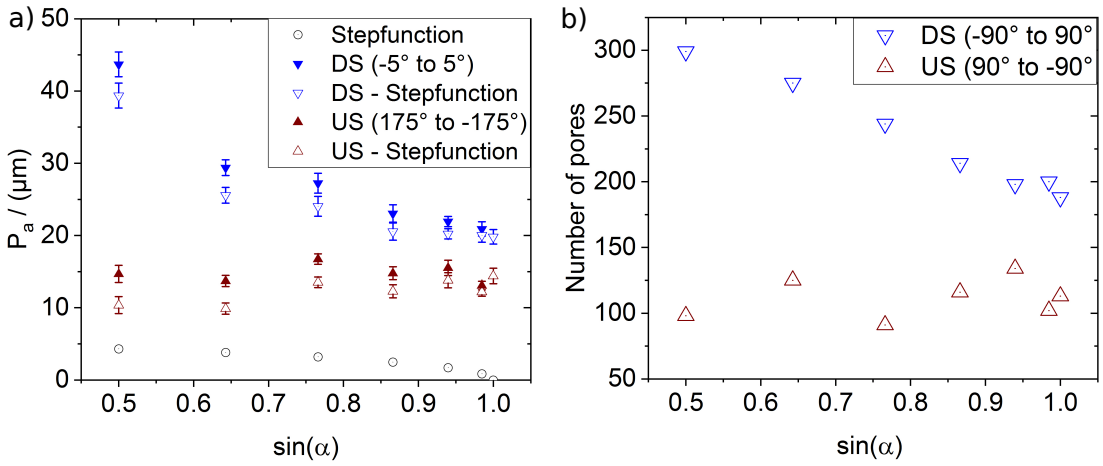

Figure 4.9: Dependence of a) the roughness P_a and b) of the number of pores for the US (red) and the DS (blue) on the $\sin\alpha$.

The mesh of the determined strut surface is exported as .stl file by VG studio MAX 3.2. After transformation from Cartesian to cylindrical coordinate system, the surface area was evaluated regarding the normal vector of the mesh triangles. A triangle is assigned to a re-entrant feature, if the normal vector has a negative component in ρ-direction ($\hat{\rho} < 0$) as sketched in 4.10a, see the source code 2 in chapter A.4. This algorithm does not only consider re-entrant features but also corrects for a inhomogeneous mesh size, as each triangle is weighted by the area associated to it. For a fine-meshed region (*i.e.* where the curvature radius is large), many triangles with smaller area are counted compared to a coursed-mesh region (*i.e.* where the curvature radius is small) where few triangles with a larger area are counted. Comparable to the first analysis described in the previous paragraph, the profile functions are analysed line-wise as a function of θ. θ varies from 0° to 360° with a step-width of 1°. The area of the triangles with a negative $\hat{\rho}$ is summed up for each line profile ($A^{\theta}_{\hat{\rho}<0}$) and related to both the total area of the respective line-profile ($\frac{A^{\theta}_{\hat{\rho}<0}}{A^{\theta}}$, Figure 4.10b) and to the total strut area ($\frac{A^{\theta}_{\hat{\rho}<0}}{A^{\alpha}}$, Figure 4.10c).

In general both diagrams are in agreement with Figure 4.8a: they show higher values for the DS than for the US, the largest values for the 30°-strut, similar values for all struts at the US, and symmetry for each strut (*i.e.* same values for $\theta = -90°$ and $\theta = 90°$). However, characteristic differences lead to new information about the surface topography:

A difference between $\frac{A^{\theta}_{\hat{\rho}<0}}{A^{\theta}}$ and $\frac{A^{\theta}_{\hat{\rho}<0}}{A^{\alpha}}$ is the distribution over θ. While $\frac{A^{\theta}_{\hat{\rho}<0}}{A^{\alpha}}$ is com-

parable to P_a of Figure 4.8a, showing clearly the highest value for each strut at the DS, $\frac{A^{\theta}_{\hat{\rho}<0}}{A^{\theta}}$ is roughly constant for each strut over the full range from $\theta = -90°$ to $\theta = 90°$.

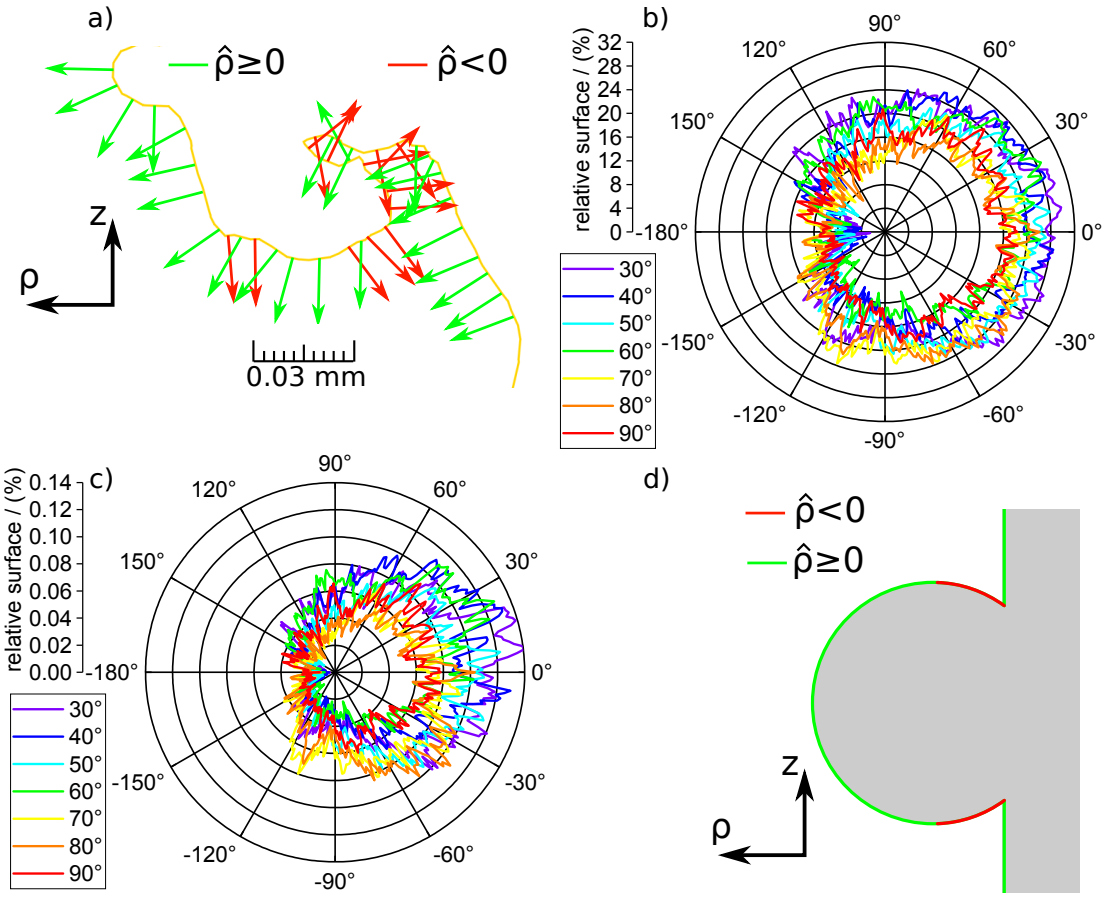

Figure 4.10: a) A sketch of the principal behind the estimation of the relative surface having a negative $\hat{\rho}$. Since the sketch is made for a real meshed strut surface, the sketch is in scale. b) The ratio between the area of the vertices with negative $\hat{\rho}$ and the area of all vertices along one line profile is shown in a polar plot for each strut ($\frac{A^{\theta}_{\hat{\rho}<0}}{A^{\theta}}$). c) The ratio between the area of the vertices with negative $\hat{\rho}$ and the area of all vertices of the strut surface is shown in a polar plot for each strut ($\frac{A^{\theta}_{\hat{\rho}<0}}{A^{\alpha}}$). d) A sketch of the effect of an attached powder particle on the relative negative surface.

The ratio between the amplitude of $\alpha = 30\,°$ and the amplitude of $\alpha = 90\,°$ at $\theta = 0\,°$ is only about 1.4 in Figure 4.10b, whereas the same ratio is about 2 in both Figures 4.10c and 4.8a.

Another difference is prominent at $\theta = 180\,°$. While Figure 4.8a proves no de-

pendence of P_a on α at US ($\theta = 180\,^\circ$), Figure 4.10b shows a significant decrease from $\alpha = 90\,^\circ$ to $\alpha = 30\,^\circ$. This decrease appears less prominent in Figure 4.10c.

The pores characterised in the previous section 4.2 were analysed together with the surface topography for the DS and the US, see Figure 4.9b. Due to the small number of pores, the azimuthal angular range was increased to 180° (instead of 10° as used for the analysis of the surface topography). This means that all pores in the interval $-90° \leq \theta \leq 90°$ were assigned to the DS and all pores in the interval $90° \leq \theta \leq 270°$ were assigned to the US.
For all struts, more pores are present in the DS region compared to the US, see Figure 4.9b. The origin of this difference can be found in the process itself: Firstly, the molten material in the DS region is likely to sag, as there is no solid material below. Secondly, heat accumulates in the DS region, as the amount of surrounding powder, acting as thermal insulator, is larger at the DS than at the US. The difference between the number of pores at the US and the DS becomes smaller with increasing build angles, as shown in Figure 4.9b. This is a strong indication that pores are not only formed from the melt pool adjacent to the solid material, otherwise a larger number of pores would appear in the US region (always facing solid material). This has been confirmed by *in-situ* radiography observations in the literature [44].
Another approach for the evaluation of the surface topography is the dimensionless surface area to volume ratio $\frac{A_\alpha}{V_\alpha^{2/3}}$. For a perfect cylinder with diameter $d = 1\,\mathrm{mm}$ and height $h = 5\,\mathrm{mm}$, it would be

$$\frac{A_{cylinder}}{V_{cylinder}^{\frac{2}{3}}} = \frac{\pi d \cdot h + 2\pi \left(\frac{d}{2}\right)^2}{\left(\pi \left(\frac{d}{2}\right)^2 \cdot h\right)^{\frac{2}{3}}} = 6.94 \tag{4.3}$$

The $\frac{A_\alpha}{V_\alpha^{2/3}}$-values in Figure 4.11a are nearly twice as high as the theoretical value (equation 4.3) ranging from 12 for $\alpha = 90°$ to about 14 for $\alpha = 30°$. This again indicates an increase of surface roughness towards smaller build angles. The 30°-strut represents the only exception to a linear behaviour. To explain this behaviour, the relative surface area $\frac{A_\alpha}{A_{cylinder}}$ and the relative volume $\frac{V_\alpha}{V_{cylinder}}$ are plot in Figure 4.11b. As expected both the relative area and the relative volume increases with a lower build angle due to a larger number of attached particles. Such increase corresponds to the linear increase in Figure 4.11a. However, for

the 30°-strut the relative volume shows a drop, while the relative surface area increases. The material starts to drip into the powder bed, as we will see in more detail in the next chapter.

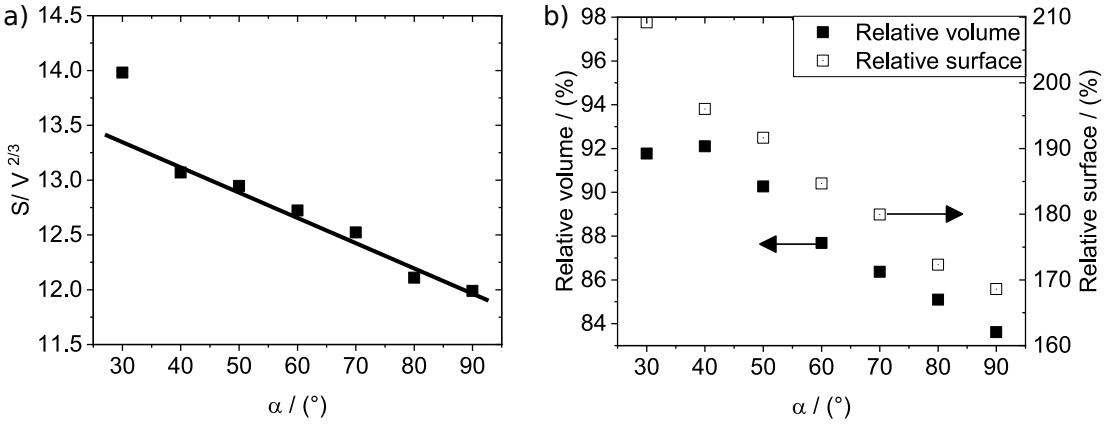

Figure 4.11: a) The dependence of the dimensionless surface-to-volume ratio on the build angle and b) the dependence of the relative volume (left scale) and the relative surface (right scale) on the build angle

4.4 Discussion

In general, it is proven that the struts with lower α have a larger projected area than the struts with larger α, even though the solid centre remains constant with α. The sum of the two relative areas in Figure 4.8b is always larger than 100 %. This is because the light-grey area is always overestimated. In fact, one pixel is added to the light-grey area as soon as just one voxel of material projects onto it. The centre of mass of a single cross-section does not lie on the same vertical axis. This artificially enlarges the total projection area. This artefact does not occur while working with volumes or with single cross-sections. We can therefore, take that the projection method is the most 'conservative' to separate the solid material from the attached powder particles.

For the strut with $\alpha = 90°$, the mean roughness parameter P_a was expected to be the same for every direction (*i.e.* independent of θ in Figure 4.8a, $P_a(\theta) = \text{const.}$). Even though the alignment of the US for the strut with $\alpha = 90°$ was random, a significant difference of P_a between $\theta = 180°$ and $\theta = 0°$ is observed. The argon flow cannot be the cause of this difference, as the argon flow was oriented along the perpendicular direction ($\theta = 90°$ to $\theta = -90°$) and would therefore be visible

for every curve in Figure 4.8a. The influence of the re-coater and the effect of the strut position on the build plate need to be considered. All other struts were manufactured with their tilt along the re-coater travel direction. The strut with $\alpha = 90°$ was located in the very bottom right corner of the build plate. Hence, the laser beam approximately penetrated with an angle of $12°$ $\left(= \arctan\left(\frac{\sqrt{2}\cdot 145\,\mathrm{mm}}{475\,\mathrm{mm}}\right)\right)$ into the powder bed. While the focal plane of the laser is corrected by the L-PBF machine at each tilt, this tilted penetration of the laser beam into the powder bed causes a distortion of the energy spatial distribution profile. Such distribution causes the observed asymmetry of P_a between $\theta = 0°$ and $\theta = 180°$. Such dependence of the surface topography on the position on the build plate is in agreement with Kleszczynski *et al.* [68]

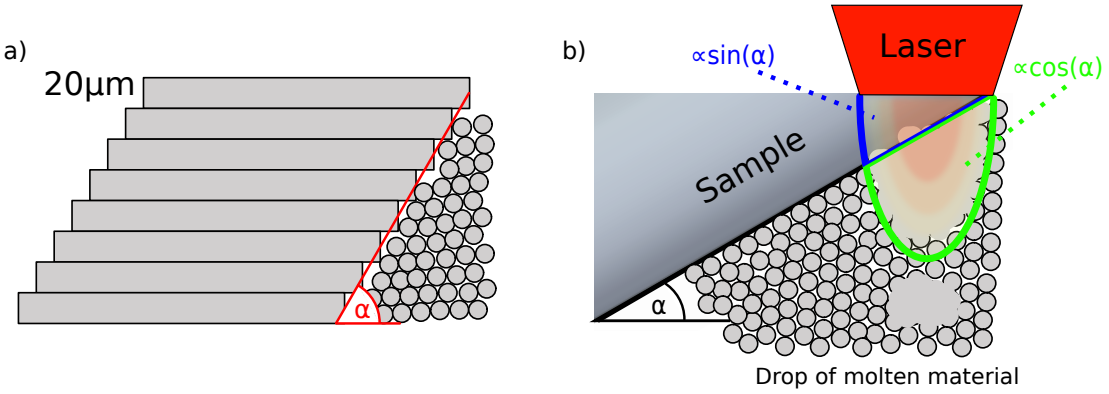

Figure 4.12: a) A sketch of the stair-case effect for tilted structures and b) a sketch of the manufacturing process of a tilted strut. The energy spatial distribution profile is presented split into the part affecting the strut only (blue, $\propto \sin\alpha$) and the part affecting the powder bed only (green, $\propto \cos\alpha$). The illustration of the molten material dripping off the edge for a low build angle is also added.

The amount of energy penetrating into the strut is proportional to $\sin\alpha$, as sketched in Figure 4.12b. This is why, the roughness and the number of pores are plotted as a function on $\sin\alpha$. Note, that the laser beam penetrates roughly $100\,\mu$m under the focal plane.

The hypothesis that the direction of the laser beam only influences the DS is confirmed by the linear dependence of both the number of pores and P_a on α at the DS (see Figure 4.9). The deviation of P_a *vs* $\sin\alpha$ from a linear relation for $\alpha = 30°$ is in agreement with the evaluation of the surface-to-volume ratio for the struts.

A linear dependence as a function of the build angle is found for both the surface roughness and the surface-to-volume ratio of the struts. However, the sample built at the smallest built angle ($\alpha = 30°$) deviates from this trend. This could be explained by assuming that the molten material drips into the powder bed. In fact, the surface cohesion force becomes smaller than gravity, and the viscosity is low at high temperatures. This leads to an anomalous increase of surface roughness and decrease of part volume.

The point-cloud-based calculation has the weakness that the mean value slightly biases the distribution of points sampling the surface. Regions of high curvature are more frequently sampled. Each data point accounts for the same size of surface. High curvature radii (*i.e.* high sampling rates), leads therefore to an overestimation of the surface area, while small curvatures radii (*i.e.* low sampling rates) leads to an underestimation of the surface area. The observation that P_a is larger for the 'fast' point cloud compared to the 'precise' one can be justified by the different surface sampling. On average, the distance between the mean value ρ^{θ}_{mean} and the individual values $\rho^{\theta}_{i}(z)$ will increase if the points close to the average value ρ^{θ}_{mean} are reduced. As soon as the sampling is so low that certain surface irregularities are lost, P_a would be reduced. In that case the lower sampling would lead to an artificial surface smoothening. An inhomogeneous sampling point distribution may bias the average value P_a.
A second weakness of the algorithm is the negligence of surface re-entrant features. Such features are accessible only by CT.

Both weaknesses are captured by using the meshed surface instead of the point-cloud.
$\frac{A^{\theta}_{\hat{\rho}<0}}{A^{\theta}}$ appears as a good measurement for the amount of re-entrant features. The influence of attached powder particles can be almost neglected as they lead only to a small amount of additional relative negative surface. Each powder particles increases $A^{\theta}_{\hat{\rho}<0}$ but also A^{θ}. The case of an attached powder particle is sketched in Figure 4.10d.
The relative surface per line profile (Figure 4.10b) shows a decrease from $\alpha = 90°$ to $\alpha = 30°$ for $\theta = 180°$. This indicates less relative negative surface at the US of the 30 °-strut. That means almost no attached powder particles and re-entrant features are found at the US of the 30°-strut and corresponds therefore to the

highest surface quality.
Such a decrease from $\alpha = 90°$ to $\alpha = 30°$ for $\theta = 180°$ is not observed for P_a (see Figure 4.8a). Therefore, the analysis of the re-entrant features differentiates between attached powder particles and the fully molten powder particles. Attached powder particles induce more roughness (*i.e.* surface profile with high frequency) and re-entrant features. Fully molten powder particles induces more waviness (*i.e.* surface profile with low frequency) and no re-entrant features.
A draw back of the current calculation is that the criteria $\hat{\rho} < 0$ is not strong enough to capture re-entrant features perfectly. Some surface regions outside of the re-entrant feature are encountered as re-entrant feature and vice a versa. Figure 4.10a visualizes this problem. All surface normals outside of the entry should be green and all inside should be red. However, they are a slightly mixed since the direction of the neighbour triangles is not considered yet.

The application of the workflow was also verified for the inner surface of a ceramic based nuclear magnetic resonance (NMR) flow cell. The details are presented in the Appendix A.3 and in the publication by Bornemann *et al.* [168].

5 Structural Integrity of Lattice Structures

Building on the findings of the previous chapters, an investigation of lattice structures was carried out. Four struts joint in the middle of the cell make up the BCC unit cell. In this way each strut is the room diagonal of the unit cell. The unit cell can be assembled in any direction to form lattice structures of the format $X \times Y \times Z$.
In this chapter, single unit cells, $3 \times 3 \times 3$ lattice structures, and $7 \times 7 \times 7$ lattice structures will be discussed. The edge length of the mentioned lattices varies from 6 mm to 40 cm. As mentioned in chapter 2.3, the resolution of a CT-scan is inherently linked with the size of the object to be imaged. Therefore, the observable features and defects very from microscopic (*e.g.* pores, cracks) to macroscopic (*e.g.* distortions, deviations from CAD-files). Importantly, as the sample size increases from struts to lattice structures, the residual stresses (RS) become more relevant, due to the amount of material allowing higher RS concentrations. In this context three aspects will be presented hereafter.
Firstly, a mechanical evaluation of a $3 \times 3 \times 3$ lattice structure will be presented in terms of *in-situ* CT. CT is performed during compression of the lattice structure. Secondly, the $7 \times 7 \times 7$ lattice will be characterised regarding deviations from the CAD-file. Different registration strategies will be discussed, since they are the bottleneck of the nominal-actual comparison (NAC).
Thirdly, neutron diffraction will be presented as a tool of non-destructive RS-analysis. The combination of thin-walled structures in a complex and large lattice geometry is a challenge for ND. A unit cell (UC) will be studied to understand the principal stress directions. The knowledge of the UC will be used for the understanding of larger lattices such as $3 \times 3 \times 3$.

The UC, the $3 \times 3 \times 3$ lattice structure and the $7 \times 7 \times 7$ lattice structure were produced with the same L-PBF parameters as the struts: an EOS 290 machine was employed using the same EOS IN 625 powder analysed in chapter 3. The set of parameter was optimised by Siemens AG, Gas and Power, Berlin, for IN 625 without contour scan and $d_{layer} = 20\,\mu$m. Each lattice structure was produced with two 1 mm thick plates at each of the opposite faces of the cube. They allowed the application of an homogeneous force during compression tests. The lattice was orientated in such a way that the plates were build perpendicular to

the build plate ($\alpha = 90°$).
The UC had a nominal strut length of 10 mm and a nominal diameter of 1 mm. With a room diagonal of 10 mm, the lattice structure had an edge length a of 5.77 mm. The effective density of the lattice structure was 33 % ($= \frac{V_{UC}}{a^3}$).

5.1 Deformation under Load

5.1.1 Experiment

The *in-situ* CT experiment on the $3 \times 3 \times 3$ lattice structure was carried out at the GE v|tome|x 300L. The reflection target was operated at $U_t = 230\,\mathrm{kV}$ and $I_t = 87\,\mu\mathrm{A}$. The detector was illuminated for 1 s and 1600 projections were recorded. A 0.25 mm copper filter was used. A voxel size of 20 μm was obtained by a magnification of $M = 10\,\mathrm{x}$. These settings led to a time step of 30 min between the start of two successive CTs. A Feldkamp algorithm [135] was used for reconstruction. The uncertainty of the motor movement was well below the resolution of this CT-setup. Therefore, a calibration measurement with the ruby spheres was not necessary.
The *in-situ* load stage CT5000RT from Deben was mounted on the rotation stage. The load stage operates at room temperature and has a maximum force of 5 kN in both compression and tension. The outer dimensions of the load stage limited the magnification for this experiment. Since the jaw movement was limited to 10 mm with a maximum jaw distance of 50 mm, steel compression platens were put below and above the $3 \times 3 \times 3$ lattice structure, see Figure 5.1. The total height added up to 47 mm. Without them, the strong absorption of the jaw would introduce a cone beam artefact which would not allow an evaluation of the lattice structure close to the jaws.
A sister sample was compressed *ex-situ* to define the relevant points for *in-situ* CT-scans. The *in-situ* force-displacement diagram is presented in Figure 5.2a. The first scan was performed as a reference at 10 N applied force (necessary to hold the sample between the jaws). Three CT-scans were performed in the elastic region (at 1 kN, 2 kN and 3 kN). Beyond the start of plastification, the force interval was reduced to 0.5 kN between two CT-scans until, the maximum force of 5 kN was reached. A final scan at 10 N was also performed, so that nine scans were performed in total, see Figure 5.2a.
The load stage was operated in load control mode between the CT-scans and in

displacement control mode during the CT-scans. The speed of the lower jaw was $0.1\,^{\mathrm{mm}}/_{\mathrm{min}}$ and the displacement sampling rate was $200\,^{\mathrm{points}}/_{\mathrm{min}}$.

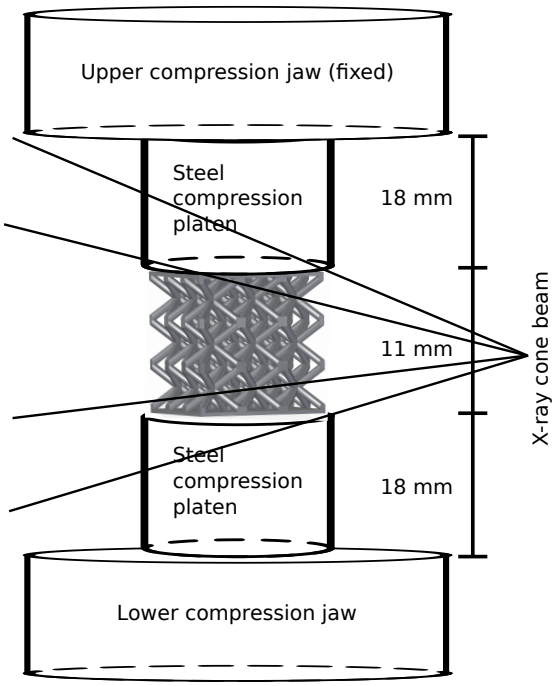

Figure 5.1: Schematic of the alignment of the $3 \times 3 \times 3$ lattice structure in the Deben load rig for *in-situ* compression.

The data was evaluated by means of digital volume correlation (DVC). The algorithm implemented in Avizo 9.4 (ThermoFischer, Berlin, Germany) was used. For DVC, the volume was divided into sub-volumes. Each of them was traced by the DVC algorithm [169]. The minimum size of the sub-volumes was limited by the memory of the graphic card (11 GB). The mesh-size for the sub-volumes was $40 \times 40 \times 40$ voxel. This corresponds to the resolution of the DVC algorithm. Since the upper jaw of the load stage was fixed, the CT-volumes had an inherent reference. However, an elastic or even plastic strain within the steel compression platens must to be taken into account. Therefore, an additional software-based registration was performed to mitigate the error of DVC.

5.1.2 Results

The *in-situ* compression test was first evaluated according to the force-displacement and the force-time diagram in Figure 5.2. The displacement used in Figure 5.2 was read out by the motor encoder of the load stage. The maximum displace-

ment was observed to be 1.4 mm at 5 kN. This value corresponds to 12.73 % of the sample height. Plastification starts at about 3 kN force and a 0.35 mm displacement. After unloading, the decrease in the displacement corresponds to an elastic relaxation. The slope in the elastic region for loading and unloading is the same. This indicates that the structure is still intact and no damage in form of cracks occurred.

Figure 5.2b shows the force relaxation over time. Such relaxation occurs every time the rig is set under displacement control. Such a relaxation could trigger a motion-induced blurring in the CT data. Therefore, the CT scan was started with a delay of about 5 min marked by the vertical dotted lines.

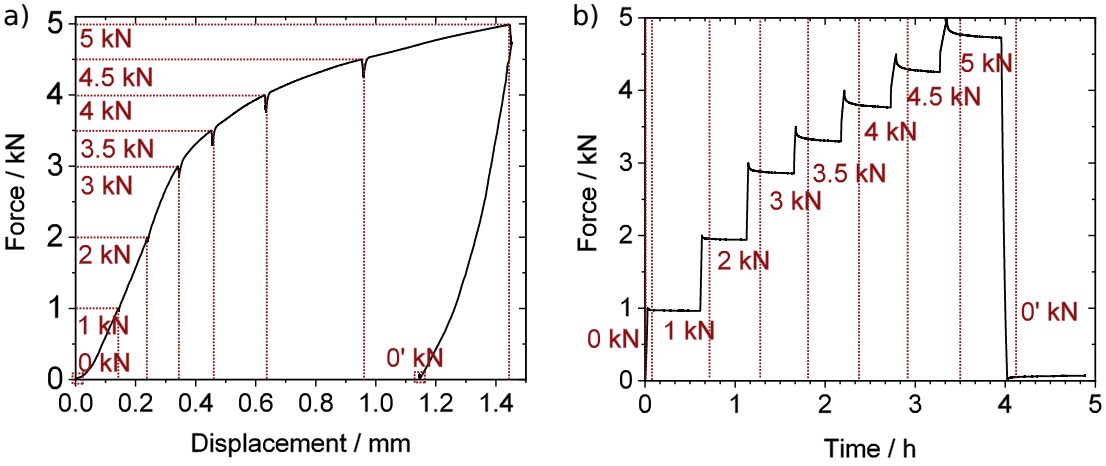

Figure 5.2: a) Force-displacement and b) force-time diagram for *in-situ* compression test.

The 3D-rendered lattice structure is shown before and at the maximum compression (5 kN) in Figure 5.3a and b, respectively. This deformation is analysed by DVC.

5.1.3 Discussion

The results of the DVC are presented in form of the absolute value of the displacement and of its vector field (see Figure 5.3c and d, respectively). The two presentations are complementary. The deformation of the first half of the upper row of triangles is negligible. In fact, due to the attached plate, the struts are stabilised. In fact, no bending was observed for the struts close to the compression plates. However, the connections of the struts to the compression plate are visible from the outer side of the compression plate in form of circles with

lower roughness. The conclusion is that the struts pressed the compression plate against the steel compression platens, so that the outer surface of the compression plate became smoother in this regions.

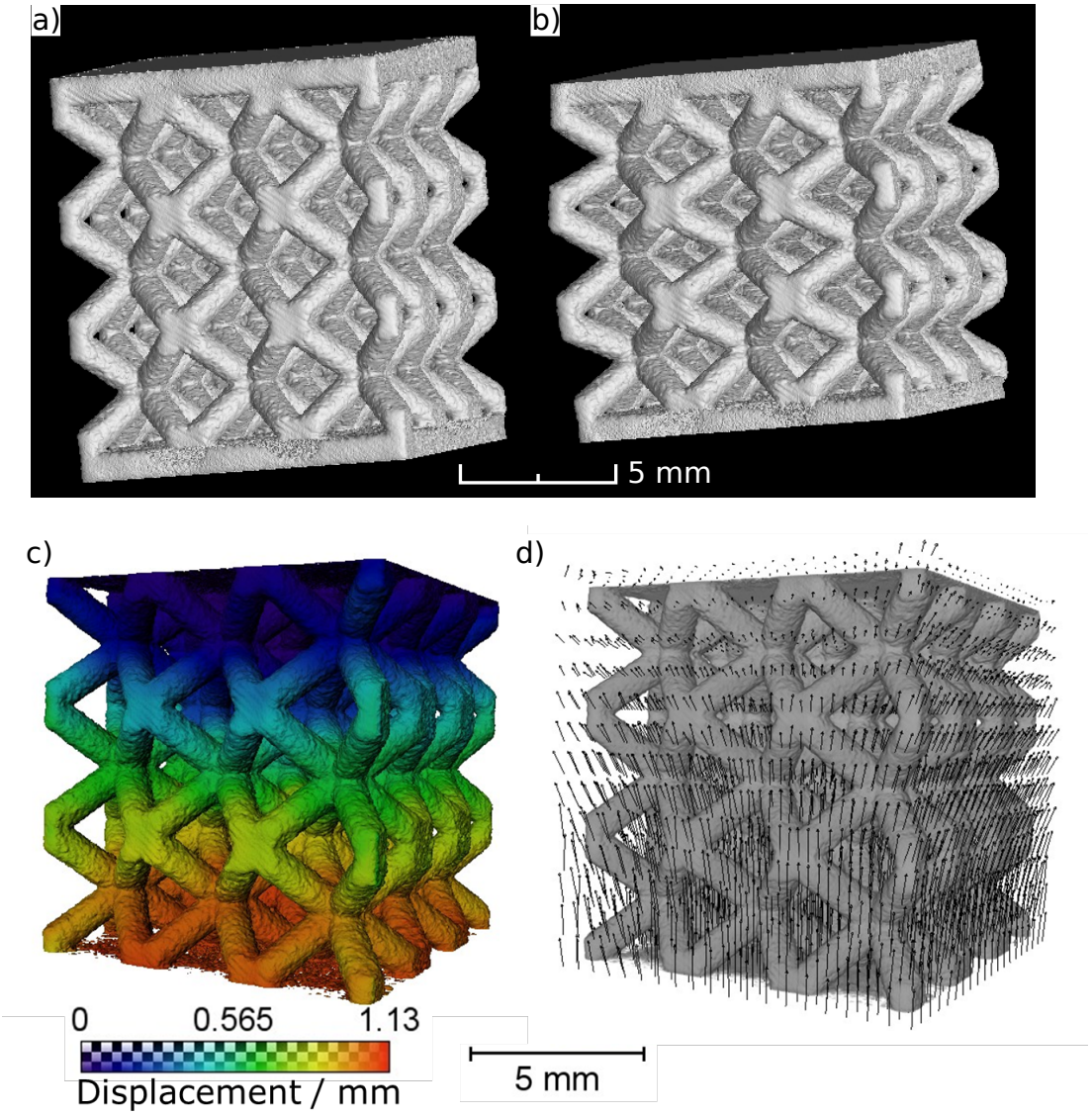

Figure 5.3: 3D rendered volume of a $3 \times 3 \times 3$ lattice structure a) before and b) after compression with 5 kN. The displacement field calculated by means of DVC is shown as c) color-coded absolute value and d) vector field

The connections between the first (attached to the plate) and the second row of unit cells (immediately underneath) have a higher degree of freedom. The directions of the displacement given by the vector field in Figure 5.3d, show a preferred

outward orientation. This indicates folding of the structure. Since a single strut is too stiff to deform or bend, the whole assembly is folded accordion-like, implying that the knots are the weakest points of the structure. The movement of the lowest plane of the unit cells is predominantly upwards. The deformation happens plane-wise. This confirms that the single strut are stiffer than the knots. This folding process enlarges the angle between the connecting struts at the knots. The increased angle leads to an even weaker unit cell. The other planes of unit cells do not start to deform before the currently weakest plane is folded completely.
In conclusion, the lattice deformation is knot-dominated rather than strut-dominated. These observations by DVC are in good agreement with compression tests on larger structures [170] and research results from Maskery *et al.* on similar structures [171].
In the chapters 4.2 and 4.3 a porosity accumulation and increased roughness was found for the DS of the individual struts. The fingerprint of these microscopic defects is not significantly visible in the macroscopic mechanical behaviour.
Firstly, the resolution of the DVC-algorithm ($= 20\,{}^{\mu\mathrm{m}}/_{\mathrm{voxel}} \cdot 40\,\mathrm{voxel} = 0.8\,\mathrm{mm}$) is in the range of the strut diameter. A further improvement is difficult to achieve. At that level of CT resolution no feature within a strut is resolved. Sub-volumes within a strut are therefore not traceable for the DVC algorithm. Each sub-volume has to contain a certain amount of strut surface.
Secondly, it is expected that the stress concentration in the knots dominate the failure mechanism. The knot is the junction of eight struts and therefore experiences a higher stress concentration.

5.2 Distortion during Production

5.2.1 Experiment

The $7 \times 7 \times 7$ lattice structure was scanned at a BAM in-house built CT-facility. The system is a combination of a Nikon Metrology Source (reflection Target with 320 kV maximum voltage) combined with a 4K Perkin Elmer detector. Compared to the GE v|tome|x 300L reflection target, the Nikon reflection target has a longer stability of the focus spot and is therefore optimised for the smaller pixel pitch ($100\,\mu\mathrm{m}$) of the 4K Perkin Elmer Detector. The time necessary for a statistically equivalent radiography at the BAM in-house built CT-facility is 4 times higher at the same magnification compared to the GE facility (which has a detector with

200 μm pixel pitch). The tube settings were close to the maximum: $U_t = 310\,\text{kV}$ and $I_t = 300\,\mu\text{A}$. Due to the strong absorption and therefore weak transmission signal, the detector was binned to 2047×2047 pixel. Radiographs were acquired with 8 s per projection. 3000 projections were required leading to total measurement time of 7 h with a tube power of 93 W. This represents the limits in term of stability of the source. Filters of 1 mm of aluminium and 0.25 mm of tin were used to suppress the beam hardening artefact. A voxel size of 38 μm was achieved.

The nominal-actual comparison (NAC) was performed by VG studio MAX 3.2. The algorithm compares the position of the actual surface with the position of the nominal surface. The algorithm estimates for a small element of the nominal surface the distance towards the actual surface. The search is performed along the perpendicular direction of the nominal surface element. The result is a distribution of the nominal surface as a function of the distance between nominal and actual surface (see Figures 5.4 and 5.5). This distance is called deviation.

5.2.2 Results

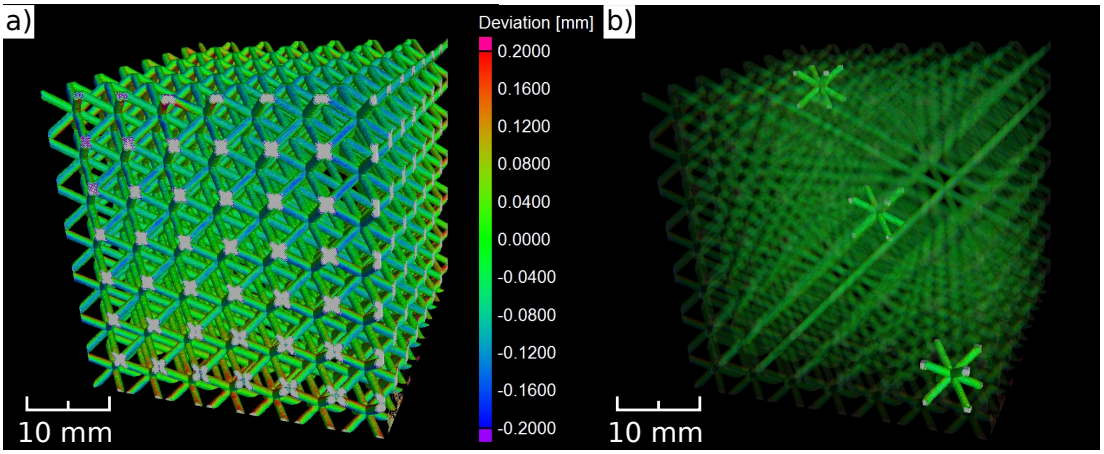

Figure 5.4: a) The nominal actual comparison for the $7 \times 7 \times 7$ lattice structure and b) the three unit cells (UC) as ROIs

The NAC of the $7 \times 7 \times 7$ lattice structure is shown in Figure 5.4. For a NAC, the most important step is the registration of the nominal CAD geometry onto the actual CT geometry. Different options are available to perform this registration. Beside the best fit registration as the most common tool [172], it could be more suitable to perform a best fit registration only for distinct regions. In Figure 5.5

three different registration are compared for four different regions (*i.e.* the full lattice structure and three unit cells (UC) distributed along the room diagonal of the lattice structure, see Figure 5.4b). Figure 5.5a presents the results of the NAC for the full lattice structure (black line).

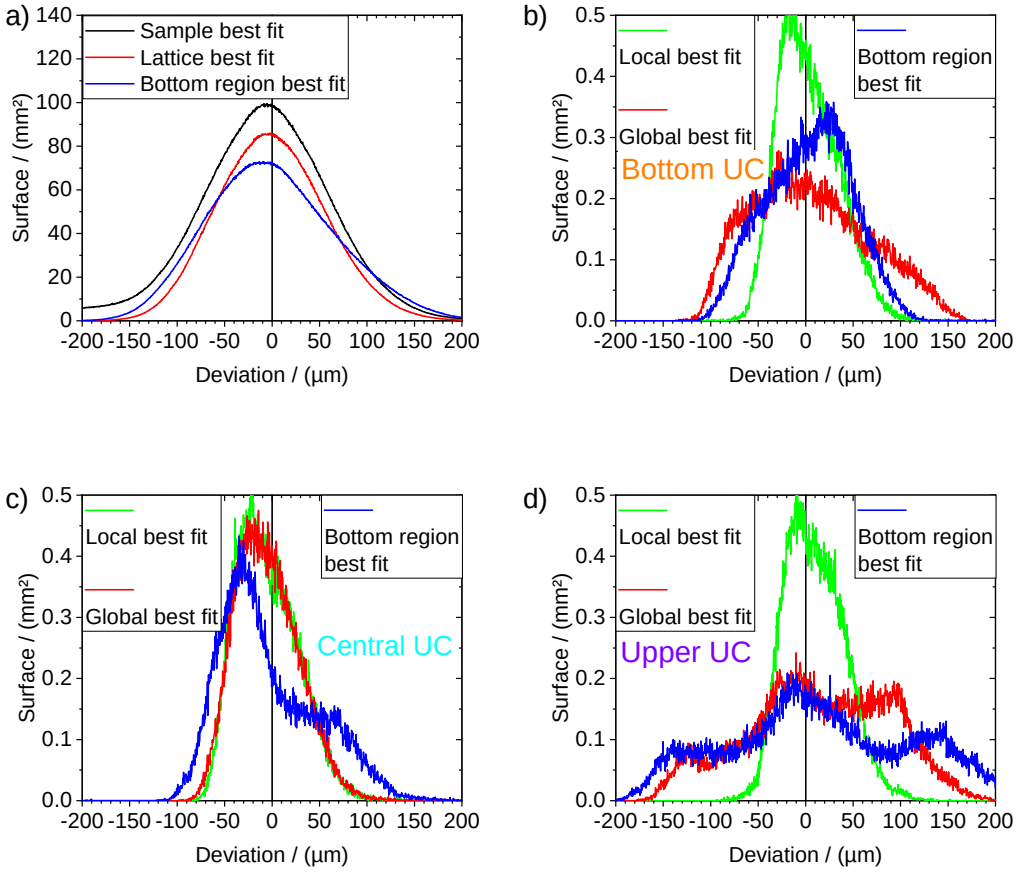

Figure 5.5: The deviation between nominal and actual surface is presented for different registrations. a) The NAC for the full sample (black, with compression plate) registered by best fit, the lattice only (red, virtually removed compression plates) registered by best fit, and the lattice only (blue) by best fit for the bottom region; the NAC for b) the bottom c) the central and d) the upper UC registered by local best fit (green), global best fit (red) and bottom region best fit.

The compression plates are virtually removed as a surface determination failed in some locations due too their strong X-ray absorption. The removal of the compression plates decreased the amount of surface but did not shift the distribution in Figure 5.5a (red line). Both curves have their global maximum at a deviation < 0. This is in good agreement with the volume shrinkage observed

for the struts (see Figure 4.11). If the best fit was performed only on the lowest plane (7×7) of unit cells (*i.e.* bottom region best fit), the deviation is spread over a wider range. This symmetric change in the distribution of the deviation must be understood as a small shift between nominal and actual geometry.
A NAC based on a local best fit was applied on the three UCs shown in Figure 5.4b in addition to the global best fit and the bottom region best fit. The three UCs are named according to their position along the main diagonal of the lattice structure: bottom (first plane of UCs), central (fourth plane of UCs) and upper (seventh plane of UCs). The local best fit registration leads to similar results for all three UCs. This registration strategy shows the narrowest deviation distribution (green curve, see 5.5b-d). For the central UC the global and local best fit are in good agreement, see 5.5c. The bottom and the upper UC show a larger difference between local and global best fit registration. For the two UCs close to the edge of the lattice, the distribution of the deviation between nominal and actual surface is broader.
All three UCs behave as expected after the registration of the bottom plan of UCs: The distribution of the bottom UC became narrower. The central unit cell shows a deviation that is not visible for the global best fit registration (5.5c). The distribution of the deviation for the upper UC is more asymmetric than for the global best fit. This is because of the large distance between bottom and top. The region of registration and the region of evaluation (*i.e.* the upper UC) have the maximum distance in this case.
In the case of a local registration all distributions are symmetric and narrow (Figure 5.5b-d). The local fit is only sensitive to volume shrinkage since the distortion is averaged out by the local best fit. The smaller a volume becomes, the better the registration works (*i.e.* Even a circle can be fitted by a straight line if the ring segment is small enough). The results for global registration contain both volume shrinkage and part distortion. The difference between local and global fit allows, therefore, the evaluation of the distortion only.
The deviation functions from Figure 5.5b-d were treated individually for each UC. First the distributions were normalised. The local fit function was separately subtracted from the global best fit and the bottom region best fit. Afterwards, all functions were centred regarding their minimum. These differences are presented in Figure 5.6.
A lattice distortion is either a UC translation or rotation of a UC with respect

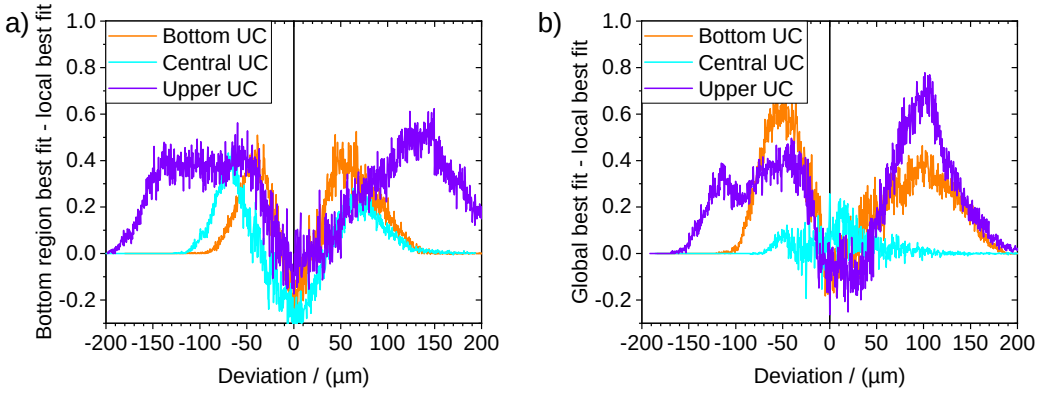

Figure 5.6: Both plots are based on the results presented in Figure 5.5b-d. The difference of the normalised deviation functions between a) the bottom region best fit and the local best fit; between b) the global best fit and the local best fit. The difference is presented for the three UCs (bottom (orange), central (turquoise), upper (purple)) as presented in Figure 5.4b

to its nominal position. A translation would lead to two sharp symmetric peaks (positive and negative deviation) with the deviation equal to the magnitude of translation, while a rotation would lead too a broad distribution of deviation.
In Figure 5.6a a superposition of both translation and rotation is recognisable. The peaks around $-50\,\mu$m and $+50\,\mu$m appear for all three UCs. In the case of the upper UC it is difficult to say whether the unit cell is distorted by means of a rotation or the whole nominal lattice is rotated. This uncertainty is due to the strut surface roughness that biases the best fit algorithm. However, the first peak is recognisably similar to the bottom UC and central UC.

5.2.3 Discussion

The difference between global best fit and local best fit is nearly zero for the central UC (see turquoise curve in Figure 5.6b). This indicates that in the case of the global best fit registration, the distortion of the lattice structure is calculated relative to the centre of the lattice structure. However, this represents averaged distortion over the sample height, see Figure 5.7. The part should instead show the minimum distortion at the bottom of the sample, because the build plate constraints the distortion of the part. Indeed, the build plate is the only reference that exists for L-PBF.

Even if reference objects are printed attached to the sample, *e.g.* spheres or plates, their relative distortion and volume shrinkage are unknown. Therefore, in the case of L-PBF it is reasonable to register only the bottom part of the sample (which was produced directly on top of the build plate). That would capture any distortion with respect to the build plate. A trade-off has to be made between a small region of interest for registration (to be as close as possible at the build plate) and sufficient statistics of material for best fit registration.

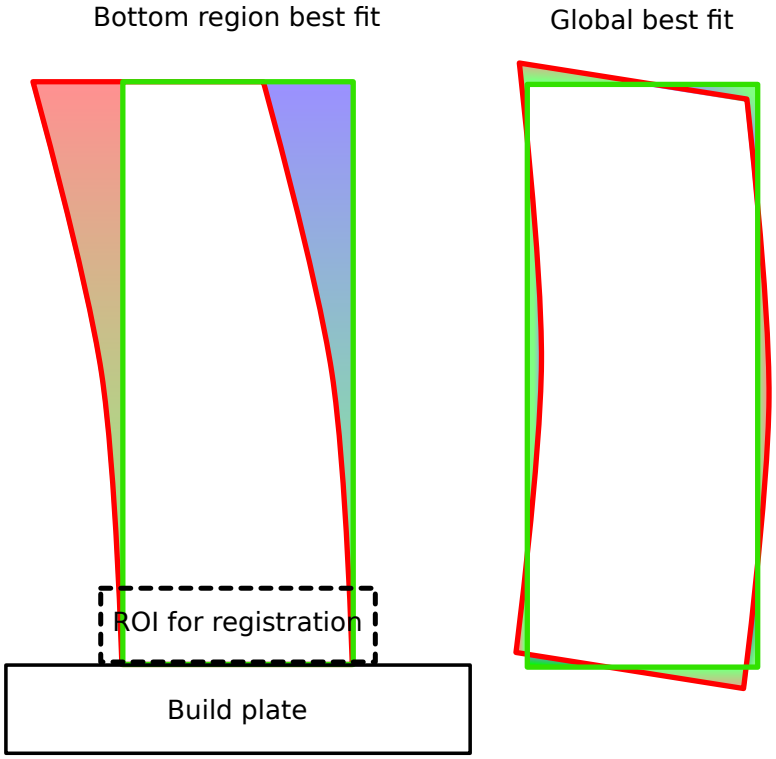

Figure 5.7: Schematic of the difference in NAC for bottom region best fit (left) and global best fit (right)

A featured base registration would not improve the results of the bottom region best fit. The features (*e.g.* spheres, cylinders, plates) would match the nominal geometry perfectly. However, they also need a least-squared error fit towards the actual volume. They specify the region of the best fit in the same way, such as a ROI would do.

5.3 Residual Stress

The lattice structure is characterised in terms of residual stress since it can lead to distortions as evaluated previously. Neutron diffraction (ND) was used for 3D stress analysis.

5.3.1 Experiment

The ND experiment was performed at the Stress-Spec beam line at the Neutron Reactor FRMII in Garching, Munich, Germany [173]. The investigation was focused on the single unit cell and the corresponding $3 \times 3 \times 3$ lattice structure. Both had a strut diameter of 1 mm and a strut length of 10 mm (see Figure 5.8). The edge length of a unit cell was therefore 5.77 mm. The characteristic length is the distance between knots, *i.e.* the half of the unit cell edge length (2.89 mm).

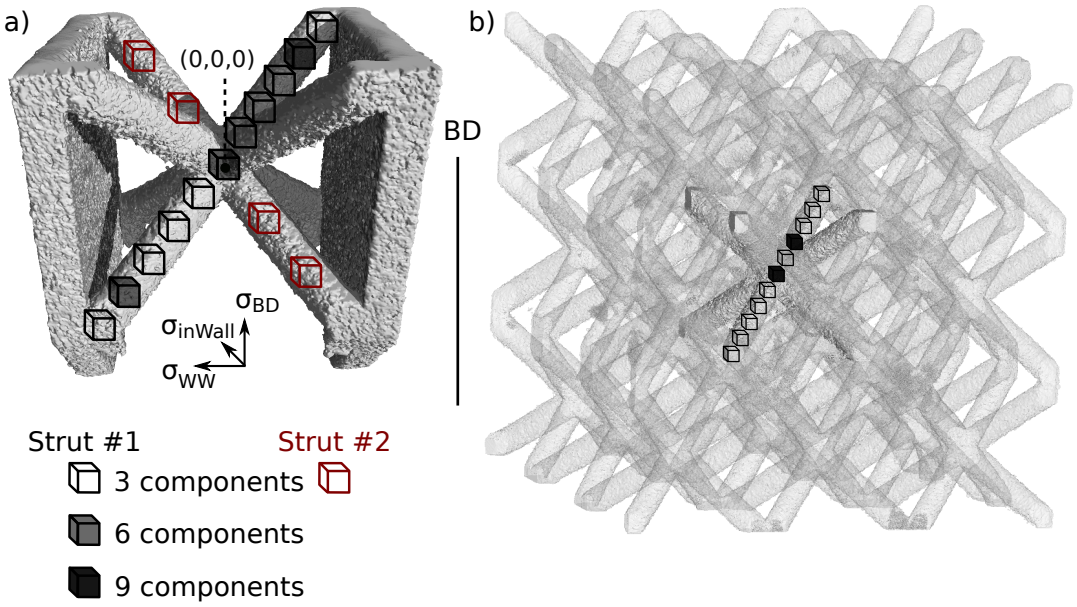

Figure 5.8: a) The actual volume (CT-data) of the single UC is shown. b) The $3 \times 3 \times 3$ lattice structure is transparent with a factor of 75 % highlighting the central UC. The compression plates were virtually removed to present a proper view on the lattice structure. The gauge volumes are sketched for both structures in white, grey, black, and red.

The gauge volume was defined by a primary slit of 1 mm × 1 mm and an oscillating radial collimator with FWHM = 0.5 mm in front of the detector. The wavelength of the neutron beam was tuned to 0.142 nm using a monochromator. In this way the diffraction signal of the {311} lattice plane was evaluated around a detector

position of $2\theta = 84°$. The reflection peak of the {311} lattice plane was chosen because it has been shown to be most representable for the macroscopic mechanical behaviour of Nickel [174]. The diffraction elastic constants $E^{h,k,l} = 193.5\,\mathrm{GPa}$ and $\nu^{h,k,l} = 0.305$ were used for the stress calculation [112]. These values have been estimated experimentally on IN 625 manufactured by laser metal deposition and represent the state-of-the-art in literature.
Eleven gauge volumes were measured along one strut in the single UC and four points along a perpendicular strut to prove the symmetry of the UC. At least three strain components were determined. Eleven points with three strain components along a strut were measured for the centre UC of the $3 \times 3 \times 3$ lattice structure, at the same relationship as for the single UC. Three additional directions (axial component of the strut, radial component of the strut, and a randomly direction) were measured at three points in the single UC. For the $3 \times 3 \times 3$ lattice structure, nine components (see Table 5.1) were measured at two gauge volumes within the $3 \times 3 \times 3$ lattice structure. The distribution of the gauge volume positions is shown in Figure 5.8.
The counting time was 30 min for each component. The (ϕ, ψ)-angles chosen for each point are reported in the sample coordinate system in Table 5.1 (compare with, Figure 2.6)

Table 5.1: Chosen (ϕ, ψ)-angles in the sample coordinate system

	σ_{inWall}	σ_{BD}	σ_{WW}	σ_{ax}	σ_{rad}	σ_{ran1}	σ_{ran2}	σ_{ran3}	σ_{ran4}
ϕ	0°	−90°	0°	−45°	−45°	−30°	−60°	0°	−80°
ψ	90°	90°	0°	125°	35°	20°	40°	10°	75°
#	1	2	3	4	5	6	7	8	9

The most crucial part of the experiment was the alignment within the lattice structures, as the gauge volume had the same size as the struts. A mismatch between the centre of gauge volume and the centre of gravity for scattering would lead to pseudo peak shift. Therefore, extreme care was used in performing the 'entrance scans', and the alignment was made with the best accuracy of the instrument. An Eulerian Cradle (χ-rotation) was mounted on top of the rotation stage (ω-rotation). A second rotation stage (ϕ-rotation) was mounted on the Eulerian cradle together with three step motors allowing translation along x, y, and z direction.

The alignment of the UC towards the gauge volume started with an optical alignment of the central knot by means of a theodolite. Afterwards, a scan in x-, y-, and z-direction was performed to find the maximum of the diffracted signal on the 2D detector. A movement along the strut (*i.e.* the room diagonal of the BCC-cell structure) was performed by using the same step width along all three translation axes. The strut was proved to be free of distortion in advance by a NAC between a CT-scan and the CAD-file, see Figure 5.9. The same procedure was used to align the $3 \times 3 \times 3$ lattice structure in the best manner.
Eventual errors in the alignment were corrected by 'mirror' measurements for the two components σ_{inWall} and σ_{BD}: Both in-wall and build directions were measured at ϕ and $\phi + 180°$. The above mentioned pseudo strain is average out by this method [175]. No significant difference was found between the two measurements. This confirmed that the alignment was excellent; nevertheless the averaged peak position was used for strain and stress analysis.

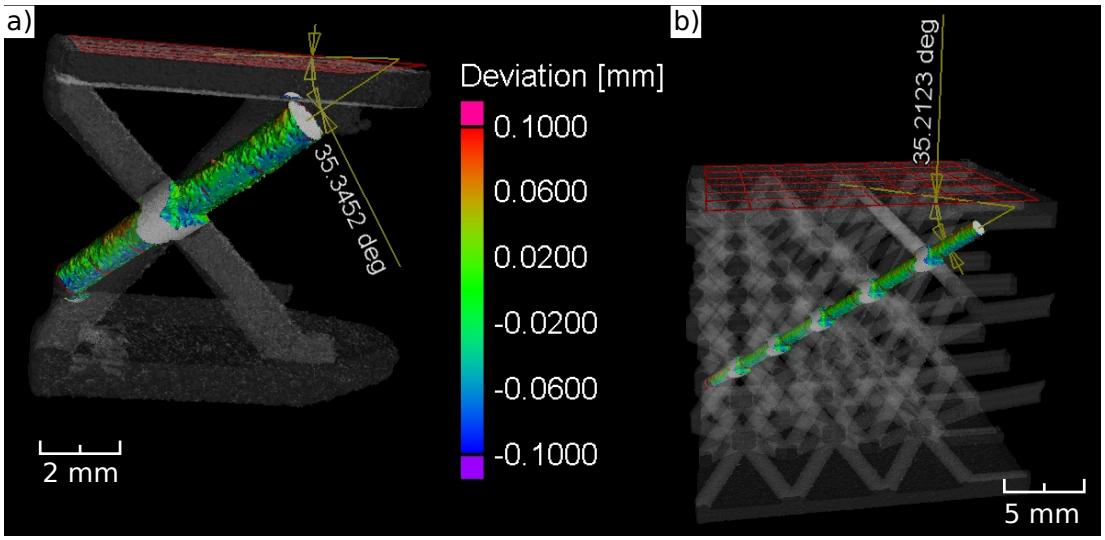

Figure 5.9: a) The NAC of a) the single unit cell and b) the $3 \times 3 \times 3$ lattice structure

A short distance between sample and primary slits was needed to avoid beam divergence effects. However, it reduced flexibility in rotation. The ω-rotation was limited by the Eulerian cradle. That led to an offset of 1.5°, *i.e.* $\omega = 40.5°$ was used instead of $\omega = \frac{1}{2} \cdot 2\theta = 42°$. This offset induced a precession of the scattering vector around the ϕ-rotation axis for $\chi \neq 0°$. The ω-offset was corrected by an offset of $\phi_{offset} = 1.5°$ in the case of $\chi = 0°$. For all other direction it will lead to a small offset in the measured strain direction, which was assumed to be

negligible.
The alignment of both the single UC and the $3 \times 3 \times 3$ lattice structure was proved by means of CT reconstructions. A plane was fitted to the compression plate and a cylinder to the strut that was investigated. The angles between the fitted planes and cylinders are presented in Figure 5.9. The angle was found to be 35.35° for the single UC and 35.21° for the $3 \times 3 \times 3$ lattice structure. The strut was assumed as a perfect room diagonal during the ND experiment. The deviation to the nominal angle of $\arccos(\frac{1}{\sqrt{3}}) = 35.27°$ is below 0.3 %. The angle of the strut is therefore proved to be undistorted (on average). Local distortions could also influence the ND experiment, but a distortion between the printed strut and the nominal cylinder is not perceptible within the resolution of the CT-scan (around 50 μm). The difference is dominated by the roughness of the strut. That roughness in terms of P_a is known to be around 40 μm (see Figure 4.9a). That covers the range from yellow to turquoise in Figure 5.9.

5.3.2 Results

The plots in Figure 5.10 show the calculated stress as a function of the *height* (*i.e.* the Cartesian z-component, see Figure 5.8). As described above, the movement along the strut was performed by translating the sample with the same step width along x-, y-, and z-component. The distance between the points in 3D space is $height \cdot \sqrt{3}$. The *height* has a range of 5.77 mm corresponding to the strut length of 10 mm. The knot of the UC is defined as $height = 0$.
Neither the intensity- nor the FWHM-values presented above each stress plot in Figure 5.10 show any peculiarity. Together with the stress data, the intensity and the FWHM indicate a reasonable sample alignment. The error of stress measurement is in the range of $30 - 50$ MPa.
In general, all stress values are low ($-100\,\text{MPa} \leq \sigma \leq 100\,\text{MPa}$). One exception is σ_{BD} for the single UC in Figure 5.10b: The junction between the strut and the compression plate allows higher RS due to the larger amount of material along build direction (BD). In contrast, σ_{WW} and σ_{inWall} appear not to be influenced by the compression plate. The comparison between Figures 5.10c and d shows the effect of the compression plate.
A periodicity is recognisable for all three stress components determined in the $3 \times 3 \times 3$ lattice structure (Figure 5.10b, d, f). It seems to correspond to the periodicity of the lattice structure (knot-strut-alternation).

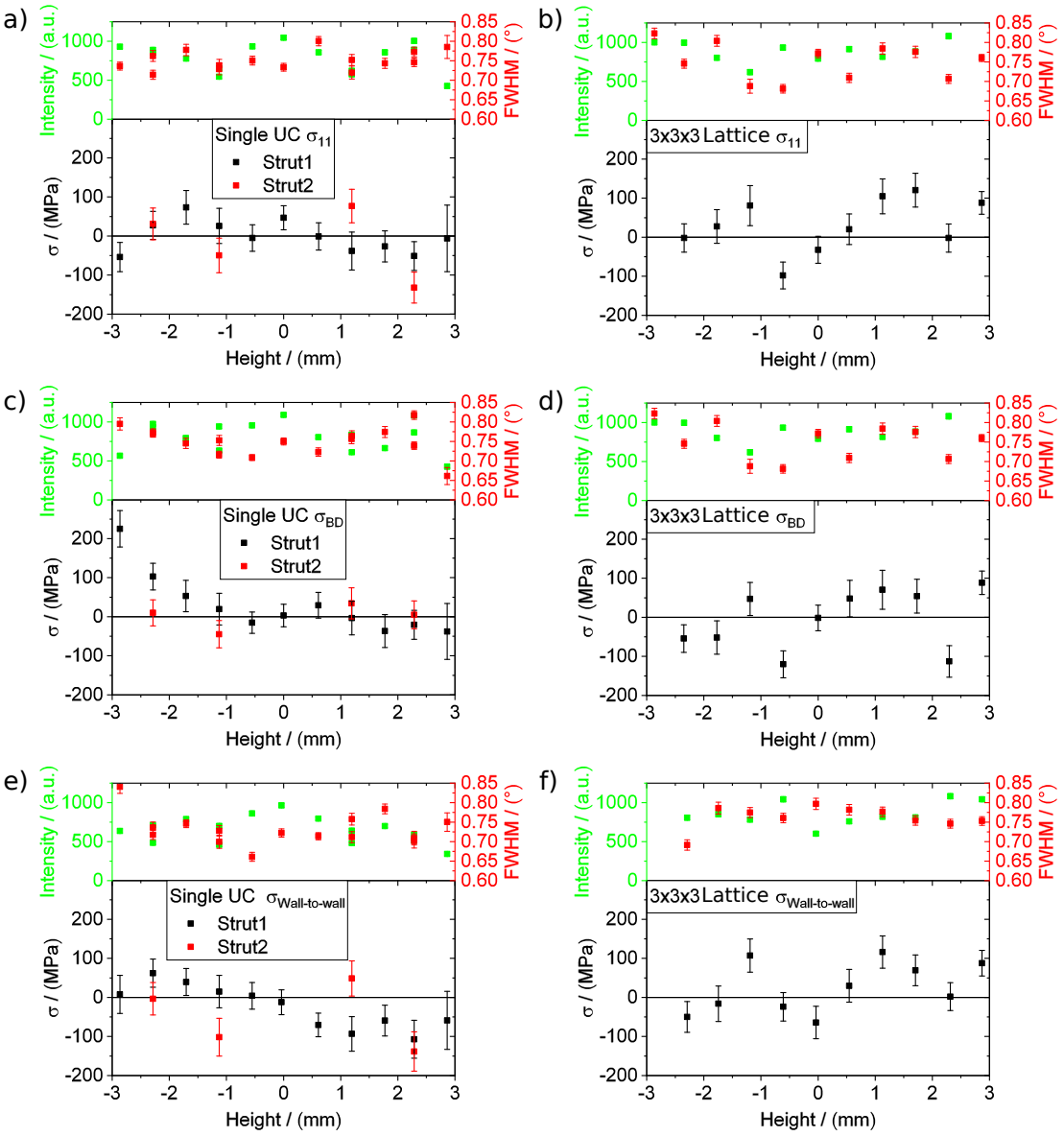

Figure 5.10: The stress values for three orthogonal stress components together with the peak intensity (green) and the peak FWHM (red) above each profile for a), c), e) the single UC and b), d), f) the $3 \times 3 \times 3$ lattice (corresponding to the central UC).

The stress values of the strut #1 (black) and strut #2 (red) do not coincide for the single UC (see Figure 5.10a, c, e). The expected symmetry between the two struts is not confirmed by this data. One could argue that at least σ_{BD} (5.10c) coincides for strut #1 (black) and strut #2 (red). The other two components (σ_{inWall} and σ_{WW}) lack of this symmetry.
The principal directions were calculated with a self-written python script, see chapter A.4, source code 3, according to the theory introduced in chapter 2.4.

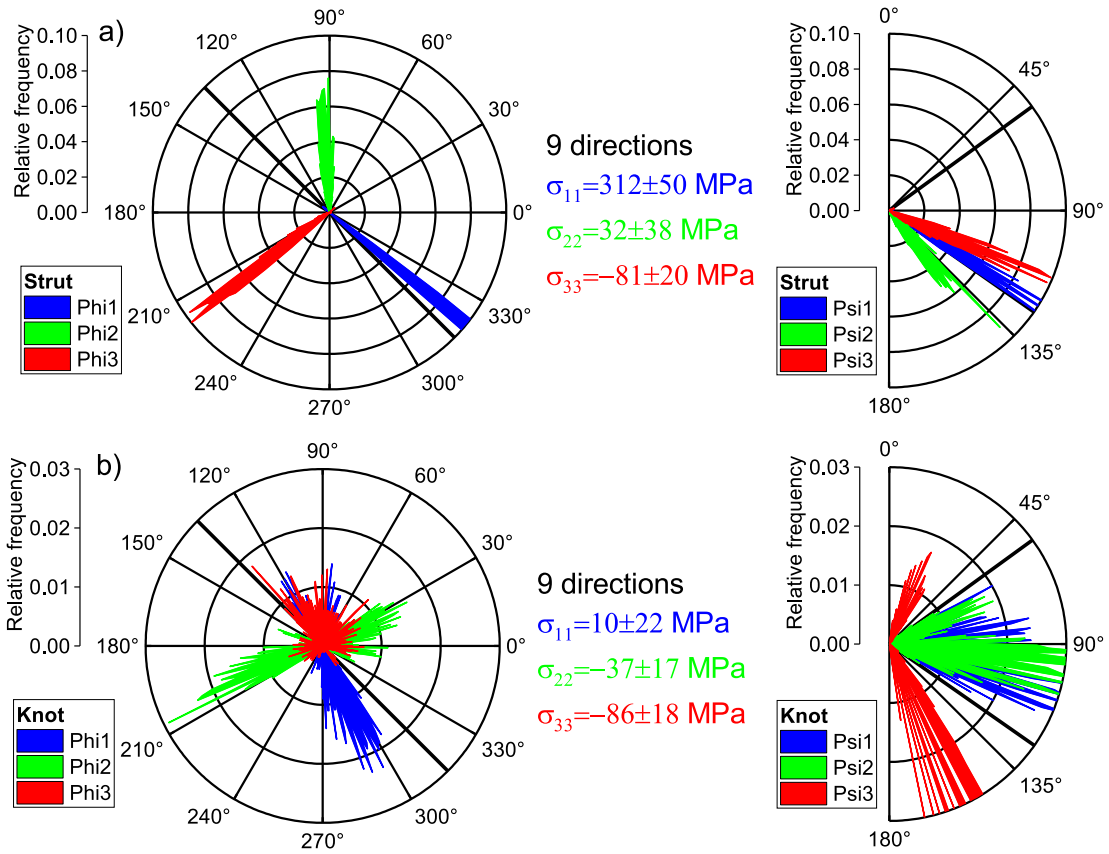

Figure 5.11: The results of the principal direction estimation for a) the strut and b) the knot in the central UC of the $3 \times 3 \times 3$ lattice structure in the sample coordinate system in terms of the eigenvalue σ_{ii} (middle) and the azimuthal phi_i^S (left) and polar ψ_i^S (right) angles of the corresponding eigenvector. The solution is presented for all nine measured directions.

All results represent the statistic evaluation of 1000 iterations to estimate an error band for both the principal stress directions and the principal stress values. The results of the principal direction calculations using all nine measured direction, see Table 5.1, are presented for the strut and the knot of the central UC of the

$3 \times 3 \times 3$ lattice structure in Figure 5.11. These two gauge volumes are presented as dark grey cubes in Figure 5.8b. The results are presented in form of the the azimuthal and polar angle of the eigenvectors in the sample coordinate system (ϕ^S (left) and ψ^S (right)). ϕ^S and ψ^S are also sketched in Figure 2.6. The corresponding eigenvalues are given in form of the stress σ_{ii} value corresponding to phi_i^S and ψ_i^S.

The strut (Figure 5.11a) shows a prominent stress of $\sigma_{11} = 312 \pm 50\,\text{MPa}$ along $\phi_1^S = 310°$ and $\psi_1^S = 122°$. This direction correlates well with the strut orientation in the sample coordinate system $\phi_{strut}^S = 315°$ and $\psi_{strut}^S = 125.3°$ which are marked as thick black lines in the Figures 5.11-5.13 and A.4-A.8. In comparison, the knot shows significantly lower stress and also a broader distribution for the principal stress direction, as expected, see Figure 5.11b.

It is important to note, that Figure 5.11a has a different scale for the relative frequency compared to 5.11b. The same scale would mislead any prediction of the principal direction. A diagram with the same scale is presented in Figure A.4.

By reducing the number of measured direction $d_{\phi,\psi}^{311}$ from nine to seven directions to calculate eigenvalues and eigenvectors, the directions and absolute stress values do not change significantly. The only difference is that the algorithm returns the exact opposite angles, that correspond anyway to the same stress direction, see Figure 5.12a and A.8a. If we input seven directions in the algorithm, the results for the principal stress directions are independent of the choice of the seven direction, see Figure 5.12b. However, the principal stress values are affected. In Figure 5.12a the last two random directions in Table 5.1 are neglected while in Figure 5.12b the two directions with the largest μ-strain values are neglected.

The results for six measured directions (see Figure 5.13a) are significantly different from the results for nine (Figure 5.11a), eight (Figure A.8a) and seven directions (Figure 5.12a). Unrealistically, the calculated directions are clearly uncorrelated from the strut orientation.

The same calculations were performed for the knot in the centre of the $3 \times 3 \times 3$ lattice structure. The results are presented in Figure 5.11b, A.8b, A.6 and A.7. In comparison to the results for the strut for nine components in Figure 5.11b, the stress value σ_{11} is small, while σ_{22} and σ_{33} are the same within the error. In addition, the distribution of ϕ_i^S and ψ_i^S are isoaxler. No prominent direction can be estimated. That correlates well with the position of the knot at the junction

of four struts. While it is trivial that the material is more isotropic at the knot than at a single strut, it can be non-trivially concluded that the principal stress directions are dominated by geometry.

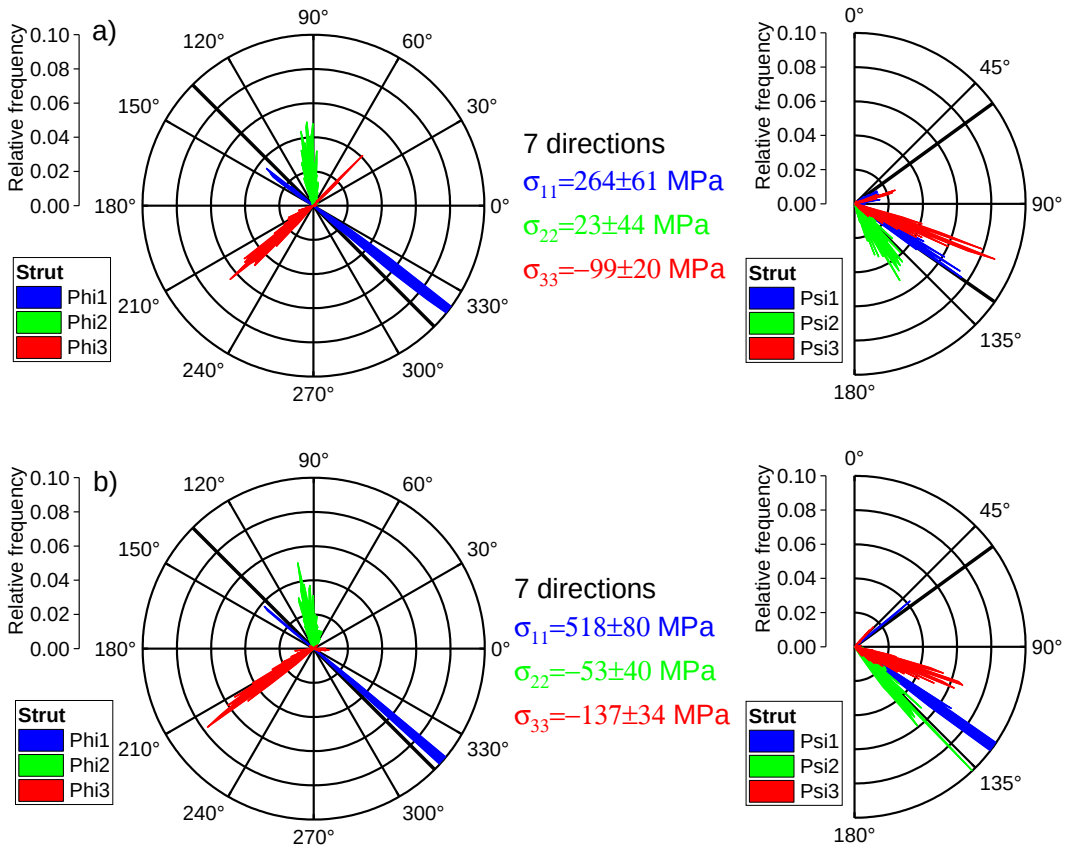

Figure 5.12: The results of the principal direction estimation for the strut in the central UC of the $3 \times 3 \times 3$ lattice structure in the sample coordinate system in terms of the eigenvalue σ_{ii} (middle) and the azimuthal phi_i^S (left) and polar ψ_i^S (right) angles of the corresponding eigenvector. The solution is presented for a) the first seven directions from table 5.1 and b) the seven directions with the lowest μstrain value.

An artificial increase of the measurement error by a factor of 5 (from about 100 μstrain to 500 μstrain) for every direction lead to broader angular distribution of ϕ^S and ψ^S together with an increased error on the stress value by a factor of 3 (compare Figure 5.11 with A.5). While in the case of the strut, the principal directions are still recognisable with a large measurement error of 500 μstrain (Figure A.5a), the directions for the knot (Figure A.5b) are lost. This indicates that an increase of the measurement error biases the results of the principal

directions. At gauge volumes with low measured strain values (*i.e.* the knot), it is hardly possible to find reliable principal stress directions.

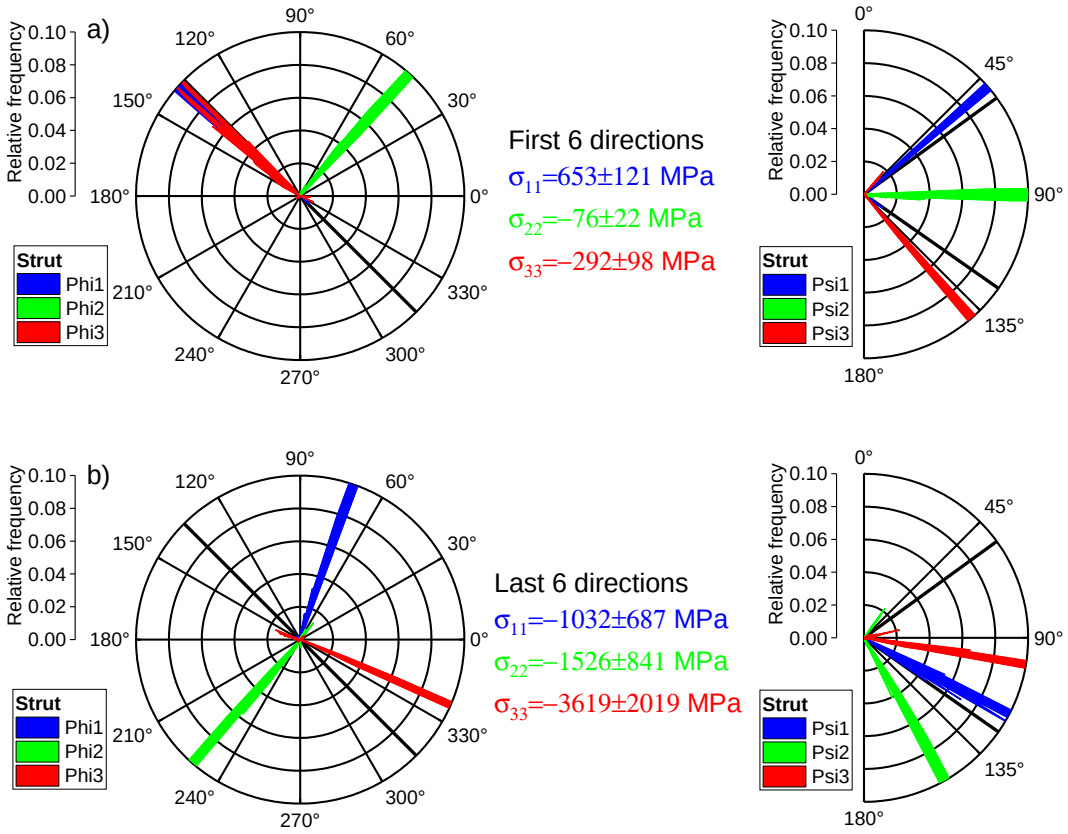

Figure 5.13: The results of the principal direction estimation for the strut in the central UC of the $3 \times 3 \times 3$ lattice structure in the sample coordinate system in terms of the eigenvalue σ_{ii} (middle) and the azimuthal phi_i^S (left) and polar ψ_i^S (right) angles of the corresponding eigenvector. The solution is presented for a) the first six and b) the last six directions from table 5.1.

Similar to the results for the strut, the knot shows also a significant difference in principal stress orientation between calculations using six, seven, eight, and nine directions. The results for six directions, shown in Figure 5.13a and A.7a, are even the same for the strut and the knot. However, the choice of the six directions exhibit a high impact on the principal stress directions, see Figure 5.13b and A.7b. Together with unrealistic principal stress values (higher than the yield strength of IN 625 (400 MPa[176]-793 MPa[177])), this leads to the conclusion that the first six components are either poorly chosen or they do not yield in significant strain values to calculate the principal directions properly. In contrast in the case of

seven directions, we found no choice of the measured direction on the resulting

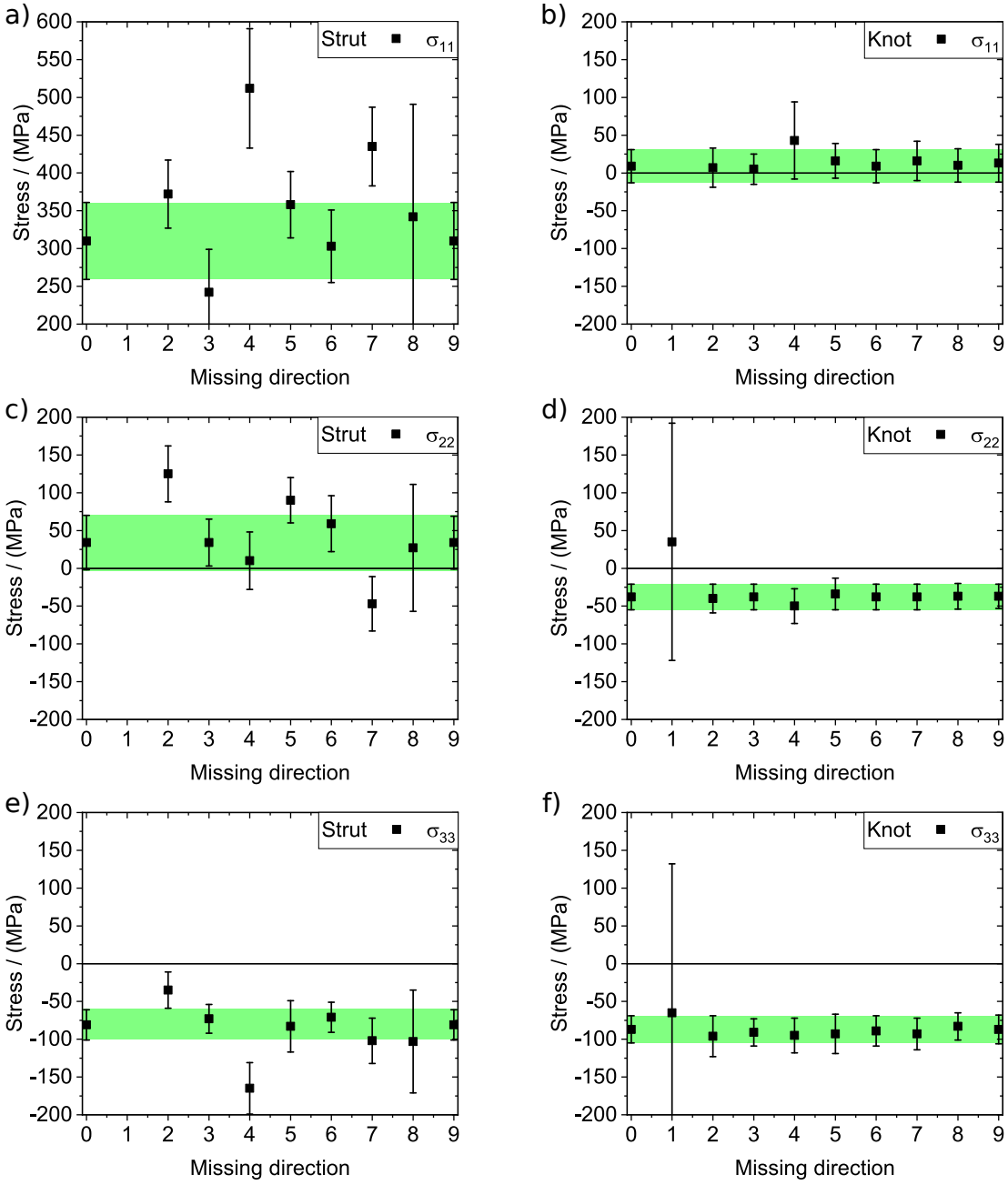

Figure 5.14: The principal stress magnitudes (σ_{11}, σ_{22}, σ_{33}) is shown in the case if eight measured directions were used for stress calculation for a), c), e) the strut and b), d), f) the knot in the $3 \times 3 \times 3$. The missing direction on the x-axis refers to the missing direction in table 5.1 whereas "0" means the calculation with nine components. The green band represents the error bar of the calculation with nine strain measurements.

principal directions.
The principal stress magnitude was also evaluated. The stress values are shown in Figure 5.14 for the case of nine measured directions and for the nine possible combinations with eight measured direction for both the strut and the knot. The green band marks the error range of the stress value calculated using all nine measured directions.
In the case of the strut (Figure 5.14a, c, e) the results for eight directions are partly in agreement with the calculation for nine. In particular, if a significant directions ('4' or '7') are missing the results do not match the calculation for nine direction. Direction '4' is the axial component of the strut and direction '7' is the random direction with the least angular deviation from direction '4', see table 5.1.
In the case of the knot the principal stress magnitude does not vary with the choice of the measured direction as it does for the strut. This confirms that the stress state is more isotropic at the knot position, with lower stress values compared to the strut.

5.3.3 Discussion

The aims of this investigations were the determination of principal stress directions in lattice structures and the understanding of the scaling effect from a single UC to larger lattice structures.
There are two sources of error in determination of the principal stress directions and values:
The first source of error is a purely mathematical one. The solver (see, chapter A.4, source code 3, line 47) for the linear equation system (equation 2.17) is based on a least squared method and should therefore become more precise with an increased number of input directions. In theory six independent strain components should be sufficient. However, the more strain components are used to solve the system of linear equations (equation 2.17), the smaller becomes the error of the output. Especially if the measured strain values are just slightly larger than the experimental error, a higher number of linear equations solved the system more reliably, see Figure 5.11.
The second source of error has a physical basis. The stress state within the gauge volume influences the error of the determined directions. If the stress state would be nearly isotropic, *i.e.* the shape of the stress ellipsoid would be close to a sphere,

a small error in the measured strain component would lead to a large error in the determined principal stress direction. Even further, in a hydrostatic stress state all direction are principal. This is proved by the comparison of the stress state within the strut (see Figure 5.11a) and the stress state within the knot (see Figure 5.11b). In both cases nine strain components were measured. The first type of error (*i.e.* the mathematical one) is therefore the same. The stress state is expected to be more hydrostatic in the knot compared to the strut, as a knot is the junction of four struts. This leads, even for nine independent measurements to a large physical error for the determined principal directions.
For the strut, prominent principal stress directions were found together with a principal stress magnitude was heavily influenced by the choice of the measured directions. For the knot, the opposite case was observed: The principal stress directions were found to be less prominent, and the principal stress magnitudes were not significantly affected by the choice of the measured directions. These observations are in agreement with a strongly uniaxial stress state in the strut and a more isotropic stress state in the knot. A small change in the principal stress direction leads to a large change in the principal stress magnitude for the strut while the stress magnitude is less influenced by the directions for the knot, see Figure 5.15.

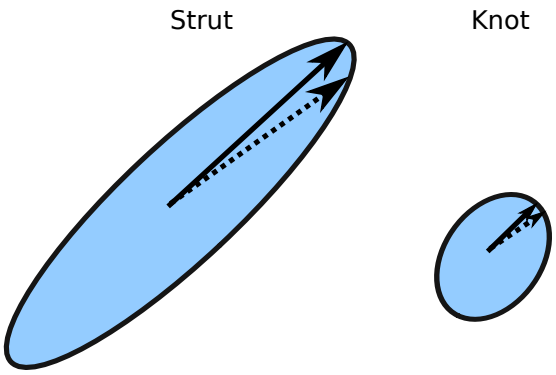

Figure 5.15: Schematic difference between stress state in the strut(left) and the knot (right).

The effect of the scaling was observed only for the building direction. An increase of σ_{BD} was observed at the junction to the compression plate at the bottom of the single UC. The other two stress components (σ_{WW} and σ_{inWall}) show no increase at that point. The 67°-rotation scan strategy is currently discussed to distribute the heat homogeneously in-plane (σ_{inWall} and σ_{WW}) but cannot correct

for the large temperature gradient along the BD [99, 100, 115, 178]. Since the temperature gradient is the origin of the residual stress, a larger σ_{BD} within the compression plate is reasonable. This would result in the observed increase of only σ_{BD}. A larger stress along BD within the compression plate was confirmed by XRD measurements. The results are shown in Figure 5.16.
In the case of the $3 \times 3 \times 3$ lattice structure, the central UC is not constrained by the compression plate but by 26 less rigid unit cells. An increased σ_{BD} is therefore not observed. Apart from this difference in σ_{BD}, the single UC and the $3 \times 3 \times 3$ lattice structure look similar as they both show low stress values in the measured directions.

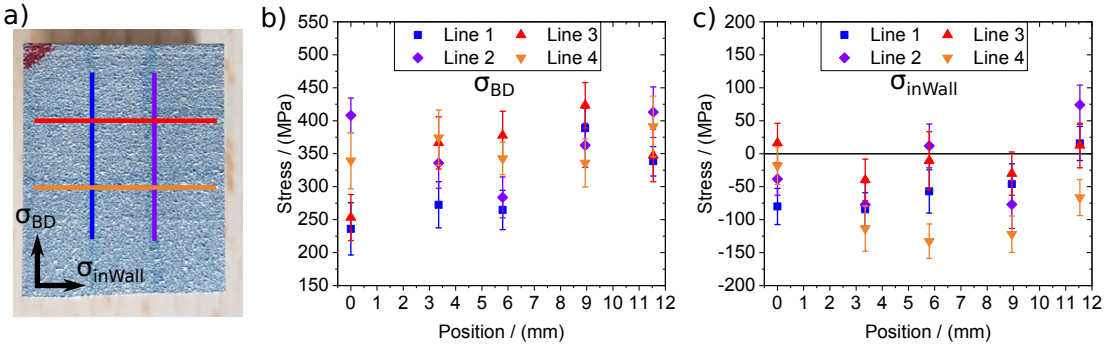

Figure 5.16: a) A photograph shows the position of the four line scans performed by means of XRD on the compression plate of the $3 \times 3 \times 3$ lattice structure. The stress results are presented b) for σ_{BD} and c) for σ_{inWall} in dependence of the height.

The principal stress analysis led to a clear difference between the strut and the knot position for both the principal stress directions and the principal stress values. We stated that the geometry has the largest influence. This implies that the microstructure is not responsible for the observed difference. In fact, the microstructure is shown in Figure A.3 and quantified in Figure 5.17 (Romeo Neumann-Salliwan, BAM, FB 5.2 is acknowledged). It was acquired on a cross section parallel to the strut axis by means of electron back-scattered detection (EBSD). The strut and the knot position showed the same microstructure in terms of grain size and grain orientation (see Figure 5.17). The mean grain size is 62 μm.
In addition to these two aims, a brief investigation of symmetry within the single UC was realised. The results for the four points measured in a second strut, show that the assumption of symmetry might be wrong. The difference between the black and red points in Figure 5.10a, c, e, is larger than the error. From

the manufacturing point of view, the only difference between the two struts is their tilt direction. Therefore, the laser penetrates them with a different relative angle. Mishurova *et al.* [101] discussed that the angle of laser penetration into the structure and into the powder bed influences the RS-state. On the example of the 90°-strut, the surface topography was as well observed to be heavily influenced.

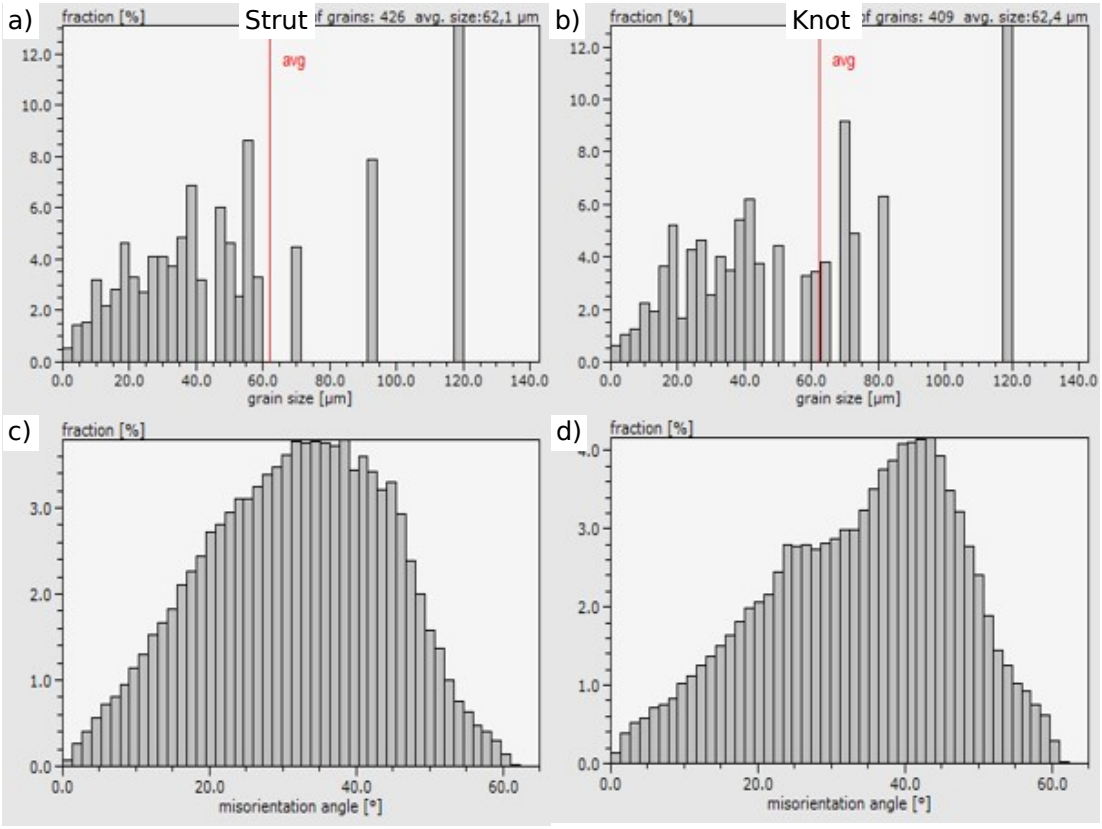

Figure 5.17: The grain size distribution of the single UC for a) a strut and b) a knot with the corresponding grain orientation for c) the strut position and d) a knot position. The distributions are calculated from Figure A.3. The images were acquired by Romero Neumann-Salliwan, BAM, FB 5.2

Finally, an important aspect, that might effect the measurement results, shall be discussed. This is the determination of the d_0 reference value. How to select a proper reference value is under current discussion, in particular for AM material, as it is shown in chapter 1. Within this thesis, the average of all $d_{\phi,\psi}$-values was used as the mean value cover a large part of the structures and many directions within the specimen [122, 179]. This was the only reasonable choice, also because the absolute value of the stress was not the major goal of the ex-

periment. An incorrect d_0 value would lead to a global shift of the RS profile by $\frac{E}{1-2\nu}\frac{\Delta d_0}{d_0}$ [99] (under the assumption of a constant d_0 for the whole sample). However, Wang *et al.* have shown that d_0 varied over the sample height due to a change in chemistry [113]. If this result will be reproduced for different alloys and different scanning parameters, the evaluation of RS by means of ND will be challenging. Therefore, the quest for a robust d_0 is a formidable task.

6 Concluding Remarks

The core of this work is the development and improvement of analysing methods and routines to investigate AM defects and characteristics in lattice structures.
In chapter 3 a workflow was presented, which allows the characterisation of the powder porosity, the particle packing density, the inter-particle distance, the particle size, and the particle shape, based on CT measurements. Synchrotron CT was used as the method of highest quality available.
The packing density is correlated with the size and the shape of the powder particles, in order to understand the powder bed quality. As shown in [180], a higher packing density correlates with a higher density of produced part. Therefore, the particle packing density of the powder bed is an important process parameter for L-PBF process. In section 3.3, it is discussed that the particle size correlates with the packing density. It is shown that the conversion from a polydisperse to a statistically equivalent bidisperse particle size distribution simplifies the correlation. The diameter ratio between small and large particles correlates well with the particle packing density, see Table 3.1 and Figure 6.1. The correlation needs to be verified on more powder batches, but the present results appear promising. They open the way to a broader application (ideally to any particle size distribution for Additive Manufacturing powder).
Another conclusion can be made regarding the relation between the shape of powder particles and the technique of their production. Plasma atomization promotes particles with lower anisotropy and larger sphericity compared to gas atomisation. This difference is more obvious for the anisotropy than for the sphericity.
The workflow in terms of the particle shape analysis allows understanding that the packing density is affected only to a minor extent by the particle shape, and hence the particle size has the major influence on the particle packing density.
The porosity within powder particles is compared to the porosity of processed parts, *i.e.* the struts. The comparison between pores within the powder and the strut is shown in Figure 4.4b. The porosity within the powder is 0.05 %. This is twice as high as the porosity in the struts, even though the pores in the powder are on average more than 10 μm smaller than the pores in the strut. We could deduce a reduction of entrapped gas, due to the melt process during L-PBF. At this point, it remains unclear whether the remaining pores in the struts are the

very same as those in the powder particles, or new pores are induced due to process-inherent flaws. In all struts, the remaining porosity is very low and in the typical range for optimised L-PBFparts ($0.2 - 0.02\,\%$, see [34, 42]). Significantly larger pores were found within the strut compared to the powder particles. In the case of the remaining pores, the larger pore size in the part can be explained by the expansion of the entrapped gas within a powder particle during melting. In the case of new pores, the pore size would be random. We assume that the remaining porosity in the strut is a result of the L-PBF process, *i.e.* gas entrapment in the melt pool, due to the Marangoni effect [44].

The porosity within the strut is also characterised regarding its position. The correlation between shape and position has not yet been reported in literature and allows the conclusion that pores with high anisotropy appear exclusively within $90\,\mu$m distance to the strut surface, see Figure 4.5 and 6.1. It is assumed that the material near the surface can freely deform thereby creating elongated pores, while in the bulk the hydrostatic stress induces round-shaped defects. The position dependence for tilted structures is in general agreement with the literature [54]. It was shown that a more upright part orientation promoted the suppression of pores smaller than $30\,\mu$m.

Similar to the powder particle analysis, a workflow is presented to quantify the surface topography of additively manufactured cylindrical struts used in lattice structures. The evaluation allows a deeper understanding of the influence of the build angle on parts manufactured by laser-powder bed fusion.
By transforming the strut surface from Cartesian to cylindrical coordinates it is observed that for tilted structures a higher roughness appears at the down-skin region. This higher roughness extends over a quarter of the strut surface, see Figure 4.8a and 6.1. This is due to the combined effect of laser penetration into the powder bed and of partially attached powder particles. The roughness is twice as high for a highly tilted strut than for a vertically built one.
Considering the estimated size of the powder particles (presented in Figure 3.7), $50\,\%$ of the particles are smaller than $17\,\mu\text{m} = D_{50}$ (by definition); it is then obvious that a mean roughness of $45\,\mu$m is in the size range of the largest particles. Indeed, in addition to the attached particles, uncontrolled flow of molten material certainly influences the mean primary surface profile (P_a). P_a at the DS increases

by a factor of 150 % while P_a at the US remains constant with the build angle. Tailoring the particle size may enable the surface topography to be optimised. The quantitative information about volume shrinkage can be used to correct parts design, in order to minimise the nominal-to-actual dimension difference.
Computed tomography allows the quantitative evaluation of internal porosity and surfaces topography, also in structures not accessible to conventional profilometry. This is particularly valuable in the case of lattice structures: Since struts are always built at an angle to the build direction, the understanding of the porosity and the surface topography in single struts (built at different angles) enables the optimisation of both the build job and the whole lattice structure itself.
For the sake of quality control and safety of such structures, as well as to assess their effective mechanical properties, it is indispensable to distinguish solid material from partially attached particles, since the latter do not contribute to the mechanical integrity. Particles that are only partially sintered to the part will not carry any load and will therefore bias the equivalent volume used for simulations of the mechanical response. In order to assess the load-carrying volume, this thesis recommends the use of the largest prism of solid material fitting into the sample projection along its axis. The analysis of the projections through the struts also revealed that the completely solidified material is not influenced by the build angle, while the number of attached particles is, see Figure 4.8b and 6.1.
The surface topography cannot be described by one parameter. This work shows the redundancy but also the complementarity between different surface characterisation methods for AM surfaces. A set of representative parameters is needed such as is exist for conventional material (R_a, R_z, R_q, R_{sk}, S_a, S_q, etc) [181]. The new parameters should of course be linked to the existing ones but must be tailored for AM features such as surface re-entrant features and attached powder particles.

As Additive Manufacturing enables the production of such complex lattice structures, the evaluation according to *in-situ* computed tomography and neutron diffraction was carried out for the first time on to the knowledge of the author.
An interesting effect, that is observed for both surface topography of the struts and residual stress determination of the lattice structure, is the influence of the tilted laser penetration into the powder bed. This occurs as soon as the sample is

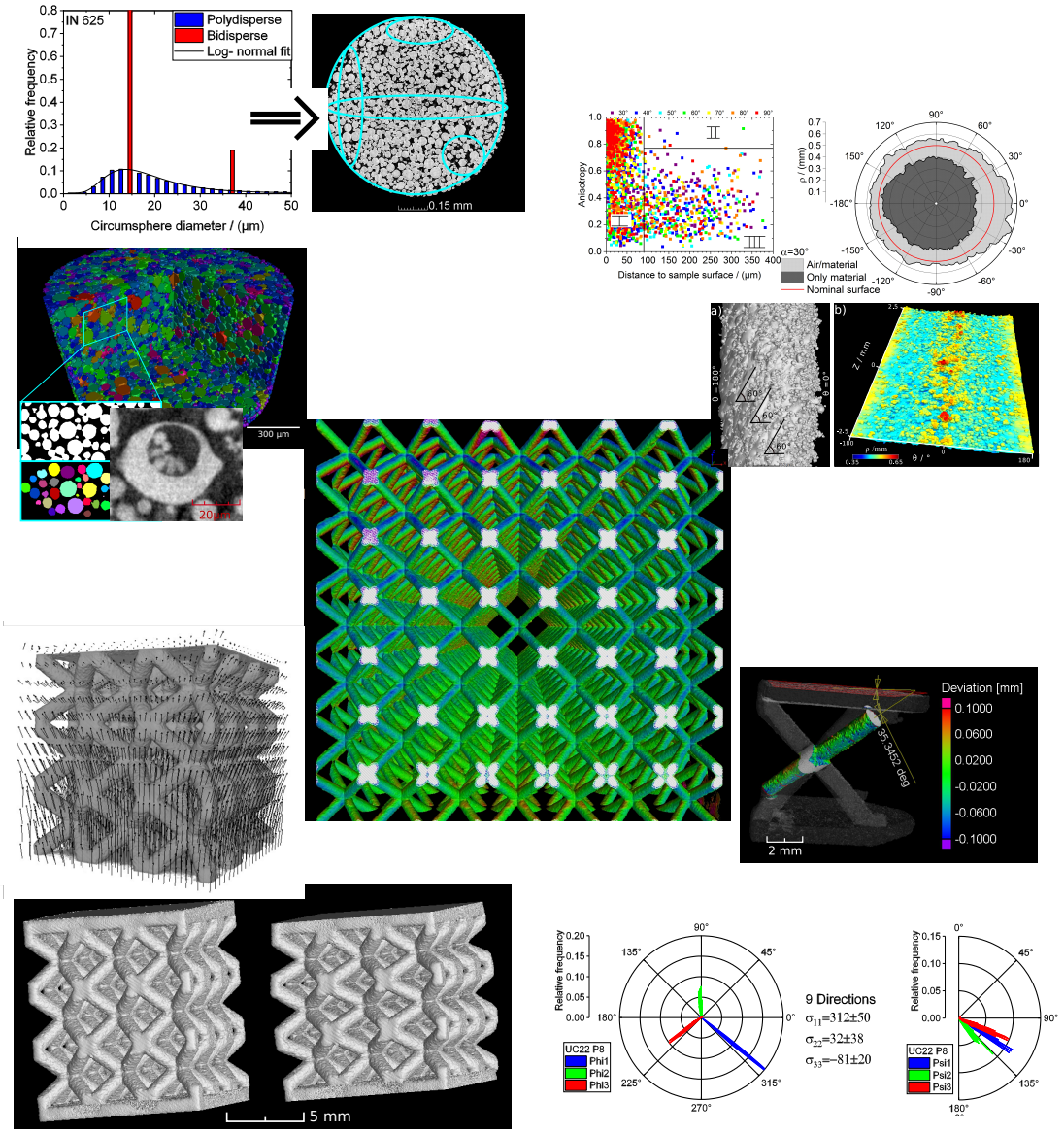

Figure 6.1: The results from the powder, the struts, the unit cell and the $3\times3\times3$ are summarised on the scale of the $7 \times 7 \times 7$ lattice structure. It represents the multiscale quantitative analysis introduced in Figure 1.5

not centred on the base plate. The effect is already reported for the surface topography by Kleszczynski *et al.* [68]. In the case of the influence on RS, a thorough understanding of this effect should be emphasised based on these results together with these of Mishurova *et al.* [101].

The *in-situ* compression computed tomography experiment is evaluated by means of digital volume correlation, see Figure 5.3 and 6.1. The results are in agreement with experiments on larger lattices structures [170].
The nominal-actual comparison is a widely used tool to investigate the geometrical accuracy of a part. However, the lack of references within the manufactured part makes an absolute volume registration impossible. This research investigated the effect of the registration on the results of the nominal-actual comparison.
One problem that is solved within this work is the alignment for a comprehensive neutron diffraction experiment for lattice structures. The alignment is described in section 5.3.1 and should be used in the future for alignments of complex structures.
The principal stress component calculation adopted here is enormously helpful to understand such structures, see Figure 5.11a and 6.1. The following recommendation can be given: one has to determine as many directions as reasonably possible, even though in theory six independent strain measurements should be sufficient. The results show in the present case that at least seven direction are needed to find the correct principal directions. To minimize the error on the principal stress value the three calculated stress direction should also be measured, resulting in a total of ten directions: seven random directions to find the principal directions and three measurements along these principal direction.
The achievements of this work are summarised as following.

- Using high-resolution synchrotron computed tomography, a new analysis workflow was developed to characterise particle porosity, size and shape with an advanced analysis for particle packing density and the inter-particle distance. This goes beyond the work reported in [159].

- The porosity analysis is in agreement with the known pore positions close the surface [15] and advanced this knowledge by the correlation between shape and position

- A workflow for surface characterisation was developed: The recently pub-

lished work by Pagani *et al.* [56] was confirmed and surpassed by a parameter independent of the nominal reference volume to quantify re-entrant features.

- The deformation of lattice structures was understood using *in-situ* computed tomography compression of lattice structure and digital volume correlation: the deformation is knot-dominated and the lattice folds unit cell layer wise.

- A volume registration procedure was established to make the nominal-actual comparison robust also in the case of additive manufacturing

- Residual stresses were non-destructively characterised in lattice structures. This includes the determination of the principal stress directions and magnitudes for the first time

The most important finding of this work is that conventional rules for materials characterisation and non-destructive testing do not necessarily apply for AM materials and even less on AM lattice structures. The new part design and new kind of defects (*e.g.* lack of fusion porosity, attached powder particles, an heterogeneous microstructure, etc.) are still an enormous challenge for existing characterisation methods. To understand all observed features, the data interpretation needs to consider a variety of parameters for AM such as the build angle, the position on the build plate, the layer thickness, the gas flow, the filling of the base plate. While interpreting data on AM materials and structures,

we have to *think additive!*

7 Outlook

The results presented within this thesis can be used in various applications. The powder analysis allows quantifying the effect of powder re-use on 3D shape and size and quantifying how large is the influence on the powder bed quality in terms of packing density and inter-particle distance.
In particular, the correlation between particle size and powder packing density (based on the conversion from poly- to bidisperse particle size distributions) would advance the industrial particle size measurements (*e.g.* sieving and laser diffraction). The evaluation of different types of powder batches with synchrotron computed tomography would allow quantification of this correlation. The characterisation of recycled powder in comparison with the used powder is of high interest as it represents a valuable application of the present results to industrial problems. A large difference in the packing density is expected between virgin and re-used powder.

High resolution computed tomography is a widely used method for non-destructive evaluation of AM parts. The amount of information extractable from a CT-scan could be increased by the correlation between surface topography and microstructure. A quantification of the surface topography as describes in section 4.3 could be used for correlation with the microstructure by means of EBSD or even by diffraction contrast tomography (DCT). Once the correlation is benchmarked, it could be used to distinguish molten material from attached (non-molten) powder particles. In this way, the attached powder particles could be virtually removed from the volume. A mechanical simulation based on CT data would be more realistic, since attached powder particles do not carry any load.
It is commonly accepted that the porosity has an influence on the mechanical behaviour. Together with the detailed surface characterisation, the results of this work could be used to improve fatigue simulations.

The discussion about the *in-situ* compression of the lattice structure could be improved by the knowledge about the stress magnitude within a knot and a strut during the compression. The hypothesis about stress accumulation within the knot could be verified by a compression experiment with *in-situ* neutron diffraction. Based on this work, the principal stress direction would be known and

a stress concentration in a knot under external load could be quantified. This would deepen the understanding of the deformation of the lattice structure under external load and therefore of their safety.
A further suggestion for neutron diffraction experiments is to minimize the d_0 problem by an enforced use of mathematical boundary conditions such as stress balance. Therefore, the L-PBF problems such as anisotropic microstructure and chemical composition variety may be avoided by taking the radial component at each gauge volume as d_0. The idea would allow avoiding extra measurements of sister samples or cubes (prone to reproducibility issue in AM).

Lattice structures are meant to be applied also as cooling channels. Therefore, a flow simulation will be needed. The approach of this thesis overlaps very well the need for such a realistic flow simulation. The combination of a macroscopic CT scan to capture the full geometry plus the high resolution information about the surface topography of each strut should be used as an input for finite element modelling or fluid low simulation.

This work has improved the understanding of defects in additively manufactured lattice structures and introduced new routes of the characterisation for AM samples and parts. The knowledge can be used for safety assurance and could assist in the application to safety-relevant parts.

A Appendix

A.1 Additional Figures

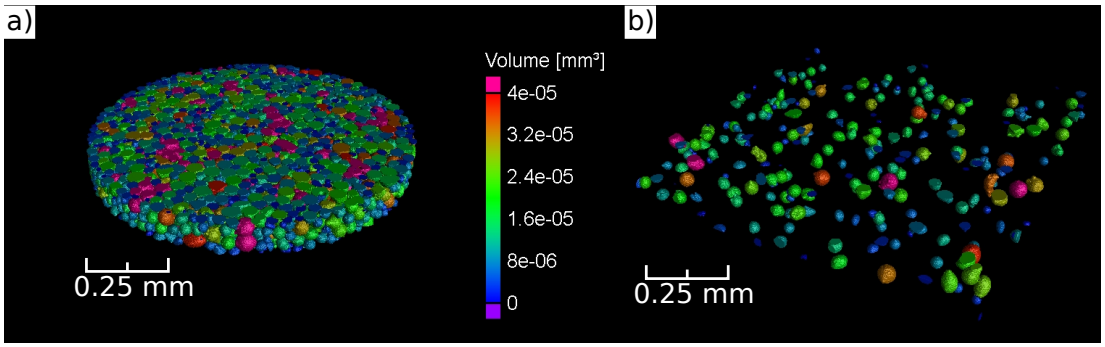

Figure A.1: 3D rendered powder particles in a) glass capillary and in b) epoxy resin

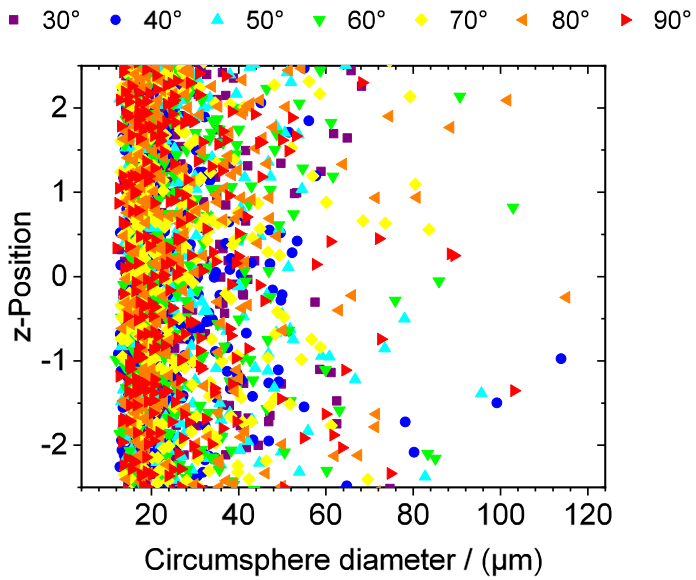

Figure A.2: The pore distribution over the strut height for all struts shows no gradient along the strut height.

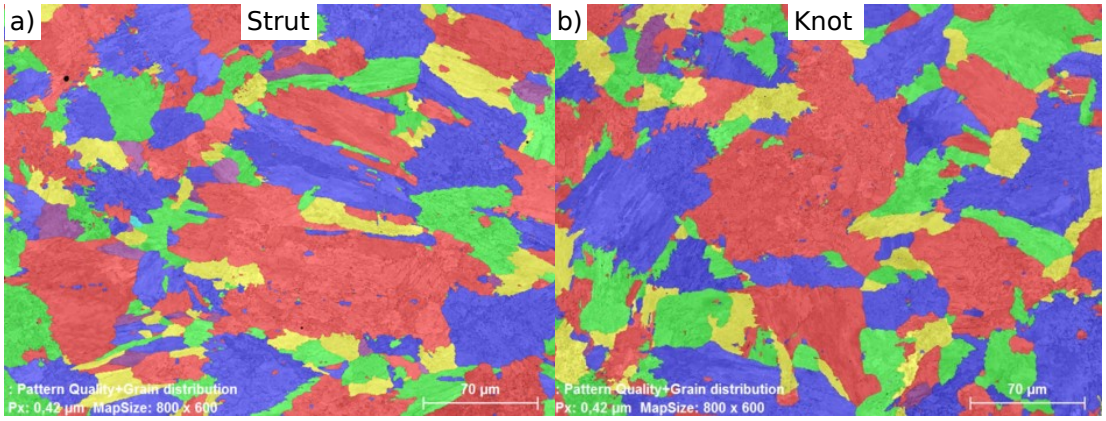

Figure A.3: The microstructure measured by means of EBSD of the single UC for a) a strut position and b) a knot position. The images were acquired by Romero Neumann-Salliwan, BAM, FB 5.2

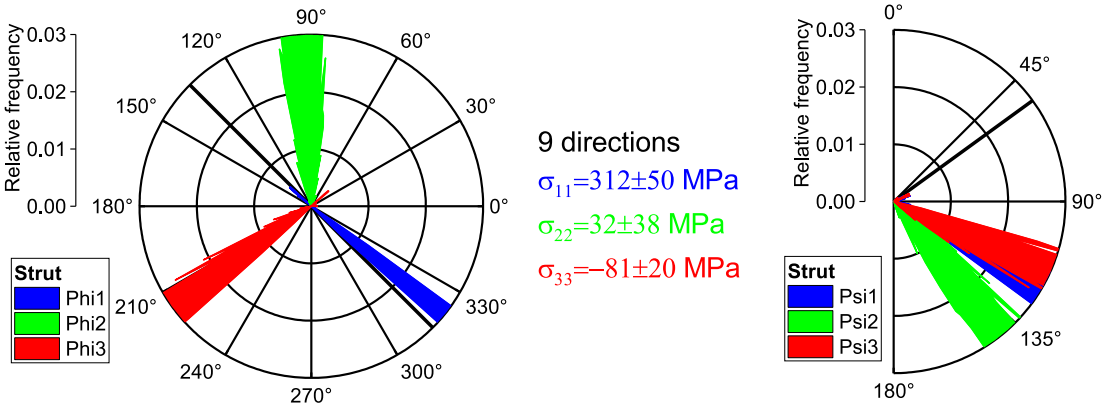

Figure A.4: The results of the principal direction estimation for the strut in the central UC of the $3 \times 3 \times 3$ lattice structure in the sample coordinate system in terms of the eigenvalue σ_{ii} (middle) and the azimuthal phi_i^S (left) and polar ψ_i^S (right) angles of the corresponding eigenvector. This diagram represents the results of Fig. 5.11a on a smaller scale.

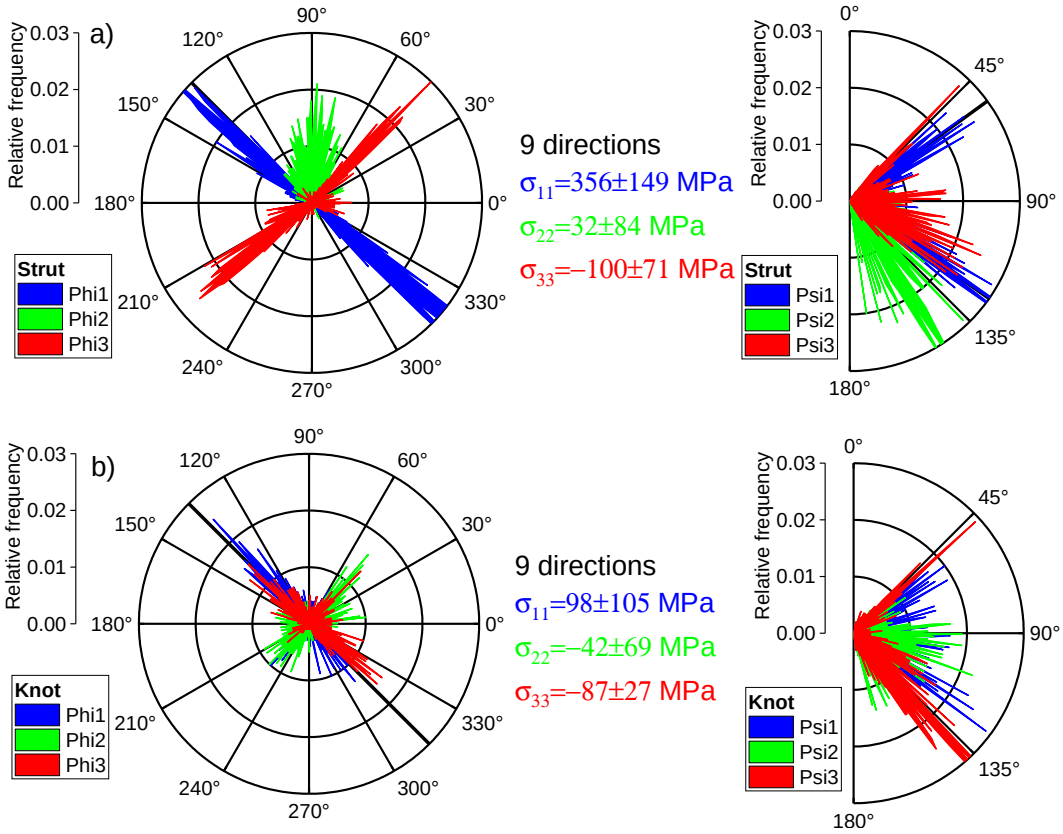

Figure A.5: The results of the principal direction estimation with an artificial measurement error of 500 μstrain for a) the strut and b) the knot in the central UC of the $3\times3\times3$ lattice structure in the sample coordinate system in terms of the eigenvalue σ_{ii} (middle) and the azimuthal phi_i^S (left) and polar ψ_i^S (right) angles of the corresponding eigenvector. The solution is presented for all nine measured directions.

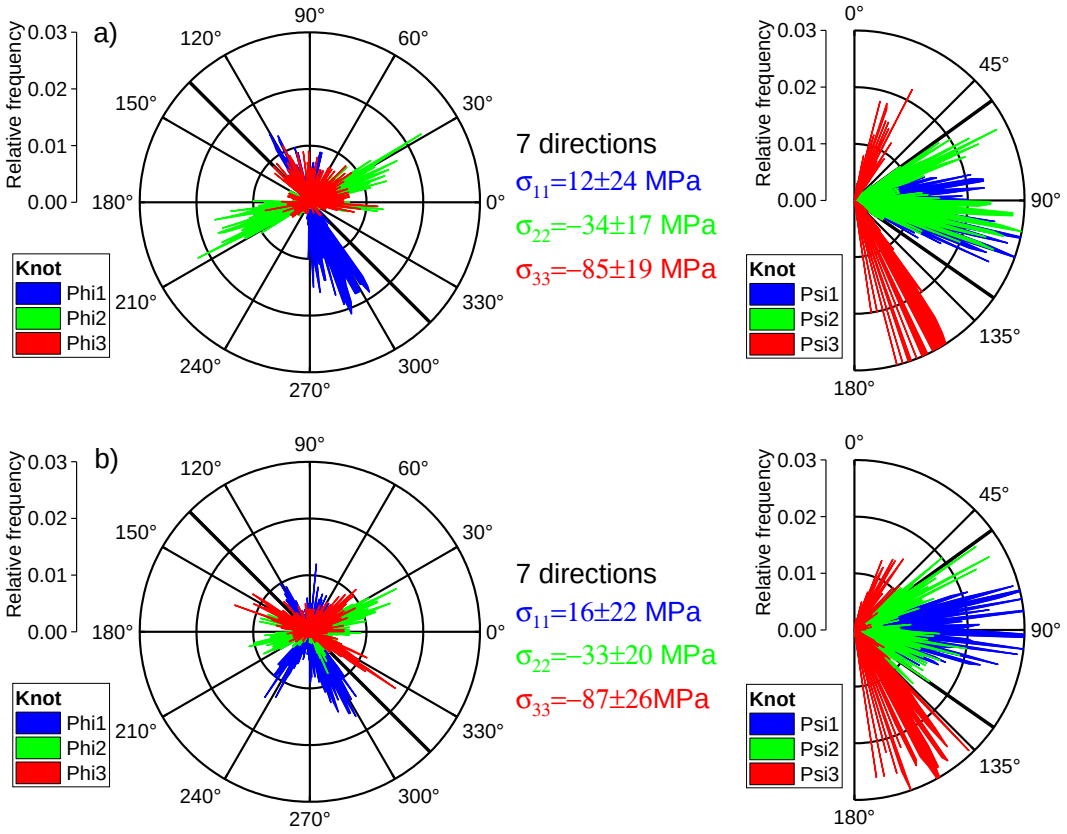

Figure A.6: The results of the principal direction estimation for the knot in the central UC of the $3 \times 3 \times 3$ lattice structure in the sample coordinate system in terms of the eigenvalue σ_{ii} (middle) and the azimuthal phi_i^S (left) and polar ψ_i^S (right) angles of the corresponding eigenvector. The solution is presented for a) the first seven directions from table 5.1 and b) the seven directions with the lowest μstrain value.

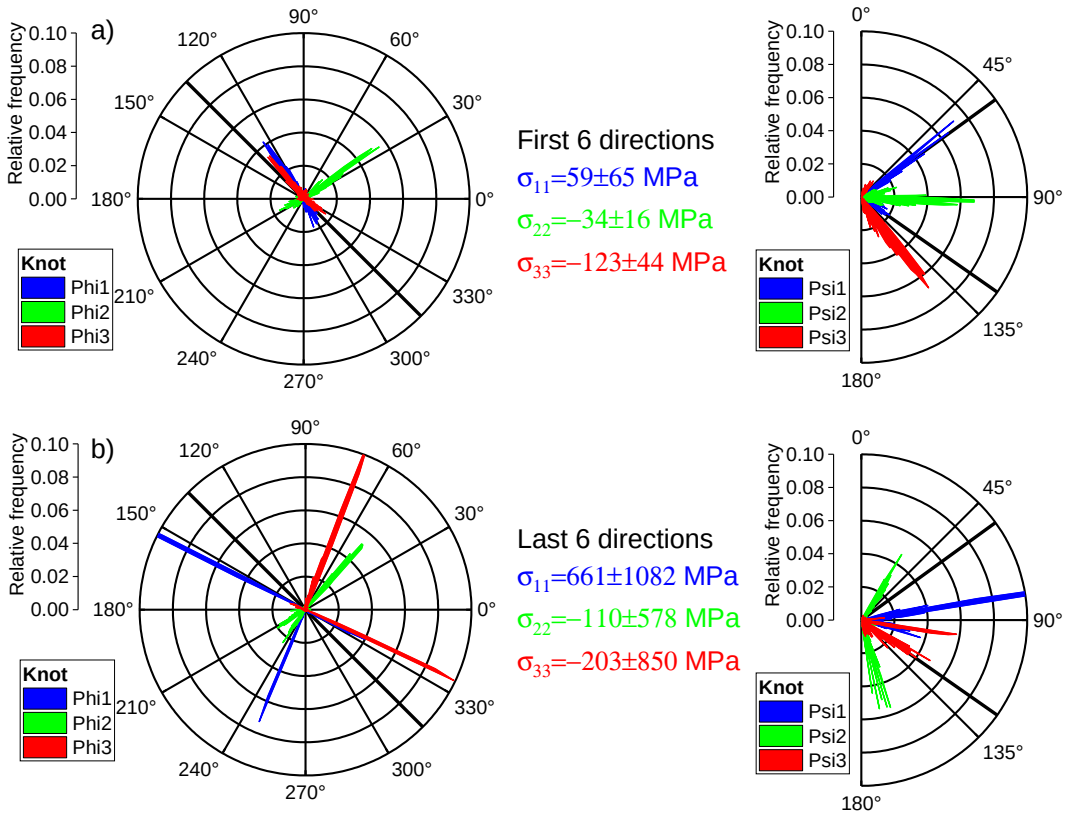

Figure A.7: The results of the principal direction estimation for the knot in the central UC of the $3 \times 3 \times 3$ lattice structure in the sample coordinate system in terms of the eigenvalue σ_{ii} (middle) and the azimuthal phi_i^S (left) and polar ψ_i^S (right) angles of the corresponding eigenvector. The solution is presented for a) the first six and b) the last six directions from table 5.1.

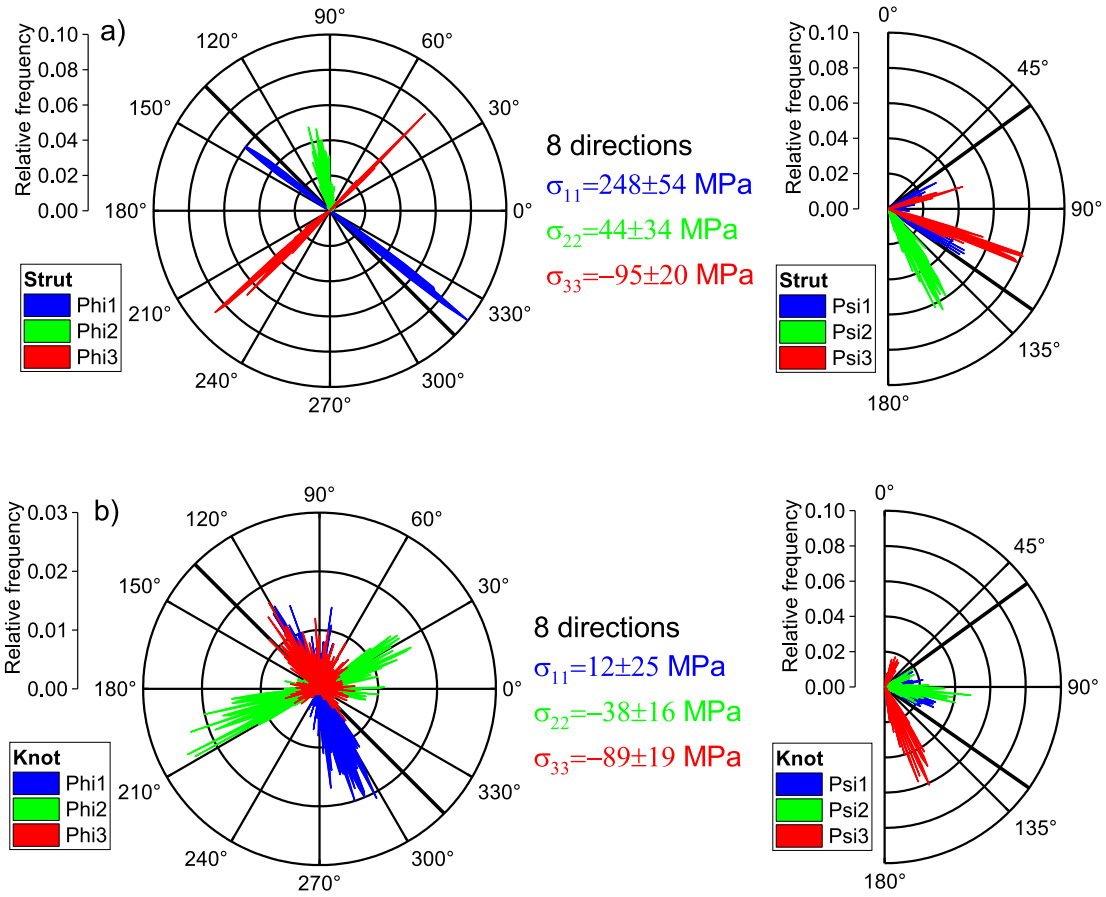

Figure A.8: The results of the principal direction estimation for a) the strut and b) the knot in the central UC of the $3 \times 3 \times 3$ lattice structure in the sample coordinate system in terms of the eigenvalue σ_{ii} (middle) and the azimuthal phi_i^S (left) and polar ψ_i^S (right) angles of the corresponding eigenvector. The solution is presented for the first eight directions from table 5.1.

A.2 Statistically Equivalent Bidisperse Particle Size Distribution

This section is based on the publication by Pednekar *et al.* [164]. They have presented the conversion from polydisperse to statistically equivalent bidisperse distributions. They have formulated three requirements. The mean, the polydispersity, and the skewness of both distributions have to be equal.

$$\bar{d}_{bi} = \bar{d}_{poly} = \mu_{poly} \tag{A.1}$$

$$\alpha_{bi} = \alpha_{poly} = \sqrt{\left(\exp\left(\sigma^2_{poly}\right) - 1\right)\exp\left(2\mu_{poly} + \sigma^2_{poly}\right)} \tag{A.2}$$

$$S_{bi} = S_{poly} = \left(\exp\left(\sigma^2_{poly}\right) + 2\right)\sqrt{\exp\left(\sigma^2_{poly}\right) - 1} \tag{A.3}$$

$$\rho D_L + (1-\rho)D_S = \bar{d}_{bi} \tag{A.4}$$

$$\sqrt{(1-\rho)(D_S-1)^2 + \rho(D_L-1)^2} = \alpha_{bi} \tag{A.5}$$

$$\frac{(1-\rho)(D_S-1)^3 + \rho(D_L-1)^3}{\alpha^3_{poly}} = S_{bi} \tag{A.6}$$

μ_{poly} and σ_{poly} being the known mean and variance from the log-normal fit of the PSD. The relative amount of large particles ρ, the diameter of the small particles D_S, and the diameter of the large particles D_L are the unknown parameters characterising the bidisperse distribution. The results of this conversion are presented in table 3.1 and Figure A.9.

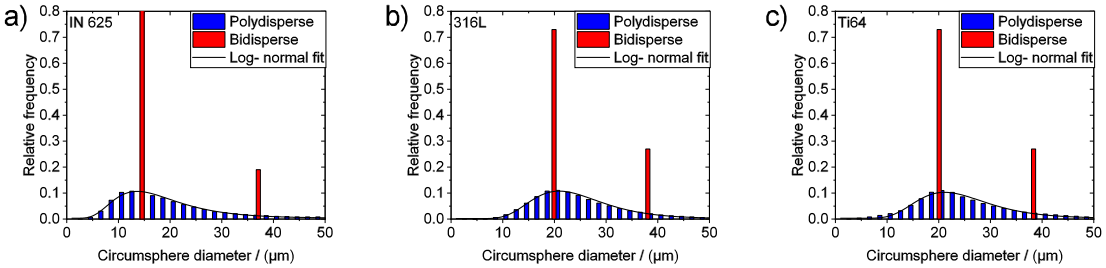

Figure A.9: The measured polydisperse particle size distribution (blue) with its statistically equivalent bidisperse distribution (red) for three powder batches: a) IN 625, b) AISI 316L, and c) Ti64.

A.3 Surface Topography of a NMR Flow Cell

The surface topography is not only important for the outer surface of metal AM parts. Another application for the workflow presented in this thesis is a 3D printed flow cell for gas mixing application. This flow cell is a hollow cylindrical structure with an outer diameter of 6 mm, see Figure A.10a. The surface topography of the inner surface can be non-destructively measured only by means of CT.

Nuclear magnetic resonance (NMR) is used to evaluate the mixture of two gas flows within the cylindrical flow cell. A high surface quality is therefore essential to assure a homogeneous magnetic field in the inside of the cell. Surface roughness and hence a difference in the wall thickness would affect the magnetic field strength. Since the nominal geometry is a cylinder the same script was used for evaluation. A sapphire crystal with the same nominal geometry such as the flow cell was scanned by CT as a reference sample.

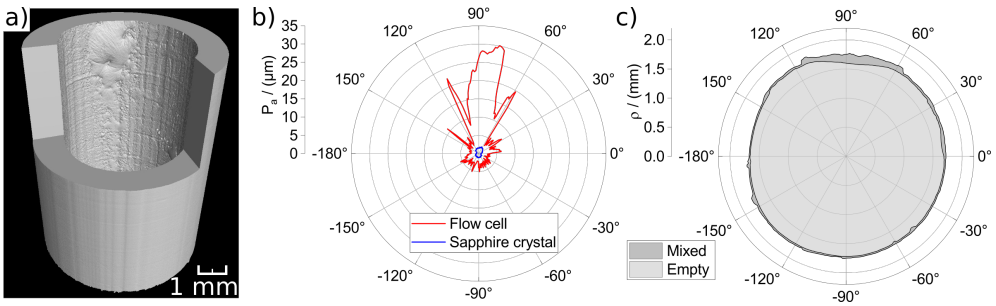

Figure A.10: a) 3D rendered flow cell, b) The surface topography in form of P_a for the flow cell (red) and the sapphire crystal and c) the projected area through the flow cell. Opposite the struts in Figure 4.7f, the light grey area indicates now material will the dark- grey indicates the mixed between material and air voxel.

The results in Figure A.10 show negligible roughness values for the sapphire crystal as it was expected. This proves the algorithm and also the idea of the sapphire crystal as a reference sample for NMR spectroscopy correct.

P_a shows on average values below 5 μm for the flow cell, indicating a good surface quality, see Figure A.10b. An exception is the angular range $60° \leq \theta \leq 115°$. An error during the printing process, see Figure A.10a lead to a reduced surface quality within this interval. P_a and the projected area are complementary for the flow cell, as already shown for the struts. This example depicts the broad application of the workflow as it allows also the quantification of inner surfaces.

A.4 Source Codes

Listing 1: Roughness analysis

```
1  import numpy as np
2  from scipy.optimize import leastsq
3  import os #for path saving
4
5  def cart2pol(a, b):
6  rho = np.sqrt(a**2 + b**2)
7  theta = np.arctan2(b, a)*180/np.pi
8  return(rho, theta)
9
10 def pol2cart(rho, phi):
11 x = rho * np.cos(phi)
12 y = rho * np.sin(phi)
13 return(x, y)
14
15 def rotX (data, angle):
16 rotXmatrix=np.array([[1, 0 , 0 ],
17 [0, np.cos(angle), -np.sin(angle)],
18 [0, np.sin(angle), np.cos(angle)]])
19 data_rot = np.dot(data,rotXmatrix)
20 return data_rot
21
22 def rotY (data, angle):
23 rotYmatrix=np.array([[np.cos(angle) , 0, np.sin(angle)],
24 [ 0 , 1, 0 ],
25 [-np.sin(angle), 0, np.cos(angle)]])
26 data_rot = np.dot(data,rotYmatrix)
27 return data_rot
28
29 def cylinderFitting(data,p,th):
30 x=data[:,0]
31 y=data[:,1]
32 z=data[:,2]
33 fitfunc = lambda p, x, y, z: (- np.cos(p[3])*(p[0] - x) - z*np.
       cos(p[2])*np.sin(p[3]) - np.sin(p[2])*np.sin(p[3])*(p[1] - y
       ))**2 + (z*np.sin(p[2]) - np.cos(p[2])*(p[1] - y))**2 #fit
       function
34 errfunc = lambda p, x, y, z: fitfunc(p, x, y, z) - p[4]**2 #
       error function
```

```
35    est_p , success = leastsq(errfunc, p, args=(x, y, z), maxfev
          =1000)
36    return est_p
37    ###Initialization of variables###
38    strut =[]
39    inner_area=[]
40    outer_area=[]
41    eccentricity=[]
42    inclination_angle=[]
43    for strutnumber in ("21","25","31","35","39","43","47"):
44    print ("Surface_Strut"+strutnumber+".txt")
45    data = np.loadtxt(os.path.join('Surface_Kart/Surface_Strut'+
          strutnumber+".txt"), skiprows=1)
46    data[:,2]=data[:,2]-((np.max(data[:,2])+np.min(data[:,2]))/2) #
          Z-shift to 0
47    p = np.array([0,0,0,0,0.5]) #Initial Fit-Parameter
48    est_p = (cylinderFitting(data,p,0.00001)) #Perform the fitting
49    ###Translation+Rotation###
50    data[:,0]=data[:,0]-est_p[0]
51    data[:,1]=data[:,1]-est_p[1]
52    data=rotX(data,est_p[2])
53    data=rotY(data,est_p[3])
54    X=data[:,0]
55    Y=data[:,1]
56    Z=data[:,2]
57    ###Transformation to cylindrical coordinates###
58    data_CylCor=np.append([cart2pol(X, Y)[1], cart2pol(X, Y)[0]], [
          Z], axis=0)
59    theta=data_CylCor[0,:]
60    rho=data_CylCor[1,:]
61
62    ###Analysis of surface topography###
63    stepwidth=1 #Step width for analysis
64    Ra=[]
65    gamma= []
66    Rmax_min= []
67    Rmin =[]
68    Rmax = []
69    innerArea = 0
70    outerArea = 0
71    for phi in range (-180,180,stepwidth):
```

```
72    interval_rho=rho[np.where(np.logical_and(theta >= (phi-
          stepwidth/2) , theta < (phi+stepwidth/2)))]
73    gamma.append(phi)
74    Ra.append(np.mean(np.abs(interval_rho-np.mean(interval_rho))))
75    Rmax_min.append(np.max(interval_rho)-np.min(interval_rho))
76    Rmin.append(np.min(interval_rho))
77    Rmax.append(np.max(interval_rho))
78    innerArea = innerArea + np.pi*np.min(interval_rho)**2*stepwidth
          /360
79    outerArea = outerArea + np.pi*np.max(interval_rho)**2*stepwidth
          /360
80    table=(np.vstack((gamma, Ra, Rmax_min, Rmin, Rmax))).T
81    np.savetxt(os.path.join('Roughness_analyzed',"Roughness"+
          strutnumber+".txt"), (table), fmt='% -1f, % -4f, % -4f, % -4
          f, % -4f', delimiter=', ', newline='\n', header='theta, R\-(
          a), R\-(max-min), R\-(min), R\-(max) \n degree, mm , mm, mm,
           mm', footer='', comments=' ')
82    strut.append(float(strutnumber))
83    inner_area.append(innerArea)
84    outer_area.append(outerArea)
85    inclination_angle.append(phi)
86    Projected_area = (np.vstack((strut, inner_area, outer_area))).T
87    np.savetxt("Projected_area.txt", (Projected_area), fmt='% -4f,
          % -4f, % -4f', delimiter=', ', newline='\n', header='Strut,
          InnerArea, OuterArea \n , mm^2 ,mm^2 ', footer='', comments
          =' ')
```

Listing 2: Re-entrant surface analysis

```
import numpy as np
from stl import mesh
from scipy.optimize import leastsq
import time
import os #for path saving
from sklearn import preprocessing

def cylinderFitting(data,p,th):
x=(data[:,:,0]).ravel()
y=(data[:,:,1]).ravel()
z=(data[:,:,2]).ravel()
fitfunc = lambda p, x, y, z: (- np.cos(p[3])*(p[0] - x) - z*np.
    cos(p[2])*np.sin(p[3]) - np.sin(p[2])*np.sin(p[3])*(p[1] - y
    ))**2 + (z*np.sin(p[2]) - np.cos(p[2])*(p[1] - y))**2 #fit
    function
errfunc = lambda p, x, y, z: fitfunc(p, x, y, z) - p[4]**2 #
    error function
est_p , success = leastsq(errfunc, p, args=(x, y, z), maxfev
    =1000)
return est_p

def cart2pol(x, y):
rho = np.sqrt(x**2+y**2)
theta = np.arctan2(y, x)*180/np.pi
return(rho, theta)

start_time = time.time()
strut, InnerSurface =[], []
for strutnumber in ("21", "25", "31", "35", "39", "43", "47"):
print ("Surface_Strut"+strutnumber+".stl")
surface=mesh.Mesh.from_file(os.path.join('Surface_Kart','S'+
    strutnumber+'.stl')) #import stl-file
volume, cog, inertia = surface.get_mass_properties()
#Aligne the strut to cylinder
p = np.array([0,0,0,0,0.5]) #Initial Fit-Parameter
est_p = (cylinderFitting(surface.vectors,p,0.00001)) #Perform
    the fitting
print ('Estimated Parameters:\n',est_p)
#correct surface by fitted cylinder
surface.x -= est_p[0]
```

```
34  surface.y -= est_p[1]
35  surface.rotate([0.5,0.0,0.0], est_p[2])
36  surface.rotate([0.0,0.5,0.0], est_p[3])
37  surface.z -= cog[2]
38  #calculate the center of gravity for each vertex and convert
        cog in rho/phi
39  x_cog, y_cog, z_cog, = [], [], [],
40  for i in range (0,surface.vectors.shape[0]):
41  x_cog.append((surface.vectors[i,:,0]).sum()/3)
42  y_cog.append((surface.vectors[i,:,1]).sum()/3)
43  z_cog.append((surface.vectors[i,:,2]).sum()/3)
44  cog=np.vstack((x_cog,y_cog,z_cog)).T
45  z_index1, z_index2=np.where(np.abs(cog[:,2])>2.5), np.where(np.
        abs(cog[:,2])<=2.5) #find index of the close-to-edge
        vertices
46  cog=np.delete(cog,z_index1,axis=0) #delete close-to-edge
        vertices from cog-array
47  rho,theta=cart2pol(cog[:,0],cog[:,1])
48  #calculated the rho component of the normal vector at the
        position of the triangle-cog without close-to-edge vertices
49  rho_component=preprocessing.normalize(surface.normals,norm='l2'
        )[z_index2[0],0]*np.cos(theta*np.pi/180)+preprocessing.
        normalize(surface.normals,norm='l2')[z_index2[0],1]*np.sin(
        theta*np.pi/180)
50  surfacearea=surface.areas[z_index2[0]]
51  #line-wise analyse of the surface pointing towards negative rho
52  stepwidth, gamma, relative_inner_surface,
        line_wise_inner_surface =1, [], [], []
53  for phi in range (-180,180,stepwidth):
54  rho_component_phi=rho_component[np.where(np.logical_and(theta
        >= (phi-stepwidth/2) , theta < (phi+stepwidth/2)))]
55  surfaceareas_phi=surfacearea[np.where(np.logical_and(theta >= (
        phi-stepwidth/2) , theta < (phi+stepwidth/2)))]
56  relative_inner_surface.append(100*np.sum(surfaceareas_phi[np.
        where(rho_component_phi<0)])/np.sum(surfacearea))
57  line_wise_inner_surface.append(100*np.sum(surfaceareas_phi[np.
        where(rho_component_phi<0)])/np.sum(surfaceareas_phi))
58  gamma.append(phi)
59  #export the relative surface for each strut and angle
60  table1=(np.vstack((gamma, relative_inner_surface,
        line_wise_inner_surface))).T
61  np.savetxt(os.path.join('Roughness_analyzed','InnerSurface'+
```

```
        strutnumber+'.txt'), (table1), fmt='%-1f, %-4f, %-4f',
        delimiter=', ', newline='\n', header='theta, relative to
        strut-surface, relative to line-surface \n degree, % , %',
        footer='', comments=' ')
62      strut.append(float(strutnumber))
63      InnerSurface.append(np.sum(surfacearea[np.where(rho_component
        <0)])/np.sum(surfacearea))
64      #export the total relative surface for each strut
65      table2 = (np.vstack((strut, InnerSurface))).T
66      np.savetxt("InnerSurface.txt", (table2), fmt='%-1f, %-4f',
        delimiter=', ', newline='\n', header='Strut, InnerSurface',
        footer='', comments=' ')
```

Listing 3: Principal stress directions

```
from __future__ import division
import numpy as np
import time
import math
import sys

start_time = time.time()
np.set_printoptions(threshold=sys.maxsize)
for j in range (1,1001): #loop for error statistics
Emodul_IN625=193800 #Inout for stress calculation
Poission_IN625=0.305
###FOR MANUAL INPUT- strain value in micro strain###
name="UC22_P8_strut_9compontents"
tths=84
omgs=np.array([42,42,42,42,42,42,42,42,42])
chis=np.array([0,0,90,35,125,70,50,80,15])
phis=np.array([0,90,0,45,45,30,60,0,80])
Meas_Strain=np.array([246,17,323,-730,80,-449,-508,0,106])
Strain_error=np.array([142,170,123,132,112,160,220,164,112])
N=len(Meas_Strain)
###Conversion from Laboratory System to Sample System###
phi=(omgs-tths/2+phis)*np.pi/180
theta=(90-chis)*np.pi/180
###Determine a strain value within the error range ###
Strain=[]
for i in range (0,N):
Strain.append(np.random.uniform(Meas_Strain[i]-Strain_error[i],
Meas_Strain[i]+Strain_error[i]))
###create cosin matrix###
for i in range (0, N):
if i==0: #define the array in the first loop
Meas_Dir = np.array([np.cos(phi[i])**2*np.sin(theta[i])**2,
np.sin(2*phi[i])*np.sin(theta[i])**2,
np.cos(phi[i])*np.sin(2*theta[i]),
np.sin(phi[i])**2*np.sin(theta[i])**2,
np.sin(phi[i])*np.sin(2*theta[i]),
np.cos(theta[i])**2 ])
else: #fill the array in the following loops
a=np.array([np.cos(phi[i])**2*np.sin(theta[i])**2,
np.sin(2*phi[i])*np.sin(theta[i])**2,
```

```
41    np.cos(phi[i])*np.sin(2*theta[i]),
42    np.sin(phi[i])**2*np.sin(theta[i])**2,
43    np.sin(phi[i])*np.sin(2*theta[i]),
44    np.cos(theta[i])**2 ])
45    Meas_Dir=np.vstack((Meas_Dir,a))
46    ###solve linear Equation System of cosines and strain values###
47    eps,res,rank,s= np.linalg.lstsq(Meas_Dir, Strain)
48    eps_11,eps_12,eps_13,eps_22,eps_23,eps_33=eps[0],eps[1],eps[2],
49    eps[3],eps[4],eps[5],
50    ###Fill the strain tensor with the solutions###
51    Strain_Tensor=[[eps_11,eps_12,eps_13],
52    [eps_12,eps_22,eps_23],
53    [eps_13,eps_23,eps_33]]
54    ###Extract and order Eigenvalues and Eigenvectors###
55    e,v=np.linalg.eig(Strain_Tensor) #extraction of eigenvalues and
          -vectors
56    sortingIndizes=e.argsort() #Order e according to size
57    e = e[sortingIndizes[::-1]]
58    if j==1:
59    eigval=e
60    else:
61    eigval=np.vstack((eigval,e))
62    eigval=np.around(eigval,2)
63    v[:,2]=np.cross(v[:,0],v[:,1]) #vector product needed for right
         -hand rule
64    v=(np.vstack((v[:,sortingIndizes[2]],
65    v[:,sortingIndizes[1]],
66    v[:,sortingIndizes[0]]))).T #Order v according to e
67    v=np.around(v,2) #round the eigenvector to 2 digits
68    ###Calculate Polar and Azimuth Angle for the three Eigenvectors
         ###
69    for i in (1,2,3):
70    a=180/np.pi*math.atan2(v[1,i-1], v[0,i-1])     #azimuth-angle
71    b=180/np.pi*np.arccos(v[2,i-1])                 #polar-angle
72    if j==1:
73    if i==1:
74    phitheta=np.hstack((a,b))
75    else:
76    phitheta=np.hstack((phitheta,a,b))
77    else:
78    if i==1:
79    phitheta_line=np.hstack((a,b))
```

```
80      else:
81      phitheta_line=np.hstack((phitheta_line,a,b))
82      if i==3:
83      phitheta=np.vstack((phitheta,phitheta_line))
84      phitheta=np.around(phitheta,2)
85      ###Output###
86      print (name)
87      epsilon11,epsilon22,epsilon33=eigval[:,0]/10**6,
88      eigval[:,1]/10**6, eigval[:,2]/10**6
89      sigma11=Emodul_IN625/((1+Poission_IN625)*(1-2*Poission_IN625))
            *((1-Poission_IN625)*epsilon11+Poission_IN
90      625*(epsilon22+epsilon33))
91      sigma22=Emodul_IN625/((1+Poission_IN625)*(1-2*Poission_IN625))
            *((1-Poission_IN625)*epsilon22+Poission_IN625*(epsilon11+
            epsilon33))
92      sigma33=Emodul_IN625/((1+Poission_IN625)*(1-2*Poission_IN625))
            *((1-Poission_IN625)*epsilon33+Poission_IN625*(epsilon22+
            epsilon11))
93      print ('Sigma11=',np.mean(sigma11),'+-',np.std(sigma11))
94      print ('Sigma22=',np.mean(sigma22),'+-',np.std(sigma22))
95      print ('Sigma33=',np.mean(sigma33),'+-',np.std(sigma33))
96      stress=np.vstack((sigma11,sigma22,sigma33)).T
97      np.savetxt(name+"_Stress.txt", (stress),fmt='% 1.2f, % 1.2f, %
            1.2f',delimiter=', ',newline='\n',header='EigVal_1, EigVal_2
            , EigVal_3',footer='', comments=' ')
98      np.savetxt(name+"_EigenAngles.txt", (phitheta),fmt='% 1.2f, %
            1.2f, % 1.2f,% 1.2f, % 1.2f, % 1.2f',delimiter=', ', newline
            ='\n',header='Phi_1,Psi_1, Phi_2,Psi_2, Phi_3,Psi_3 ',footer
            ='',comments=' ')
99      print("Finished after %s seconds" % (time.time() - start_time))
```

A.5 Lists of Figures and Tables

List of Figures

List of Tables

A.6 List of Publications

J. Kurpiers, T. Ferron, S. Roland, M. Jakoby, T. Thiede, F. Jaiser, S. Albrecht, S. Janietz, B. A. Collins, I. A. Howard, and D. Neher: *Probing the pathways of free charge generation in organic bulk heterojunction solar cells*, in Nat. Comm. **9** (2018), doi:10.1038/s41467-018-04386-3

N. Nadammal, S. Cabeza, T. Mishurova, T. Thiede, A. Kromm, C. Seyfert, L. Farahbod, C. Haberland, J. A. Schneider, P. D. Portella, and G. Bruno: *Effect of hatch length on the development of microstructure, texture and residual stresses in selective laser melted superalloy Inconel 718*, in Material & Design **134**, (2017), doi: https://doi.org/10.1016/j.matdes.2017.08.049

T. Thiede, S. Cabeza, T. Mishurova, N. Nadammal, A. Kromm, J. Bode, C. Haberland, and G. Bruno: *Residual Stress in Selective Laser Melted Inconel 718: Influence of the Removal from Base Plate and Deposition Hatch Length*, in Mat. Perf. and Char. **7** (2018), doi: https://doi.org/10.1520/MPC20170119

T. Mishurova, S. Cabeza, T. Thiede, N. Nadammal, A. Kromm, M. Klaus, C. Genzel, C. Haberland, and G. Bruno: *The Influence of the Support Structure on Residual Stress and Distortion in SLM Inconel 718 Parts*, in Metallurgical and Mat. Trans. A **49** (2018), doi: https://doi.org/10.1007/s11661-018-4653-9

T. Thiede, T. Mishurova, S. Evsevleev, I. Serrano-Munoz, C. Gollwitzer, and G. Bruno: *3D Shape Analysis of Powder for Laser Beam Melting by Synchrotron X-ray CT*, in Quantum Beam Sci. **3** (2018), doi: https://doi.org/10.3390/qubs3010003

M. Bornemann, S. Kern, N. Jurtz, T. Thiede, M. Kraume, and M. Maiwald: *Design and Validation of an Additively Manufactured Flow Cell–Static Mixer Combination for Inline NMR Spectroscopy*, in Ind. Eng. Chem. Res. **58** (2019), doi: https://doi.org/10.1021/acs.iecr.9b03746

A. Ulbricht, C. Gollwitzer, A. Kupsch, F. Léonard, B. R. Müller, T. Oesch, Y. Onel, T. Thiede, and U. Zscherpel: *Moderne Methoden der Quantitativen 3D Bildanalyse*, submitted to Technisches Messen, **86**, Indus. CT (2019) (under review)

T. Thiede, Lena Farahbod-Sternahl, I. Serrano-Munoz, F. Léonard, C. Haberland, and G. Bruno: *Additively manufactured IN625 struts at the microscale: comprehensive understanding of surface roughness and bulk porosity* submitted to Journal of Materials Research and Technology (2019), (under review)

A.7 List of Attended Conferences

HERCULES School, **2017** in Grenoble, France, Poster presentation: *Residual Stress Analysis of Selective Laser Melting of IN 718*

DVM, **2017** in Berlin Germany, Oral presentation and conference paper, JuniorPrize: *Der Einfluss der Hatch-Länge und der Probenabtrennung von der Bauplatte auf den Eigenspannungszustand in SLM-Bauteilen aus IN718*

iCT, **2018** in Wels, Austria, Poster presentation: *In-situ compression CT on additively manufactured IN 625 lattice structures*

InnoTesting, **2018** in Wildau, Germany, Oral presentation: *Computed Tomography of SLM Produced IN625 Parts: From Powder Grains to Lattice Structures*

BAM PhD-Day, **2018** in Berlin, Germany, Poster presentation, Poster Prize: *In-situ compression CT on additively manufactured IN 625 lattice structures*

ECNDT, **2018** in Gothenburg, Sweden, Oral presentation and reviewed conference paper: *An assessment of bulk residual stress in selective laser melted Inconel 718*

DVI Expertenforum, **2018** in Munich, Germany, Oral presentation, Invited speaker: *Computed tomography of SLM produced IN625 parts: From powder grains to lattice structures*

HZB User-Meeting, **2018** in Berlin, Germany, Oral presentation, Invited speaker: *An assessment of bulk residual stress in selective laser melted Inconel 718*

iCT, **2019** in Padua, Italy, Poster presentation: *μCT Surface Analysis of LBM Struts - Influence of the Build Angle*

Hannover Messe, **2019**, Representing Additive Manufacturing at the BAM-booth

A.8 Acknowledgement

I can barely express how thankful I am for the support, the motivation, and the guidance I received from Prof. Dr. Giovanni Bruno. He took the German term 'Doktor**vater**' incredible seriously and taught and guided me in both, science and live. His frenetic optimism in any discussion always spurred me on.
A constantly well established atmosphere of teamwork and constructivism within the whole team 8.5 made me feel acknowledged and led me to this thesis. Even though I am not able to mention everyone, I would like to highlight very fruitful discussions during lunch-breaks and beam-times with Tatiana, Sergei, Fabien, Yevgenia, Itziar, Alex., Alex, Maximilian and Christian. I felt blessed to benefit from the long experience in CT of Dietmar and Bernhard. An additional thanks goes to Alex and Fabien for reading the first draft of this manuscript.
I always looked forward to the next beamtime at the EDDI beamline because my second supervisor Prof. Dr. Christoph Genzel created intrinsically an atmosphere of teaching and scientific work together with his colleague and beamline scientist Dr. Manuela Klaus that I highly acknowledged.
The whole research project would not have been possible without the collaboration with Siemens AG, Gas and Power, in Persons of Lena Farahbod-Sternahl and Dr. Christoph Haberland. The discussions helped me tremendously to understand the manufacturing process itself, and the close contact enabled fast support for any question and query. I feel thankful to Dr. Sandra Cabeza together with Lena and Giovanni for the initiation of this successful collaboration.
The experiments at the neutron reactors BER II and FRM II were possible only thanks to the beamline scientist at E3, Dr. Robert Wimpory and Dr. Mirko Boin, and the beamline scientist at Stress-Spec Dr. Michael Hofmann with his team. I acknowledge the openness to questions even long time after a beamtime.
During my stay at BAM, I experienced a strong support from many colleagues: Mr. Lehmann and Mr. Fröse (FB 9.2), Mr. Löwe (FB 5.2), Mr. Salliwan-Neumann (FB 5.1), and Mrs. Kirstein (FB 9.3). One highlight was the spontaneous and fruitful collaboration with FB 1.3, in particular Martin Bornemann.
I received helpful support by Thermo Fischer in persons of Dr. Staude and Mr. Westenberger who explained me patiently the DVC algorithm.
Finally, I appreciate the gorgeous motivation and support that I received from my fiancée, together with her understanding of nights of writing and long absences for experiments and conferences.

A.9 Thesis Declaration

I, Tobias Thiede, hereby declare that the work presented in this thesis has not been submitted to any other university or higher education institute and that this work is my own and that all sources, aids, and supports used are listed within. Any results not of my own creation are clearly indicated as such.

Place/Date	Tobias Thiede

References

[1] S. Hickey. *Chuck Hull: the father of 3D printing who shaped technology*. Access: 10.04.2019. June 2014. URL: https://www.theguardian.com/business/2014/jun/22/chuck-hull-father-3d-printing-shaped-technology.

[2] J.F.Isaza and C. Aumund-Kopp. "Additive Manufacturing with metal powders: Design for Manufacture evolves into Design for Function". In: *Powder Metallurgy Review* 3 (2014), pp. 41–51.

[3] R. Bogue. "3D printing: the dawn of a new era in manufacturing?" In: *Assembly Automation* 33.4 (2013), pp. 307–311. DOI: 10.1108/AA-06-2013-055.

[4] R. A. of Engineering. *Additive manufacturing: Opportunities and constraints*. Report. Royal Academy of Engineering, 2013.

[5] J. Gausemeier, N. Echterhoff and M. Wall. "Thinking ahead the future of additive manufacturing: Innovation roadmapping of required advancements". In: *DMRC - Direct Manufacturing Research Center* (2013).

[6] I. Gibson, D. Rosen and B. Stucker. *Additive Manufacturing Technologies*. 3D Printing, Rapid Prototyping, and Direct Digital Manufacturing. Springer, 2015.

[7] T. Wohlers. *Additive manufacturing and 3D printing state of the industry*. Report. 2013.

[8] J. Kranz, D. Herzog and C. Emmelmann. "Design for manufacturing approach for laser additive manufactured bionic lightweight structures in TiAl6V4". In: *User's Conference for Rapid Technology*. (Erfurt, Germany). Rapid. Tech, May 2014, pp. 1–11. ISBN: 978-3-932875-36-6.

[9] *Siemens sets innovation milestone with first 3D-printed parts for industrial steam turbine*. Access: 01.09.2019. Apr. 2018. URL: https://www.siemens.com/press/en/feature/2018/powergenerationservices/2018-04-3d-parts.php?content=PS.

[10] S. Hyde and A. Okninski. "Additive Manufacturing Design Optimised Bipropellant Injector". In: (Rom, Italy). Space Propulsion 2016. May 2016.

[11] E. Wycisk et al. “Fatigue Performance of Laser Additive Manufactured Ti–6Al–4V in Very High Cycle Fatigue Regime up to 109 Cycles”. In: *Frontiers in Materials* 2 (2015), p. 72. DOI: 10.3389/fmats.2015.00072.

[12] M. R. Alkahari et al. “Thermal Conductivity of Metal Powder and Consolidated Material Fabricated via Selective Laser Melting”. In: *Key Engineering Materials* 523-524 (2012), pp. 244–249. DOI: 10.4028/www.scientific.net/KEM.523-524.244.

[13] A. B. Spierings et al. “Powder flowability characterisation methodology for powder-bed-based metal additive manufacturing”. In: *Progress in Additive Manufacturing* 1.1-2 (2015), pp. 9–20. DOI: 10.1007/s40964-015-0001-4.

[14] R. Baitimerov et al. “Influence of Powder Characteristics on Processability of AlSi12 Alloy Fabricated by Selective Laser Melting”. In: *Materials (Basel)* 11.5 (2018). DOI: 10.3390/ma11050742.

[15] S. Tammas-Williams et al. “XCT analysis of the influence of melt strategies on defect population in Ti–6Al–4V components manufactured by Selective Electron Beam Melting”. In: *Materials Characterization* 102.Supplement C (2015), pp. 47–61. ISSN: 1044-5803. DOI: https://doi.org/10.1016/j.matchar.2015.02.008.

[16] G. Jacob, C. U. Brown and A. Donmez. “The Influence of Spreading Metal Powders with Different Particle Size Distributions on the Powder Bed Density in Laser-Based Powder Bed Fusion Processes”. In: *Advanced Manufacturing Series (NIST AMS)* 100-17 (2018). DOI: 10.6028/nist.Ams.100-17.

[17] M. J. Heiden et al. “Evolution of 316L stainless steel feedstock due to laser powder bed fusion process”. In: *Additive Manufacturing* 25 (2019), pp. 84–103. DOI: https://doi.org/10.1016/j.addma.2018.10.019.

[18] H. Mühlenweg and E. D. Hirleman. “Laser Diffraction Spectroscopy: Influence of Particle Shape and a Shape Adaptation Technique”. In: *Particle and Particle Systems Characterization* 15.4 (1998), pp. 163–169. ISSN: 0934-0866. DOI: 10.1002/(SICI)1521-4117(199808)15:4<163::AID-PPSC163>3.0.CO;2-8.

[19] M. Simonelli, Y. Y. Tse and C. Tuck. "Effect of the build orientation on the mechanical properties and fracture modes of SLM Ti–6Al–4V". In: *Materials Science and Engineering: A* 616.Supplement C (2014), pp. 1–11. ISSN: 0921-5093. DOI: https://doi.org/10.1016/j.msea.2014.07.086.

[20] S. T. Erdoğan, E. J. Garboczi and D. W. Fowler. "Shape and size of microfine aggregates: X-ray micro computed tomography vs. laser diffraction". In: *Powder Technology* 177.2 (2007), pp. 53–63. DOI: 10.1016/j.powtec.2007.02.016.

[21] E. J. Garboczi and J. W. Bullard. "3D analytical mathematical models of random star-shape particles via a combination of X-ray computed micro tomography and spherical harmonic analysis". In: *Advanced Powder Technology* 28.2 (2017), pp. 325–339. DOI: 10.1016/j.apt.2016.10.014.

[22] A. Jillavenkatesa, S. Dapkunas and L. Lum. "NIST Recommended Practice Guide - Particle size Characterization". In: *National Institute of Standards and Technology* (2001, Washington, USA).

[23] A. Strondl et al. "Characterization and Control of Powder Properties for Additive Manufacturing". In: *Jom* 67.3 (2015), pp. 549–554. DOI: 10.1007/s11837-015-1304-0.

[24] J. A. Slotwinski et al. "Characterization of Metal Powders Used for Additive Manufacturing". In: *J Res Natl Inst Stand Technol* 119 (2014), pp. 460–93. DOI: 10.6028/jres.119.018.

[25] Q. B. Nguyen et al. "Characteristics of Inconel Powders for Powder-Bed Additive Manufacturing". In: *Engineering* 3.5 (2017), pp. 695–700. DOI: https://doi.org/10.1016/J.ENG.2017.05.012.

[26] C. Pleass and S. Jothi. "Influence of powder characteristics and additive manufacturing process parameters on the microstructure and mechanical behaviour of Inconel 625 fabricated by Selective Laser Melting". In: *Additive Manufacturing* 24 (2018), pp. 419–431. ISSN: 2214-8604. DOI: https://doi.org/10.1016/j.addma.2018.09.023.

[27] B. Zhou et al. "A study of the microstructures and mechanical properties of Ti6Al4V fabricated by SLM under vacuum". In: *Materials Science and Engineering: A* 724 (2018), pp. 1–10. ISSN: 0921-5093. DOI: https://doi.org/10.1016/j.msea.2018.03.021.

[28] D. J. Brown and G. T. Vickers. "The use of projected area distribution functions in particle shape measurement". In: *Powder Technology* 98.3 (1998), pp. 250–257. ISSN: 0032-5910. DOI: https://doi.org/10.1016/S0032-5910(98)00066-7.

[29] K. Heim et al. "High resolution pore size analysis in metallic powders by X-ray tomography". In: *Case Studies in Nondestructive Testing and Evaluation* 6 (2016), pp. 45–52. DOI: 10.1016/j.csndt.2016.09.002.

[30] J. Zielinski et al. "Influence of Powder Bed Characteristics on Material Quality in Additive Manufacturing". In: *BHM Berg- und Hüttenmännische Monatshefte* 162.5 (2017), pp. 192–198. DOI: 10.1007/s00501-017-0592-9.

[31] G. Chen et al. "A comparative study of Ti-6Al-4V powders for additive manufacturing by gas atomization, plasma rotating electrode process and plasma atomization". In: *Powder Technology* 333 (2018), pp. 38–46. ISSN: 00325910. DOI: 10.1016/j.powtec.2018.04.013.

[32] M. Zheng et al. "A novel method for the molten pool and porosity formation modelling in selective laser melting". In: *International Journal of Heat and Mass Transfer* 140 (2019), pp. 1091–1105. DOI: https://doi.org/10.1016/j.ijheatmasstransfer.2019.06.038.

[33] B. Liu et al. "Investigation the effect of particle size distribution on processing parameters optimisation in selective laser melting process". In: (Austin, TX, USA). Proceedings of Solid Freeform Fabrication Symposium, Aug. 2011.

[34] N. T. Aboulkhair et al. "Reducing porosity in AlSi10Mg parts processed by selective laser melting". In: *Additive Manufacturing* 1-4 (2014), pp. 77–86. ISSN: 2214-8604. DOI: https://doi.org/10.1016/j.addma.2014.08.001.

[35] H. Shipley et al. "Optimisation of process parameters to address fundamental challenges during selective laser melting of Ti-6Al-4V: A review". In: *International Journal of Machine Tools and Manufacture* 128 (2018), pp. 1–20. ISSN: 0890-6955. DOI: https://doi.org/10.1016/j.ijmachtools.2018.01.003.

[36] D. Bernard et al. "First direct 3D visualisation of microstructural evolutions during sintering through X-ray computed microtomography". In: *Acta Materialia* 53.1 (2005), pp. 121 –128. DOI: https://doi.org/10.1016/j.actamat.2004.09.027.

[37] I. Lima et al. "Characterization of titanium implant through Micro CT". In: *Nuclear Instruments and Methods in Physics Research Section A: Accelerators, Spectrometers, Detectors and Associated Equipment* 579 (2007), pp. 309 –312. DOI: https://doi.org/10.1016/j.nima.2007.04.067.

[38] A. Townsend et al. "Areal surface texture data extraction from X-ray computed tomography reconstructions of metal additively manufactured parts". In: (2016). DOI: 10.1016/j.precisioneng.2016.12.008.

[39] A. Thompson et al. "Measurement of internal surfaces of additively manufactured parts by X-ray computed tomography". In: *7th Conference on Industrial Computed Tomography* (2017).

[40] M. Suard et al. "Mechanical equivalent diameter of single struts for the stiffness prediction of lattice structures produced by Electron Beam Melting". In: *Additive Manufacturing* 8.Supplement C (2015), pp. 124–131. ISSN: 2214-8604. DOI: https://doi.org/10.1016/j.addma.2015.10.002.

[41] I. Maskery et al. "Quantification and characterisation of porosity in selectively laser melted Al–Si10–Mg using x-ray computed tomography". In: *Materials Characterization* 111 (2016), pp. 193–204.

[42] G. Kasperovich et al. "Correlation between porosity and processing parameters in TiAl6V4 produced by selective laser melting". In: *Materials and Design* 105 (2016), pp. 160–170. ISSN: 0264-1275. DOI: https://doi.org/10.1016/j.matdes.2016.05.070.

[43] W. W. Wits et al. "Porosity testing methods for the quality assessment of selective laser melted parts". In: *CIRP Annals* 65.1 (2016), pp. 201–204. ISSN: 0007-8506. DOI: https://doi.org/10.1016/j.cirp.2016.04.054.

[44] A. A. Martin et al. "Dynamics of pore formation during laser powder bed fusion additive manufacturing". In: *Nature Communications* 10.1 (2019), p. 1987. ISSN: 2041-1723. DOI: 10.1038/s41467-019-10009-2.

[45] C. L. A. Leung et al. "The effect of powder oxidation on defect formation in laser additive manufacturing". In: *Acta Materialia* 166 (2019), pp. 294–305. ISSN: 1359-6454. DOI: https://doi.org/10.1016/j.actamat.2018.12.027.

[46] T. Vilaro, C. Colin and J. D. Bartout. "As-Fabricated and Heat-Treated Microstructures of the Ti-6Al-4V Alloy Processed by Selective Laser Melting". In: *Metallurgical and Materials Transactions A* 42.10 (2011), pp. 3190–3199. ISSN: 1543-1940. DOI: 10.1007/s11661-011-0731-y.

[47] T. Voisin et al. "Defects-dictated tensile properties of selective laser melted Ti-6Al-4V". In: *Materials and Design* 158 (2018), pp. 113–126. ISSN: 0264-1275. DOI: https://doi.org/10.1016/j.matdes.2018.08.004.

[48] S. Tammas-Williams et al. "The Effectiveness of Hot Isostatic Pressing for Closing Porosity in Titanium Parts Manufactured by Selective Electron Beam Melting". In: *Metallurgical and Materials Transactions A* 47.5 (2016), pp. 1939–1946. DOI: 10.1007/s11661-016-3429-3.

[49] S. Tammas-Williams et al. "The Influence of Porosity on Fatigue Crack Initiation in Additively Manufactured Titanium Components". In: *Sci Rep* 7.1 (2017), p. 7308. DOI: 10.1038/s41598-017-06504-5.

[50] H. Atkinson and S. Davies. "Fundamental aspects of hot isostatic pressing: An overview". In: *Metallurgical and Materials Transactions A* 31: 2981 (2000).

[51] D. Agius et al. "Cyclic plasticity and microstructure of as-built SLM Ti-6Al-4V: The effect of build orientation". In: *Materials Science and Engineering: A* 701.Supplement C (2017), pp. 85–100. ISSN: 0921-5093. DOI: https://doi.org/10.1016/j.msea.2017.06.069.

[52] P. Delroisse et al. "Effect of strut orientation on the microstructure heterogeneities in AlSi10Mg lattices processed by selective laser melting". In: *Scripta Materialia* 141 (2017), pp. 32–35. ISSN: 1359-6462. DOI: https://doi.org/10.1016/j.scriptamat.2017.07.020.

[53] R. Wauthle et al. "Effects of build orientation and heat treatment on the microstructure and mechanical properties of selective laser melted Ti6Al4V lattice structures". In: *Additive Manufacturing* 5 (2015), pp. 77–84.

[54] Z. Chen et al. "Surface roughness of Selective Laser Melted Ti-6Al-4V alloy components". In: *Additive Manufacturing* 21 (2018), pp. 91–103. ISSN: 22148604. DOI: 10.1016/j.addma.2018.02.009.

[55] C.-Y. Fang, C. K. Sung and K.-W. Lui. "Measurement Uncertainty Analysis of CMM with ISO GUM". In: *ASPE Proceedings, Norfolk, VA* (2005).

[56] L. Pagani et al. "Towards a new definition of areal surface texture parameters on freeform surface: re-entrant features and functional parameters". In: *Measurement* (2019). ISSN: 0263-2241. DOI: https://doi.org/10.1016/j.measurement.2019.04.027.

[57] H. Villarraga-Gómez, C. Lee and S. T. Smith. "Dimensional metrology with X-ray CT: A comparison with CMM measurements on internal features and compliant structures". In: *Precision Engineering* 51 (2018), pp. 291–307. ISSN: 0141-6359. DOI: https://doi.org/10.1016/j.precisioneng.2017.08.021.

[58] B. Gapinski et al. "Comparison of Different Method of Measurement Geometry Using CMM, Optical Scanner and Computed Tomography 3D". In: *Procedia Engineering* 69 (2014), pp. 255–262. ISSN: 1877-7058. DOI: https://doi.org/10.1016/j.proeng.2014.02.230.

[59] M. Ferrucci et al. "Towards geometrical calibration of x-ray computed tomography systems—a review". In: *Measurement Science and Technology* 26.9 (Aug. 2015). DOI: 10.1088/0957-0233/26/9/092003.

[60] K. Kiekens et al. "Uncertainty determination for dimensional measurements with computed tomography". In: *Proc. of NDT Conference*. 2012, pp. 183–190.

[61] S. Carmignato, M. Balcon and F. Zanini. "Investigation on the accuracy of CT measurements for wear testing of prosthetic joint components". In: *Proceedings of the Conference on Industrial Computed Tomography (ICT)*. 2014.

[62] A. d. Plessis et al. "Standard method for microCT-based additive manufacturing quality control 3: Surface roughness". In: *MethodsX* 5 (2018), pp. 1111–1116. DOI: 10.1016/j.mex.2018.09.004.

[63] A. Townsend et al. "Factors affecting the accuracy of areal surface texture data extraction from X-ray CT". In: *CIRP Annals* 66.1 (2017), pp. 547–550. ISSN: 0007-8506. DOI: https://doi.org/10.1016/j.cirp.2017.04.074.

[64] P. Shah, R. Racasan and P. Bills. "Comparison of different additive manufacturing methods using computed tomography". In: *Case Studies in Nondestructive Testing and Evaluation* 6 (2016). Special Issue: Industrial computed tomography, pp. 69–78. DOI: https://doi.org/10.1016/j.csndt.2016.05.008.

[65] T. Grimm, G. Wiora and G. Witt. "Characterization of typical surface effects in additive manufacturing with confocal microscopy". In: *Surface Topography: Metrology and Properties* 3.1 (Jan. 2015). DOI: 10.1088/2051-672x/3/1/014001.

[66] L. Farahbod et al. "Assessment of SLM-Manufactured Single Struts as Major Elements of Complex Lattice Structures". In: 2018.

[67] I. Koutiri et al. "Influence of SLM process parameters on the surface finish, porosity rate and fatigue behavior of as-built Inconel 625 parts". In: *Journal of Materials Processing Technology* 255 (2018), pp. 536–546. ISSN: 0924-0136. DOI: https://doi.org/10.1016/j.jmatprotec.2017.12.043.

[68] S. Kleszczynski et al. "Position Dependency of Surface Roughness in Parts from Laser Beam Melting Systems". In: 2015.

[69] M. Suard et al. "Towards stiffness prediction of cellular structures made by electron beam melting (EBM)". In: *Powder Metallurgy* 57.3 (2014), pp. 190–195. DOI: 10.1179/1743290114Y.0000000093.

[70] A. Pérez-Sánchez et al. "Fatigue behaviour and equivalent diameter of single Ti-6Al-4V struts fabricated by Electron Bean Melting orientated to porous lattice structures". In: *Materials and Design* 155 (2018), pp. 106–115. ISSN: 0264-1275. DOI: https://doi.org/10.1016/j.matdes.2018.05.066.

[71] V. Weißmann et al. "Comparison of Single Ti6Al4V Struts Made Using Selective Laser Melting and Electron Beam Melting Subject to Part Orientation". In: *Metals* 7.3 (2017), p. 91. ISSN: 2075-4701. URL: https://www.mdpi.com/2075-4701/7/3/91.

[72] F. Brenne and T. Niendorf. "Load distribution and damage evolution in bending and stretch dominated Ti-6Al-4V cellular structures processed by selective laser melting". In: *International Journal of Fatigue* 121 (2019), pp. 219–228. ISSN: 0142-1123. DOI: https://doi.org/10.1016/j.ijfatigue.2018.12.017.

[73] C. Yan et al. "Evaluations of cellular lattice structures manufactured using selective laser melting". In: *International Journal of Machine Tools and Manufacture* 62 (2012), pp. 32–38. DOI: https://doi.org/10.1016/j.ijmachtools.2012.06.002.

[74] M. Leary et al. "Inconel 625 lattice structures manufactured by selective laser melting (SLM): Mechanical properties, deformation and failure modes". In: *Materials and Design* 157 (2018), pp. 179 –199. DOI: https://doi.org/10.1016/j.matdes.2018.06.010.

[75] B. Lozanovski et al. "Computational modelling of strut defects in SLM manufactured lattice structures". In: *Materials and Design* 171 (2019), p. 107671. DOI: https://doi.org/10.1016/j.matdes.2019.107671.

[76] F. Rosa, S. Manzoni and R. Casati. "Damping behavior of 316L lattice structures produced by Selective Laser Melting". In: *Materials and Design* 160 (2018), pp. 1010 –1018. DOI: https://doi.org/10.1016/j.matdes.2018.10.035.

[77] A. Hussein et al. "Advanced lattice support structures for metal additive manufacturing". In: *Journal of Materials Processing Technology* 213.7 (2013), pp. 1019–1026. DOI: https://doi.org/10.1016/j.jmatprotec.2013.01.020.

[78] J. P. Kruth et al. "Assessing and comparing influencing factors of residual stresses in selective laser melting using a novel analysis method". In: *Proceedings of the Institution of Mechanical Engineers, Part B: Journal of Engineering Manufacture* 226.6 (2012), pp. 980–991. DOI: 10.1177/0954405412437085.

[79] P. J. Bouchard et al. "Measurement of the residual stresses in a stainless steel pipe girth weld containing long and short repairs". In: *International Journal of Pressure Vessels and Piping* 82.4 (2005), pp. 299–310. DOI: http://dx.doi.org/10.1016/j.ijpvp.2004.08.008.

[80] G. Albertini et al. "Comparative neutron and X-ray residual stress measurements on Al-2219 welded plate". In: *Materials Science and Engineering: A* 224.1 (1997), pp. 157–165. DOI: http://dx.doi.org/10.1016/S0921-5093(96)10546-3.

[81] G. Bruno and B. D. Dunn. "Surface and Bulk Residual Stress in Ti6Al4V Welded Aerospace Tanks". In: *Journal of Pressure Vessel Technology* 126.3 (2004), pp. 284–292. DOI: https://doi.org/10.1115/1.1763932.

[82] T. Kannengiesser and A. Kromm. "Formation of welding residual stresses in low transformation temperature (LTT) materials". In: *Soldagem and Inspecao* 14.1 (2009), pp. 74–81. DOI: http://dx.doi.org/10.1590/S0104-92242009000100009.

[83] T. Nitschke-Pagel and H. Wohlfahrt. "Residual Stress Distributions After Welding as a Consequence of the Combined Effect of Physical, Metallurgical and Mechanical Sources". In: *Mechanical Effects of Welding: IUTAM Symposium, Luleå/Sweden, June 10–14, 1991*. Ed. by L. Karlsson, L.-E. Lindgren and M. Jonsson. Berlin, Heidelberg: Springer Berlin Heidelberg, 1992, pp. 123–134. ISBN: 978-3-642-84731-8. DOI: 10.1007/978-3-642-84731-8_11.

[84] N. Nadammal et al. "Effect of hatch length on the development of microstructure, texture and residual stresses in selective laser melted superalloy 718". In: *Materials and Design* (2017).

[85] P. Mercelis and J. Kruth. "Residual stresses in selective laser sintering and selective laser melting". In: *Rapid Prototyping Journal* 12.5 (2006), pp. 254–265. ISSN: 1355-2546. DOI: 10.1108/13552540610707013.

[86] A. E. Patterson, S. L. Messimer and P. A. Farrington. "Overhanging Features and the SLM/DMLS Residual Stresses Problem: Review and Future Research Need". In: *Technologies* 5.2 (2017), p. 15. ISSN: 2227-7080. DOI: https://doi.org/10.3390/technologies5020015.

[87] I. Yadroitsev and I. Yadroitsava. "Evaluation of residual stress in stainless steel 316L and Ti6Al4V samples produced by selective laser melting". In: *Virtual and Physical Prototyping* 10.2 (2015), pp. 67–76. DOI: https://doi.org/10.1080/17452759.2015.1026045.

[88] T. Mukherjee, W. Zhang and T. DebRoy. "An improved prediction of residual stresses and distortion in additive manufacturing". In: *Computational Materials Science* 126 (2017), pp. 360–372. ISSN: 0927-0256. DOI: http://dx.doi.org/10.1016/j.commatsci.2016.10.003.

[89] J. P. Kruth et al. "Selective laser melting of iron-based powder". In: *Journal of Materials Processing Technology* 149.1 (2004), pp. 616–622. DOI: http://dx.doi.org/10.1016/j.jmatprotec.2003.11.051.

[90] J.-P. Kruth et al. "Part and material properties in selective laser melting of metals". In: *Proceedings of the 16th international symposium on electromachining*. 2010, pp. 1–12.

[91] S. D. Bagg, L. M. Sochalski-Kolbus and J. R. Bunn. "The Effect of Laser Scan Strategy on Distortion and Residual Stresses of Arches Made With Selective Laser Melting". In: (Raleigh, NC, United States). American Society of Precision Engineering (ASPE) 2016 Summer Topical Meeting: Dimensional Accuracy and Surface Finish in Additive Manufacturing. NASA Marshall Space Flight Center, June 2016. URL: https://ntrs.nasa.gov/search.jsp?R=20160008858.

[92] S. D. Bagg, L. M. Sochalski-Kolbus and B. J. R. "The Effect of Laser Scan Strategy on Distortion and Residual Stresses of Arches Made With Selective Laser Melting". In: *American Society of Precision Engineering (ASPE) 2016 Summer Topical Meeting* (2017).

[93] M. Schmidt et al. "Laser based additive manufacturing in industry and academia". In: *CIRP Annals* 66.2 (2017), pp. 561 –583. ISSN: 0007-8506. DOI: https://doi.org/10.1016/j.cirp.2017.05.011.

[94] H. Ali, H. Ghadbeigi and K. Mumtaz. "Effect of scanning strategies on residual stress and mechanical properties of Selective Laser Melted Ti6Al4V". In: *Materials Science and Engineering: A* 712 (2018), pp. 175–187. ISSN: 09215093. DOI: 10.1016/j.msea.2017.11.103.

[95] M. F. Zaeh and G. Branner. "Investigations on residual stresses and deformations in selective laser melting". In: *Production Engineering* 4.1 (2009), pp. 35–45. DOI: https://doi.org/10.1007/s11740-009-0192-y.

[96] Y. Lu et al. "Study on the microstructure, mechanical property and residual stress of SLM Inconel-718 alloy manufactured by differing island scanning strategy". In: *Optics and Laser Technology* 75 (2015), pp. 197–206. DOI: http://dx.doi.org/10.1016/j.optlastec.2015.07.009.

[97] T. Mishurova et al. "An Assessment of Subsurface Residual Stress Analysis in SLM Ti-6Al-4V". In: *Materials* 10.4 (2017), p. 348. ISSN: 1996-1944. DOI: https://doi.org/10.3390/ma10040348.

[98] L. Parry, I. A. Ashcroft and R. D. Wildman. "Understanding the effect of laser scan strategy on residual stress in selective laser melting through thermo-mechanical simulation". In: *Additive Manufacturing* 12 (2016), pp. 1–15. ISSN: 22148604. DOI: 10.1016/j.addma.2016.05.014.

[99] T. Thiede et al. "Residual Stress in Selective Laser Melted Inconel 718: Influence of the Removal from Base Plate and Deposition Hatch Length". In: *Materials Performance and Characterization* 7.4 (201), pp. 717–735. DOI: https://doi.org/10.1520/MPC20170119.

[100] J. Song et al. "Role of scanning strategy on residual stress distribution in Ti-6Al4V alloy prepared by selective laser melting". In: *Optik* 170 (2018), pp. 342–352. DOI: 10.1016/j.ijleo.2018.05.128.

[101] T. Mishurova et al. "New aspects about the search for the most relevant parameters optimizing SLM materials". In: *Additive Manufacturing* 25 (2019), pp. 325–334. ISSN: 2214-8604. DOI: https://doi.org/10.1016/j.addma.2018.11.023.

[102] T. Mishurova et al. "The Influence of the Support Structure on Residual Stress and Distortion in SLM Inconel 718 Parts". In: *Metallurgical and Materials Transactions A* 49.7 (2018), pp. 3038–3046. ISSN: 1073-5623 1543-1940. DOI: 10.1007/s11661-018-4653-9.

[103] C. Pappalettere, S. L. Campanelli and C. Casavola. "Preliminary investigation on distribution of residual stress generated by the selective laser melting process". In: *The Journal of Strain Analysis for Engineering Design* 44.1 (2009), pp. 93–104. DOI: https://doi.org/10.1243/03093247JSA464.

[104] M. T. Hutchings et al. *Introduction to the characterization of residual stress by neutron diffraction*. CRC press, 2005. ISBN: 9780203402818.

[105] B. Vrancken et al. "Residual stress via the contour method in compact tension specimens produced via selective laser melting". In: *Scripta Materialia* 87 (2014), pp. 29–32. ISSN: 13596462. DOI: https://doi.org/10.1016/j.scriptamat.2014.05.016.

[106] B. Ahmad et al. "Residual stress evaluation in selective-laser-melting additively manufactured titanium (Ti-6Al-4V) and inconel 718 using the contour method and numerical simulation". In: *Additive Manufacturing* 22 (2018), pp. 571–582. ISSN: 22148604. DOI: 10.1016/j.addma.2018.06.002.

[107] R. J. Moat et al. "Residual stresses in laser direct metal deposited Waspaloy". In: *Materials Science and Engineering: A* 528.6 (2011), pp. 2288–2298. DOI: https://doi.org/10.1016/j.msea.2010.12.010.

[108] B. Vrancken et al. "Study of the influence of material properties on residual stress in selective laser melting". In: *Solid Freeform Fabrication Symposium, Austin, TX, USA* (2013), pp. 393–408.

[109] A. Evans et al. "Relaxation of residual stress in shot peened Udimet 720Li under high temperature isothermal fatigue". In: *International Journal of Fatigue* 27.10 (2005), pp. 1530–1534. DOI: http://dx.doi.org/10.1016/j.ijfatigue.2005.07.027.

[110] M. Boin and R. Wimpory. "Residual Stress Neutron Diffractometer at BER II". In: *Journal of large-scale research facilities* 2.A100 (2016). DOI: http://dx.doi.org/10.17815/jlsrf-2-126.

[111] C. Genzel et al. "The materials science synchrotron beamline EDDI for energy-dispersive diffraction analysis". In: *Nuclear Instruments and Methods in Physics Research Section A: Accelerators, Spectrometers, Detectors and Associated Equipment* 578.1 (2007), pp. 23 –33. DOI: https://doi.org/10.1016/j.nima.2007.05.209.

[112] Z. Wang et al. "Diffraction and single-crystal elastic constants of Inconel 625 at room and elevated temperatures determined by neutron diffraction". In: *Materials Science and Engineering: A* 674 (2016), pp. 406–412. DOI: https://doi.org/10.1016/j.msea.2016.08.010.

[113] Z. Wang et al. "Residual stress mapping in Inconel 625 fabricated through additive manufacturing: Method for neutron diffraction measurements to validate thermomechanical model predictions". In: *Materials and Design* 113 (2017), pp. 169–177. ISSN: 02641275. DOI: https://doi.org/10.1016/j.matdes.2016.10.003.

[114] Z. Wang et al. "Stress relaxation in a nickel-base superalloy at elevated temperatures with in situ neutron diffraction characterization: Application to additive manufacturing". In: *Materials Science and Engineering: A* 714 (2018), pp. 75–83. ISSN: 0921-5093. DOI: https://doi.org/10.1016/j.msea.2017.12.058.

[115] L. Parry, I. A. Ashcroft and R. D. Wildman. "Understanding the effect of laser scan strategy on residual stress in selective laser melting through thermo-mechanical simulation". In: *Additive Manufacturing* 12 (2016), pp. 1–15. ISSN: 22148604. DOI: https://doi.org/10.1016/j.addma.2016.05.014.

[116] G. Vastola et al. "Controlling of residual stress in additive manufacturing of Ti6Al4V by finite element modeling". In: *Additive Manufacturing* 12 (2016), pp. 231–239. DOI: https://doi.org/10.1016/j.addma.2016.05.010.

[117] L. Papadakis et al. "Numerical Computation of Component Shape Distortion Manufactured by Selective Laser Melting". In: *Procedia CIRP* 18 (2014), pp. 90–95. ISSN: 22128271. DOI: 10.1016/j.procir.2014.06.113.

[118] M. Strantza et al. "Coupled experimental and computational study of residual stresses in additively manufactured Ti-6Al-4V components". In: *Materials Letters* 231 (2018), pp. 221–224. DOI: https://doi.org/10.1016/j.matlet.2018.07.141.

[119] K. An et al. "Neutron residual stress measurement and numerical modeling in a curved thin-walled structure by laser powder bed fusion additive manufacturing". In: *Materials and Design* 135 (2017), pp. 122–132. ISSN: 02641275. DOI: 10.1016/j.matdes.2017.09.018.

[120] H. E. Coules et al. "Three-dimensional mapping of the residual stress field in a locally rolled aluminium alloy specimen". In: *Journal of Manufacturing*

Processes 26 (2017), pp. 240–251. ISSN: 1526-6125. DOI: https://doi.org/10.1016/j.jmapro.2017.02.010.

[121] L. M. Sochalski-Kolbus et al. "Comparison of Residual Stresses in Inconel 718 Simple Parts Made by Electron Beam Melting and Direct Laser Metal Sintering". In: *Metallurgical and Materials Transactions A* 46.3 (2015), pp. 1419–1432. DOI: https://doi.org/10.1007/s11661-014-2722-2.

[122] P. A. Colegrove et al. "High Pressure Interpass Rolling of Wire + Arc Additively Manufactured Titanium Components". In: *Advanced Materials Research* 996 (2014), pp. 694–700. DOI: https://doi.org/10.4028/www.scientific.net/AMR.996.694.

[123] T. Watkins et al. "Neutron Characterization for Additive Manufacturing". In: *Advanced Materials and Processes* 171 (2013), p. 23.

[124] E. Cakmak et al. "Mechanical Characterization of an Additively Manufactured Inconel 718 Theta-Shaped Specimen". In: *Metallurgical and Materials Transactions A* 47.2 (2016), pp. 971–980. ISSN: 1543-1940. DOI: 10.1007/s11661-015-3186-8.

[125] J. S. Robinson, D. J. Hughes and C. E. Truman. "Confirmation of Principal Residual Stress Directions in Rectilinear Components by Neutron Diffraction". In: *Strain* 47.s2 (2011), pp. 36–42. ISSN: 0039-2103. DOI: 10.1111/j.1475-1305.2010.00732.x.

[126] F. Bayerlein et al. "Transient development of residual stresses in laser beam melting – A neutron diffraction study". In: *Additive Manufacturing* 24 (2018), pp. 587–594. ISSN: 2214-8604. DOI: https://doi.org/10.1016/j.addma.2018.10.024.

[127] B. Vrancken et al. *Study of the influence of material properties on residual stress in selective laser melting*. 2013, pp. 393–407.

[128] *Inconel Alloy 625*. Aug. 2013.

[129] B. Henke, E. Gullikson and J. Davis. "X-ray interactions: photoabsorption, scattering, transmission, and reflection at E=50-30000 eV, Z=1-92". In: *Atomic Data and Nuclear Data Tables* 54.2 (1993), pp. 181–342. URL: http://henke.lbl.gov/optical_constants/.

[130] K. Moussaoui et al. "Effects of Selective Laser Melting additive manufacturing parameters of Inconel 718 on porosity, microstructure and mechanical properties". In: *Materials Science and Engineering: A* 735 (2018), pp. 182–190. DOI: https://doi.org/10.1016/j.msea.2018.08.037.

[131] J. H. Tan, W. L. E. Wong and K. W. Dalgarno. "An overview of powder granulometry on feedstock and part performance in the selective laser melting process". In: *Additive Manufacturing* 18 (2017), pp. 228–255. ISSN: 22148604. DOI: 10.1016/j.addma.2017.10.011.

[132] S. Carmignato, W. Dewulf and R. Leach. *Industrial X-Ray Computed Tomography*. Springer International Publishing, 2017. ISBN: 9783319595733. URL: https://books.google.co.uk/books?id=KLo6DwAAQBAJ.

[133] A. Kak and M. Slaney. *Principles of Computerized Tomographic Imaging*. IEEE Press, 1988. ISBN: 9780879421984. URL: https://books.google.co.uk/books?id=RKhrAAAAMAAJ.

[134] J. Radon. "On the determination of functions from their integral values along certain manifolds". In: *IEEE Transactions on Medical Imaging* 5.4 (1986), pp. 170–176. DOI: 10.1109/TMI.1986.4307775.

[135] L. A. Feldkamp, L. C. Davis and J. W. Kress. "Practical cone-beam algorithm". In: *Journal of the Optical Society of America A* 1.6 (1984), pp. 612–619. DOI: 10.1364/JOSAA.1.000612.

[136] E. Ametova, M. Ferrucci and W. Dewulf. "A tool for reducing cone-beam artifacts in computed tomography data". In: (Leuven, Belgium). Feb. 2017. URL: https://www.ndt.net/events/iCT2017/app/content/Extended_Abstract/91_Ametova_Rev1.pdf.

[137] R. Roche et al. "Quantification of porosity in Acropora pulchra (Brook 1891) using X-ray micro-computed tomography techniques". In: *Journal of Experimental Marine Biology and Ecology* 396 (Dec. 2010). DOI: 10.1016/j.jembe.2010.10.006.

[138] K. Schörner, M. Goldammer and J. Stephan. "Scatter Correction by Modulation of Primary Radiation in Industrial X-ray CT : Beam-hardening Effects and their Correction". In: International Symposium on Digital Industrial Radiology and Computed Tomography. 2011. URL: https://www.semanticscholar.org/paper/Scatter-Correction-by-Modulation-

of-Primary-in-CT-%3A-Sch%C3%B6rner-Goldammer/3156033c70a0a-671183c7e101e215ec3d476ff15.

[139] Z. Wei, S. Wiebe and D. Chapman. "Ring artifacts removal from synchrotron CT image slices". In: *Journal of Instrumentation* 8 (June 2013). DOI: 10.1088/1748-0221/8/06/C06006.

[140] B. Münch et al. "Stripe and ring artifact removal with combined wavelet — Fourier filtering". In: *Optics Express* 17.10 (2009), pp. 8567–8591. DOI: 10.1364/OE.17.008567.

[141] V. Hauk. *Structural and Residual Stress Analysis by Nondestructive Methods: Evaluation - Application - Assessment*. Elsevier Science, 1997. ISBN: 9780080541952. URL: https://books.google.de/books?id=mwecnh6cuDEC.

[142] I. Noyan and J. Cohen. *Residual Stress: Measurement by Diffraction and Interpretation*. Materials Research and Engineering. Springer New York, 2013. ISBN: 9781461395706. URL: https://books.google.de/books?id=EaVtCQAAQBAJ.

[143] M. Hutchings and A. Krawitz. *Measurement of Residual and Applied Stress Using Neutron Diffraction*. Nato Science Series E: Springer Netherlands, 2012. ISBN: 9789401127974. URL: https://books.google.de/books?id=s5_qCAAAQBAJ.

[144] L. Spieß et al. *Moderne Röntgenbeugung: Röntgendiffraktometrie für Materialwissenschaftler, Physiker und Chemiker*. Vieweg+Teubner Verlag, 2015. ISBN: 9783663108313. URL: https://books.google.de/books?id=6HGQBwAAQBAJ.

[145] V Hauk and H.-J Nikolin. "The Evaluation of the Distribution of Residual Stresses of the I. Kind (RS I) and of the II. Kind (RS II) in Textured Materials". In: *Textures and Microstructures* 8 (Jan. 1988). DOI: 10.1155/TSM.8-9.693.

[146] *Research Reactors*. Access: 20.06.2019. Dec. 2018. URL: http://www.world-nuclear.org/information-library/non-power-nuclear-applications/radioisotopes-research/research-reactors.aspx.

[147] A. Cooke and J. Slotwinski. "Properties of Metal Powders for Additive Manufacturing: A Review of the State of the Art of Metal Powder Property Testing". In: (2012). DOI: 10.6028/nist.Ir.7873.

[148] T. Thiede et al. "3D Shape Analysis of Powder for Laser Beam Melting by Synchrotron X-ray CT". In: *Quantum Beam Sci.* 3.3 (2019). DOI: https://doi.org/10.3390/qubs3010003.

[149] R. Cunningham et al. "Synchrotron-Based X-ray Microtomography Characterization of the Effect of Processing Variables on Porosity Formation in Laser Power-Bed Additive Manufacturing of Ti-6Al-4V". In: *Jom* 69.3 (2017), pp. 479–484. DOI: 10.1007/s11837-016-2234-1.

[150] A. Rack et al. "High resolution synchrotron-based radiography and tomography using hard X-rays at the BAMline (BESSY II)". In: *Nuclear Instruments and Methods in Physics Research Section A: Accelerators, Spectrometers, Detectors and Associated Equipment* 586.2 (2008), pp. 327–344. ISSN: 0168-9002. DOI: 10.1016/j.nima.2007.11.020.

[151] V. Voland et al. *Novel Techniques for High-Resolution Computed Tomography of Optoelectronic Devices*. 2012.

[152] D. Paganin et al. "Simultaneous phase and amplitude extraction from a single defocused image of a homogeneous object". In: *Journal of Microscopy-Oxford* 206 (2002), pp. 33–40. ISSN: 0022-2720. DOI: 10.1046/j.1365-2818.2002.01010.x.

[153] J. Schindelin et al. "The ImageJ ecosystem: An open platform for biomedical image analysis". In: *Molecular Reproduction and Development* 82.7-8 (2015), pp. 518–529. ISSN: 1098-2795. DOI: 10.1002/mrd.22489.

[154] C. Tomasi and R. Manduchi. "Bilateral filtering for gray and color images". In: *Sixth International Conference on Computer Vision (IEEE Cat. No.98CH36271)*. 1998, pp. 839–846. DOI: 10.1109/ICCV.1998.710815.

[155] T. Ridler and S. Calvard. "Picture Thresholding Using an Iterative Selection Method". In: *IEEE Transactions on Systems, Man, and Cybernetics* 8.8 (1978), pp. 630–632. ISSN: 0018-9472. DOI: 10.1109/TSMC.1978.4310039.

[156] B. Münch et al. "FIB-Nanotomography of Particulate Systems—Part II: Particle Recognition and Effect of Boundary Truncation". In: *Journal of the American Ceramic Society* 89.8 (2006), pp. 2586–2595. ISSN: 0002-7820. DOI: 10.1111/j.1551-2916.2006.01121.x.

[157] R. K. McGeary. "Mechanical Packing of Spherical Particles". In: *Journal of The American Ceramic Society* 44.10 (1961), pp. 513–522.

[158] H. A.C. K. Hettiarachchi and W. K. Mampearachchi. "Effect of vibration frequency, size ratio and large particle volume fraction on packing density of binary spherical mixtures". In: *Powder Technology* 336 (2018), pp. 150–160. ISSN: 0032-5910. DOI: https://doi.org/10.1016/j.powtec.2018.05.049.

[159] A. du Plessis et al. "Standard method for microCT-based additive manufacturing quality control 4: Metal powder analysis". In: *MethodsX* 5 (2018), pp. 1336 –1345. DOI: https://doi.org/10.1016/j.mex.2018.10.021.

[160] I. Jolliffe. *Principal Component Analysis*. International Encyclopedia of Statistical Science. Berlin, Heidelberg: Springer Berlin Heidelberg, 2011. ISBN: 978-3-642-04898-2. DOI: 10.1007/978-3-642-04898-2_455.

[161] W. Feller. *An introduction to probability theory and its applications*. Wiley series in probability and mathematical statistics: Probability and mathematical statistics. Wiley, 1971. ISBN: 9780471257097.

[162] *Powders for powder metallurgical purposes - Sampling*. Standard. Nov. 2007.

[163] J. E. Ayer and F. E. Soppet. "Vibratory Compaction: I, Compaction of Spherical Shapes". In: *Journal of the American Ceramic Society* 48.4 (1965), pp. 180–183. ISSN: 0002-7820. DOI: 10.1111/j.1151-2916.1965.tb14708.x.

[164] S. Pednekar, J. Chun and J. F. Morris. "Bidisperse and polydisperse suspension rheology at large solid fraction". In: *Journal of Rheology* 62.2 (2018). DOI: https://doi.org/10.1122/1.5011353.

[165] *VG studio MAX 3.2 Reference Manual*. Aug. 2018.

[166] A. d. Plessis et al. "X-Ray Microcomputed Tomography in Additive Manufacturing: A Review of the Current Technology and Applications". In: *3D Printing and Additive Manufacturing* 5.3 (2018), pp. 227–247. DOI: 10.1089/3dp.2018.0060.

[167] *Geometrical product specifications (GPS) — Surface texture: Areal — Part 6: Classification of methods for measuring surface texture*. Standard. 17.040.20. Feb. 2010.

[168] M. Bornemann et al. “Design and Validation of an Additively Manufactured Flow Cell–Static Mixer Combination for Inline NMR Spectroscopy”. In: *Industrial & Engineering Chemistry Research* 58.42 (2019), pp. 19562–19570. DOI: 10.1021/acs.iecr.9b03746.

[169] B. K. Bay et al. “Digital volume correlation: Three-dimensional strain mapping using X-ray tomography”. In: *Experimental Mechanics* 39.3 (1999), pp. 217–226. DOI: 10.1007/BF02323555.

[170] L. Farahbod-Sternahl et al. “Mechanisches Verhalten L-PBF-gefertigter Gitterstrukturen”. In: 2019, pp. 389–402. ISBN: 978-3-446-46223-6. DOI: 10.3139/9783446462441.027.

[171] I. Maskery et al. “An investigation into reinforced and functionally graded lattice structures”. In: *Journal of Cellular Plastics* 53.2 (2017), pp. 151–165. DOI: 10.1177/0021955X16639035.

[172] J. M. Warnett et al. “Towards in-process x-ray CT for dimensional metrology”. In: *Measurement Science and Technology* 27.3 (2016), p. 035401. DOI: 10.1088/0957-0233/27/3/035401.

[173] M. Hofmann et al. “The New Materials Science Diffractometer STRESS-SPEC at FRM-II”. In: *Residual Stresses VII, ECRS7*. Vol. 524. Materials Science Forum. Trans Tech Publications Ltd, Sept. 2006, pp. 211–216. DOI: 10.4028/www.scientific.net/MSF.524-525.211.

[174] T. M. Holden, A. P. Clarke and R. A. Holt. “Neutron diffraction measurements of intergranular strains in MONEL-400”. In: *Metallurgical and Materials Transactions a-Physical Metallurgy and Materials Science* 28.12 (1997), pp. 2565–2576. DOI: https://doi.org/10.1007/s11661-997-0014-9.

[175] T. Holden et al. “Determination and mitigation of the uncertainty of neutron diffraction measurements of residual strain in large-grained polycrystalline material”. In: *Journal of Applied Crystallography* 48 (2015). DOI: 10.1107/S1600576715002757.

[176] W. Yangfan, C. Xizhang and S. Chuanchu. “Microstructure and mechanical properties of Inconel 625 fabricated by wire-arc additive manufacturing”. In: *Surface and Coatings Technology* 374 (2019), pp. 116 –123. DOI: https://doi.org/10.1016/j.surfcoat.2019.05.079.

[177] Y. Gao and M. Zhou. "Superior Mechanical Behavior and Fretting Wear Resistance of 3D-Printed Inconel 625 Superalloy". In: *Applied Sciences* 8 (Dec. 2018), p. 2439. DOI: 10.3390/app8122439.

[178] M. M. Attallah et al. "Additive manufacturing of Ni-based superalloys: The outstanding issues". In: *MRS Bulletin* 41.10 (2016), pp. 758–764. DOI: 10.1557/mrs.2016.211.

[179] B. A. Szost et al. "A comparative study of additive manufacturing techniques: Residual stress and microstructural analysis of CLAD and WAAM printed Ti–6Al–4V components". In: *Materials and Design* 89 (2016), pp. 559–567. ISSN: 0264-1275. DOI: http://dx.doi.org/10.1016/j.matdes.2015.09.115.

[180] E. O. Olakanmi. "Effect of mixing time on the bed density, and microstructure of selective laser sintered (sls) aluminium powders". In: *Materials Research* 15.2 (2012), pp. 167–176. ISSN: 1980-5373 1516-1439. DOI: 10.1590/s1516-14392012005000031.

[181] *Geometrical product specification (GPS). Surface texture. Profile method. Terms, definitions and surface texture parameters*. Standard. 17.040.20. Apr. 1997.